Design of multi-heterojunction organic photovoltaic devices

by

Edward George New

A thesis submitted for the degree of

Doctor of Philosophy

at The University of Warwick

Department of Chemistry

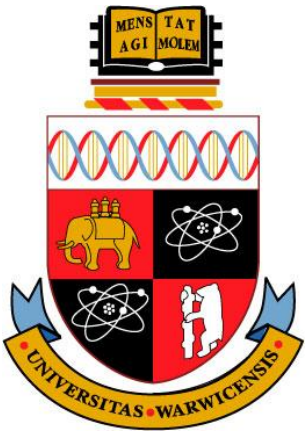

May 2013

Abstract

Organic photovoltaic (OPV) devices have shown great potential as an inexpensive source of renewable energy. There are many factors that affect the efficiency of an OPV device, and understanding them can help the design of new architectures to boost the efficiency towards a commercially viable level. Multijunction OPV devices have been realised as a key route to higher efficiencies. The work presented in this thesis focuses on the design of multi heterojunction OPV devices based upon small molecule organic semiconductors.

A small molecule tandem OPV device consisting of two donor materials with complementary absorption spectra, boron subphthalocyanine chloride (SubPc) and aluminium phthalocyanine chloride (ClAlPc) combined with C_{60} as the acceptor is used as a test device architecture.
The recombination layer between the sub-cells was investigated first, with the layer thickness and deposition conditions optimised. Modification of the photoactive layers by co-deposition of the donor and acceptor, and the use of a templating layer is proven to increase the device efficiency.

α-NPD co-deposited with MoO_x was used as a hole transport and optical spacer layer in single junction and tandem OPV devices. The electrical, optical and morphological properties of the α-NPD and the co-deposited layers are investigated. The hole transporting properties of α-NPD:MoO_x are shown in a SubPc / C_{60} device with the optical spacing properties shown for a ClAlPc:C_{60} bulk heterojunction (BHJ) device. Implementation of the α-NPD:MoO_x optical spacer layer is shown as a tool for current matching in a SubPc:C_{60} BHJ tandem OPV device. An optical simulation predicts the use of an optical spacer will improve the device performance as it positions the sub-cells in an optimum optical field position for current matching. Experimental results show good agreement with the optical simulation and an improvement in short circuit current (J_{SC}) is shown with the α-NPD:MoO_x optical spacer layer. The tandem OPV device is also shown with a larger active area which displays good operational stability characteristics.

A multi-heterojunction cascade device was designed using α-sexithiophene (α-6T) as an interfacial layer with phthalocyanine / C_{60} OPV devices. The α-6T is shown to dissociate excitons in the phthalocyanine layer and contribute to the photocurrent of the device without affecting the phthalocyanine / C_{60} interface. The dual exciton dissociation in the cascade device leads to an increased J_{SC} compared to the bilayer devices.

Table of Contents

Declaration

I declare that the work presented in this thesis was conducted by myself at the Department of Chemistry at the University of Warwick. The transfer matrix simulations were carried out using a program written by Thomas Howells and ellipsometry measurements were carried out by L.O.T-Oriel GmbH & Co. KG. I confirm that none of this work has been previously published for a higher degree.

Acknowledgments

Firstly, I would like to thank my supervisor Professor Tim Jones for giving me the opportunity to carry out my work in the fascinating area of organic photovoltaic devices, and for his guidance and support throughout this time. I would also like to thank the members of the Department of Chemistry for assistance throughout my PhD as well as the University of Warwick Postgraduate Research Scholarship for their funding.

I would like to acknowledge all of the members of the Tim Jones group that have helped make these past years enjoyable, so my thanks goes to Paul, Stefan, Ian, Nicola, Luke, Tom, Raff, Chloe, Nat, Gavin, V, Jay, Mark and Tomasz. I would especially like to thank Dr Paul Sullivan for his help and advice with learning the experimental techniques and for his proofreading. Thanks also go to all of the members of the group who made C110 a great office to work in.

My time at Warwick wouldn't have been as enjoyable without the social aspect of the people in the department. Many relaxing evenings were spent after a hard day's work in the university pub "The Grad", for those old enough to remember and still call it by its old name. My thanks go to all of the group, especially my old housemate Nicola and to Dave and Mike, who were always on hand for a drink.

Finally, I would like to thank my family for putting up with my stress over the course of my PhD. I am indebted to my parents, Rosemary and Michael, who have given me so much love and support throughout my life and I could not achieve any of this without them. I would also like to thank my brothers and family; Robert, Philip, Nic, Chloe, Chloe, Calum and Phoebe for their love and support.

List of publications

- T. Howells, E. New, P. Sullivan, T.S. Jones, *An External Quantum Efficiency Technique to Directly Observe Current Balancing in Tandem Organic Photovoltaics*, Advanced Energy Materials, 2011, 1(6), 1085-1088
- E. New, T. Howells, P. Sullivan, T.S. Jones, *Small molecule tandem organic photovoltaic cells incorporating an α-NPD optical spacer layer*, Organic Electronics, 2013, 14(9), 2353-2359
- E. New, N. Beaumont, P. Sullivan, T.S. Jones, *Increased photocurrent in small molecule organic solar cells through a dual heterojunction cascade structure* , to be submitted.

List of abbreviations

General abbreviations

α-6T	α-sexithiophene
AFM	Atomic Force Microscopy
Ag	Silver
Al	Aluminium
AM	Air Mass
α-NPD	N,N'-diphenyl-N,N'-bis(1-naphthyl)-1,1'-biphenyl-4,4'-diamine
AO	Atomic Orbital
Au	Gold
BCP	Bathocuproine
BHJ	Bulk Heterojunction
ClAlPc	Aluminium Phthalocyanine Chloride
CuPc	Copper Phthalocyanine
CT	Charge Transfer State
D / A	Donor / Acceptor
DSSC	Dye Sensitised Solar Cell
EQE	External Quantum Efficiency
GaAs	Gallium Arsenide
HOMO	Highest Occupied Molecular Orbital
ICBA	Indene-C_{60} bisadduct
InP	Indium Phosphide
ITO	Indium Tin Oxide
LUMO	Lowest Unoccupied Molecular Orbital
MDMO-PPV	poly[2-methoxy-5-(3',7',-dimethyloctyloxy)-1,4-phenylenevinylene]

MeO-TPD	N,N,N,N-Tetrakis(4-methoxyphenyl)-benzidine
MO	Molecular Orbital
MoO_x	Molybdenum Oxide
OFET	Organic Field Effect Transistor
OMBD	Organic Molecular Beam Deposition
OPV	Organic Photovoltaic
P3HT	poly(3-hexylthiophene-2,5,diyl)
PCBM	[6,6]-phenyl-C61butyric acid methyl ester
PCPDTBT	poly[2,6-(4,4-bis-(2-ethylhexyl)-4H-cyclopenta[2,1-b;3,4-b']dithiophene)-alt-4,7-(2,1,3-benzothiadiazole)]
PEDOT	poly(3,4-ethylenedioxythiophene)
PL	Photoluminescence
PHJ	Planar Heterojunction
PTBEHT	poly-1-di(2-ethylhexyloxy)phenyl)-thieno[3,4-b]pyrazine
PTCBI	3,4,9,10-perylenetetracarboxylic bis-benzimidazole
PTCDA	Perylene-3,4,9,10-tetracarboxylic dianhydride
PV	Photovoltaic
QCM	Quartz Crystal Microbalance
SAM	Self Assembled Monolayer
SubPc	Boron Subphthalocyanine Chloride
TAE	Total Absorption Efficiency
TT	tetraceno-[2,3-b]-thiophene
ZnPc	Zinc Phthalocyanine

Physical quantities and parameters

α	Absorption Coefficient
A	Absorption
Abs	Absorptance
A_g	Electron Affinity
D	Exciton Diffusion Coefficient
ε	Dielectric Constant
E_B	Exciton Binding Energy
E_F	Fermi Level
E_G	Interface Band Gap
$\eta_{(A,ED,CT,CC)}$	Quantum Efficiency of (Absorption, Exciton Diffusion, Exciton Dissociation and Charge Collection)
FF	Fill Factor
I	Light Intensity
I_0	Incident Light Intensity
I_g	Ionisation Potential
IQE	Internal Quantum Efficiency
J_{MP}	Current Density at Maximum Power Point
J_{ph}	Photocurrent
J_{SC}	Short Circuit Current Density
J-V	Current Density - Voltage
k_B	Boltzman constant
L_D	Exciton Diffusion Length
r_B	Bohr Radius
r_C	Coulomb radius

R_q	Surface Roughness Parameter
R_S	Series Resistance
R_{SH}	Shunt Resistance
T	Temperature
T	Transmittance
τ	Exciton Lifetime
VL	Vacuum Level
V_{MP}	Voltage at Maximum Power Point
V_{OC}	Open Circuit Voltage

Chapter 1 Introduction

1.1 Why the need for solar energy

There has been a rise in global energy consumption over the years as the population of the world and industrialisation in developing countries increases. To keep up with the energy demand, the burning of fossil fuels such as coal, oil and natural gas has mainly been used as shown in Figure 1.1.

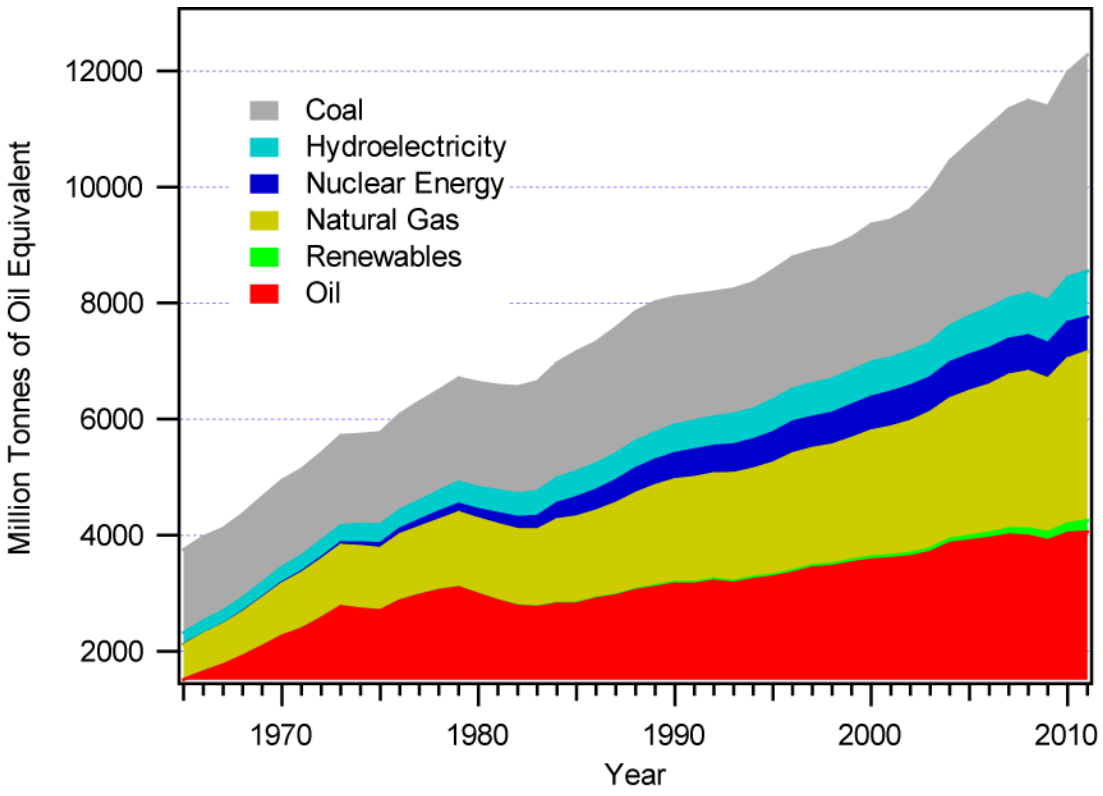

Figure 1.1: World energy consumption in million tonnes of oil equivalent per year. Data taken from BP statistical review of World Energy June 2012. [1]

These energy reserves are of limited supply and production of these fuels is due to decline so there is a need for an alternative energy supply to make up the increasing demand. The burning of fossil fuels also releases greenhouse gases and air pollutants which are damaging for the environment and human health. The greenhouse gas CO_2 is one of the main contributors to global warming, which has already led to a 0.6^{o}C rise in global surface temperature.[2] In Europe there is a goal to reduce CO_2 emissions by 20% by 2020, based upon 2008 levels. All of these factors have led to an increase in using renewable energy sources, although the current high cost still drives the use of more economically viable fossil fuels.

Most of the renewable energy sources are directly or indirectly fuelled by the sun; the most abundant energy provider to the Earth. Current calculations estimate that it supplies 10,000 times more energy to the Earth's surface than the total world energy consumption. Covering just 0.1% of the Earth's surface with 10 % efficient photovoltaic (PV) devices would provide enough energy to meet demand, showing the great potential for the technology.

1.2 History of photovoltaic devices

The development of modern PV devices started in Bell Labs after the discovery by Russell Ohl of the p-n junction in crystalline silicon.[3] Early devices were expensive to produce but had a commercial application for satellites, starting with the Vanguard I satellite in 1958. Modern monocrystalline silicon PV devices have reached efficiencies of ~25 %,[4] but are still expensive due to the high processing temperatures and manufacturing conditions that are required to make large area defect-free crystals. Amorphous silicon can be used to reduce the fabrication cost but

this leads to a reduction in efficiency to ~10 %, and these devices are commercially used only for small scale electronic applications.

A second generation of PV devices were developed using combinations of group III and V elements such as gallium arsenide (GaAs) and indium phosphide (InP) which have band gaps closer to the optimum value from the Shockley Queisser limit. The use of multijunction devices can overcome the Shockley Queisser limit by utilising junctions that absorb photons in different energy ranges, for example, $Ga_{(0.51)}In_{(0.49)}P$ (1.83 eV) / $In_{(0.04)}Ga_{(0.96)}As$ (1.34 eV) / $In_{(0.37)}Ga_{(0.63)}As$ (0.89 eV) [5] High efficiencies of over 40% have been achieved using concentrated light in a III-V multijunction device.[4] The high cost of producing these devices has limited the commercialisation of the technology.

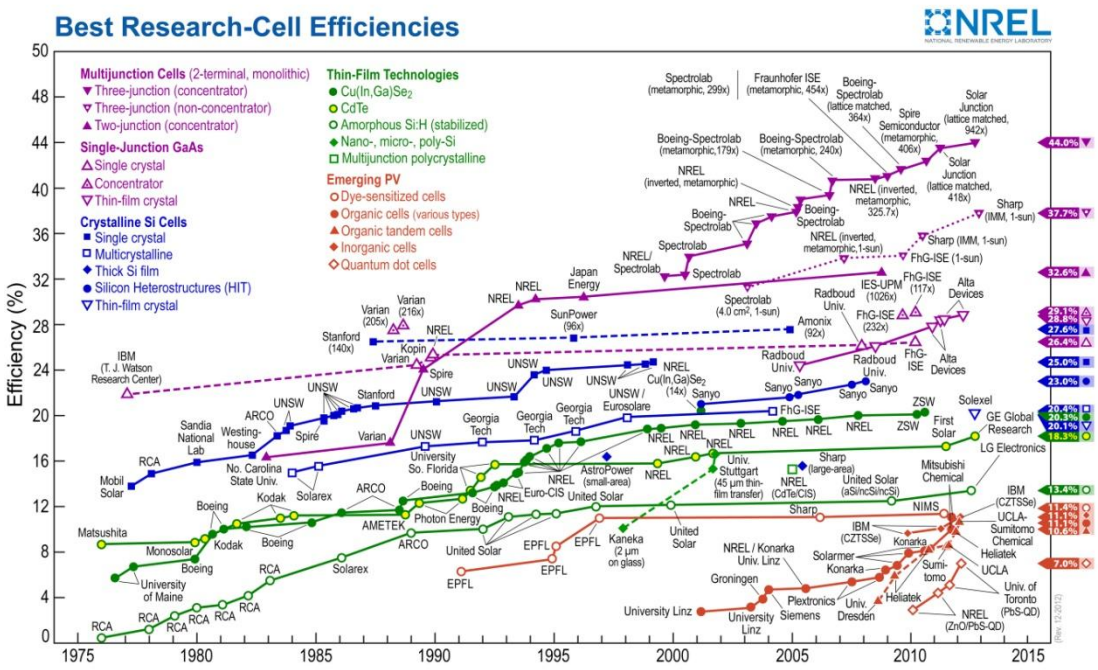

Figure 1.2: Certified research cell efficiencies for different PV technologies over the period 1975 – 2012.[6]

The latest generation of PV devices are based upon organic semiconductor active materials which have high absorption coefficients allowing for thin layers to be used for light harvesting. The high abundance of carbon, oxygen, nitrogen and hydrogen and the low process temperatures of organic molecules allow for low cost material and fabrication. Although the efficiency of the cells is lower than the inorganic counterparts, the added benefits of non-toxic materials, low cost and low weight make it a promising technology. The best research efficiencies of all PV devices are shown in Figure 1.2.

Organic photovoltaic (OPV) devices can be separated into three main classes: dye sensitized solar cells (DSSC), polymer OPVs and small molecule OPVs. DSSCs were invented by O'Regan and Graetzel in 1991[7] and have achieved efficiencies up to 12.3 %.[8] This device concept is based upon an electrochemical redox PV where a photon absorbing and electron donating dye are coated on an electron accepting titanium dioxide layer. An electrolyte acts as a redox for the dye and charge is transferred to the electrodes. The development of other OPV devices is described in section 1.3.

1.3 Development of OPV devices

Early development of OPVs was based upon using single organic semiconductor layers such as phthalocyanines sandwiched between two electrodes of different work functions.[9] These had low efficiency as exciton separation occurred only at defect sites or in the thin depletion region close to the electrode and opposite charges were transported in the same material leading to increased recombination. A major advance in OPV device structure was made by Tang in 1986 with the creation of the donor / acceptor (D / A) heterojunction device.[10] By using two organic semiconductors with electron donor and electron acceptor properties, an energy level offset is produced at the material interface for efficient exciton dissociation. This also had the added benefit of separating the transport of electrons and holes in different materials which reduced recombination. Using copper phthalocyanine (CuPc) as the electron donor and 3,4,9,10-perylenetetracarboxylic bis-benzimidazole (PTCBI) as the electron acceptor gave an efficiency of 0.95 %. Further improvement was achieved using C_{60} as the electron acceptor. C_{60} possesses a high exciton diffusion length of ~40 nm and a high acceptor strength due to its degenerate lowest unoccupied molecular orbital and employing it in a CuPc OPV device increased efficiency to 3.6 %.[11]

Intermixing the donor and acceptor materials to form a bulk heterojunction (BHJ) been presented as a method to improve exciton dissociation. This has been shown by Sullivan et al., where the co-deposition of CuPc and C_{60} enabled an increase in short circuit current density (J_{SC}) compared to the planar heterojunction.[12] Excitons that are generated in the BHJ layer are always within a diffusion length of the D / A interface which increases exciton dissociation. Co-deposition of planar

phthalocyanines (e.g. CuPc) and C_{60} tends to form an amorphous film which can reduce the hole and electron mobility of the BHJ layer by one order of magnitude compared to the planar layers.[13] By elevating the temperature of the substrate during co-deposition the morphology of the BHJ can be controlled to improve the charge transport and percolation pathways to the electrodes, improving the device efficiency. Pfuetzner et al. demonstrated this concept for a zinc phthalocyanine (ZnPc) : C_{60} BHJ device.[14] Deposition at 110 °C showed an improved efficiency of 2.56 % compared to the 1.59 % achieved at room temperature. Using this method, efficiencies of up to 6.9 % have been achieved for dicyanovinyl-capped oligothophene derivatives codeposited with C_{60}.[15]

Development of new electron donors based upon squarines, merocyanines, oligothiophenes and donor-acceptor oligomers which improve light absorption in the near infrared have pushed single heterojunction vacuum evaporated OPV device efficiencies towards 7 %.[16,17]

1.4 Tandem OPV devices

A tandem OPV device is a multi-heterojunction architecture where two or more D / A heterojunctions are stacked on top of each other and connected, usually in series. The realisation of a tandem device structure allows for the improvement of two issues inherent to organic semiconductors. The first issue is the short exciton diffusion length that limits the distance over which the excitons can diffuse to an interface and therefore limits the thickness of the organic layer. The resulting thickness is below 100 nm and leads to far too little light absorption for efficient photon harvesting. Using a tandem structure can increase the total active layer

thickness and hence light absorption without hindering dissociation. The second issue is that, unlike inorganic semiconductors, the absorption profile of organic semiconductors is not a continuum but is narrow in nature and made up of discrete peaks. Using organic semiconductors with different band gaps can overcome the narrow absorption spectra utilising more of the solar spectrum.

Small molecule vacuum evaporated tandem solar cells were the first to be developed due to their ease of fabrication. The first tandem organic solar cell was created by Hiramoto in 1990[18] using a metal-free phthalocyanine donor combined with a perylene tetracarboxylic derivative acceptor. An ultra-thin discontinuous Au layer provided an ohmic contact between the two sub-cells to recombine the electrons and holes from opposing sub-cells, preventing charge build up. The tandem device achieved an open circuit voltage (V_{OC}) of 0.78 V nearly twice that of the sub-cell, as expected from Kirchoff's law with heterojunctions in a series connection. This idea was developed further by Yakimov et al. who stacked up to five CuPc / PTCBI heterojunctions in a series connection.[19] The two-heterojunction OPV device achieved an efficiency of 2.5 %, more than double that of the single heterojunction device efficiency of 1.1 %.

Efficiencies were improved by Maennig et al. for a ZnPc:C_{60} BHJ tandem device.[20] They separated the photoactive regions with p-doped N,N,N,N-Tetrakis(4-methoxyphenyl)-benzidine (MeO-TPD) and n-doped C_{60}. These act as selective transport layers as well as isolating the recombination contact from the excitons. This was further improved by Drechsel et al. by optimising the dopants of the n and p-type transport layers achieving an efficiency of 3.8 %.[21] Xue et al. used thin layers of bathocuproine and PTCBI as exciton blocking layers to improve the

recombination layer in a CuPc / C_{60} tandem OPV device.[22] By tuning the sub-cells for preferential CuPc and C_{60} absorption it achieved an efficiency of 5.7 %.

Using two different donor materials which absorb different parts of the solar spectrum were used to make the most recent advances in efficiency. In 2010, Cheyns et al. achieved a 5.15 % using a complementary green-absorbing boron subphthalocyanine chloride (SubPc) (500 – 600 nm) in combination with boron subnapthphthalocyanine chloride (550 – 750 nm) to cover most of the visible spectrum.[23] Other combinations of phthalocyanines have shown similar promise for small-molecule tandem PV devices [24-26]. The current leader in the field is the work done by the company Heliatek. Their development of a broadly absorbing oligothiophene derivative and new doped transport layers has steadily increased efficiency over recent years to the current record of 12 %.[27] The ease of fabrication in vacuum has allowed for the multijunction concept to be taken to an extreme with up to 10 junctions connected,[28] and a new high voltage concept reported by Sullivan et al.[29] using high voltage sub-cells to create a tandem device with a V_{OC} up to 7 V.

Solution processed polymer solar cells have also branched into the tandem device concept to increase the absorption coverage, but fabrication of multiple sequential solution processed layers causes some engineering problems regarding dissolution of previous layers.[30] The first solution-processed tandem cell was created by Kawano et al. based upon sub-cells of poly[2-methoxy-5-(3',7',-dimethyloctyloxy)-1,4-phenylenevinylene] (MDMO-PPV), with the fullerene derivative [6,6]-phenyl-C61 butyric acid methyl ester (PCBM), and a DC magnetron sputtered ITO recombination layer, achieving an efficiency of 3.1 %.[31] The voltage in the tandem cell was reduced from the ideal addition of the sub-cells by the high work function of the ITO producing a poor ohmic contact. Other early reports combined solution

process sub-cells with vacuum deposited phthalocyanine-based sub-cells to overcome the dissolution problem and create a tandem cell with increased spectral coverage from 400 – 800 nm.[32] Hadipour et al. produced the first tandem cell comprising of two complementary absorbing conjugated-polymers-based sub-cells.[33] A low band gap donor polymer poly-[34-di(2-ethylhexyloxy)phenyl)-thieno[3,4-b]pyrazine (PTBEHT) was used to extend the coverage out to 1000 nm. The first fully solution processed tandem device was produced by Gilot et al. by replacing the usually evaporated metal recombination layer with spin cast ZnO nanoparticles from acetone followed by pH neutral poly(3,4-ethylenedioxythiophene) (PEDOT) from water [35] A breakthrough in efficiency was achieved by Kim et al. who achieved 6.5% using a highly efficient low band gap polymer donor poly[2,6-(4,4-bis-(2-ethylhexyl)-4H-cyclopenta[2,1-b;3,4-b']dithiophene)-alt-4,7-(2,1,3-benzothiadiazole)] (PCPDTBT) sub-cell in combination with a poly(3-hexylthiophene-2,5,diyl) (P3HT) sub-cell.[34] An extension in fullerene absorption was added by employing $PC_{70}BM$ as the acceptor in the P3HT sub-cell and $PC_{60}BM$ in the PCPDTBT sub-cell. Further development has been achieved using a fullerene derivative indene-C_{60} bisadduct (ICBA) to increase the V_{OC} of a P3HT sub-cell and finding new low band gap polymers to extend the absorption spectra into the near IR.[36,37] The current record for polymer tandem OPV devices is 10.6 %.[38]

1.5 Organic semiconductors

Organic compounds are classed as materials that contain carbon atoms and carbon-hydrogen bonds. Due to the flexibility of the carbon backbone, a virtually unlimited number of compounds can be synthesised which can each have unique properties. The semiconducting properties of certain classes of these organic compounds come from the properties of the carbon atom. The electron ground state configuration of a carbon atom is $1s^2 2s^2 2p^2$, with the electrons in the $2s^2 2p^2$ orbitals being the valence electrons. Hybridisation of the 2s and 2p atomic orbitals (AO) leads to different bonding orbital configurations depending upon the mixing of the s orbital with multiple p orbitals, such as sp, sp^2 and sp^3. For organic semiconductors, the most interesting hybridisation is sp^2 where the 2s orbital combines with the $2p_x$ and the $2p_y$ orbitals to form three degenerate sp^2 orbitals. These sp^2 orbitals are coplanar and separated by an angle of 120^o. The remaining $2p_z$ orbital is unchanged and is located perpendicular to the plane. A simple sp^2 hybridised carbon molecule is ethene (C_2H_4), which combines two sp^2 carbon atoms and four hydrogen atoms. The sp^2 orbitals form σ-bonds which are localised between the C-C and C-H atoms, whereas the $2p_z$ orbitals on the two carbon atoms overlap to form a delocalised π- bond. Increasing the carbon chain by adding more sp^2 carbon atoms will cause the π molecular orbital (MO) to be delocalised across the whole molecule. The overlap of all of the AOs of each atom contribute to the overall MO, preserving the number of orbitals. Each MO is filled according to the Pauli principle with two electrons that have opposite spin. In the ground state, the lowest energy orbitals are filled with electrons with the remaining orbitals unoccupied. The occupied orbitals are known as bonding MOs and the unoccupied known as anti-bonding MOs. Figure 1.3 displays a schematic of the energy levels for ethene and an energy gap is shown

between the π-orbital and the π* anti-bonding orbital. These are defined as the highest occupied molecular orbital (HOMO) and the lowest unoccupied molecular orbital (LUMO). Typical π-π* energy gaps for conjugated molecules are in the order of a few electron volts and photons from the ultraviolet to infrared spectral region usually have sufficient energy to excite an electron. This makes organic semiconductors interesting for optoelectronic applications. The energy level gap depends upon the amount of conjugation there is in the system, e.g. anthracene has a band gap of 3.72 eV[39] absorbing UV photons compared to the 1.9 eV band gap of pentacene with two more fused benzene rings which absorbs ~650 nm.[40]

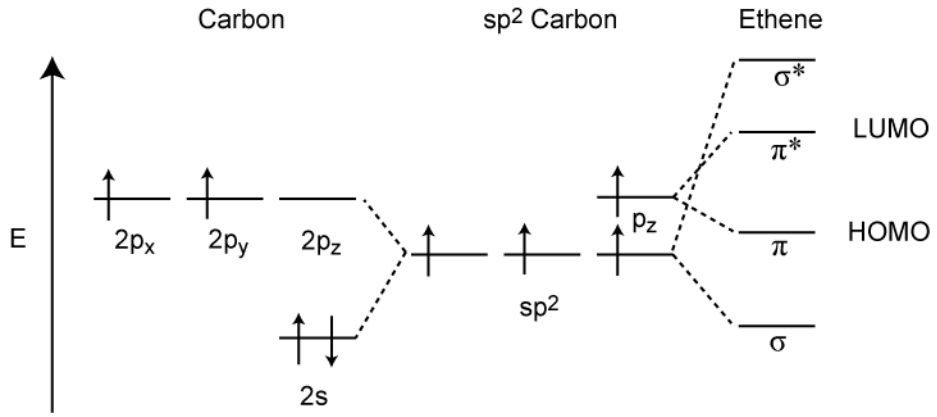

Figure 1.3: Energy level diagram of the valence orbitals of carbon, sp2 hybridised carbon and ethene.

Organic semiconductors in the solid state are only weakly bound by van der Waals interactions and do not form covalent bonds. The binding energies of these interactions are much weaker that a covalent bond, and as a result of this organic compounds tend to have a low melting temperature, low dielectric constants and a small intrinsic conductivity.

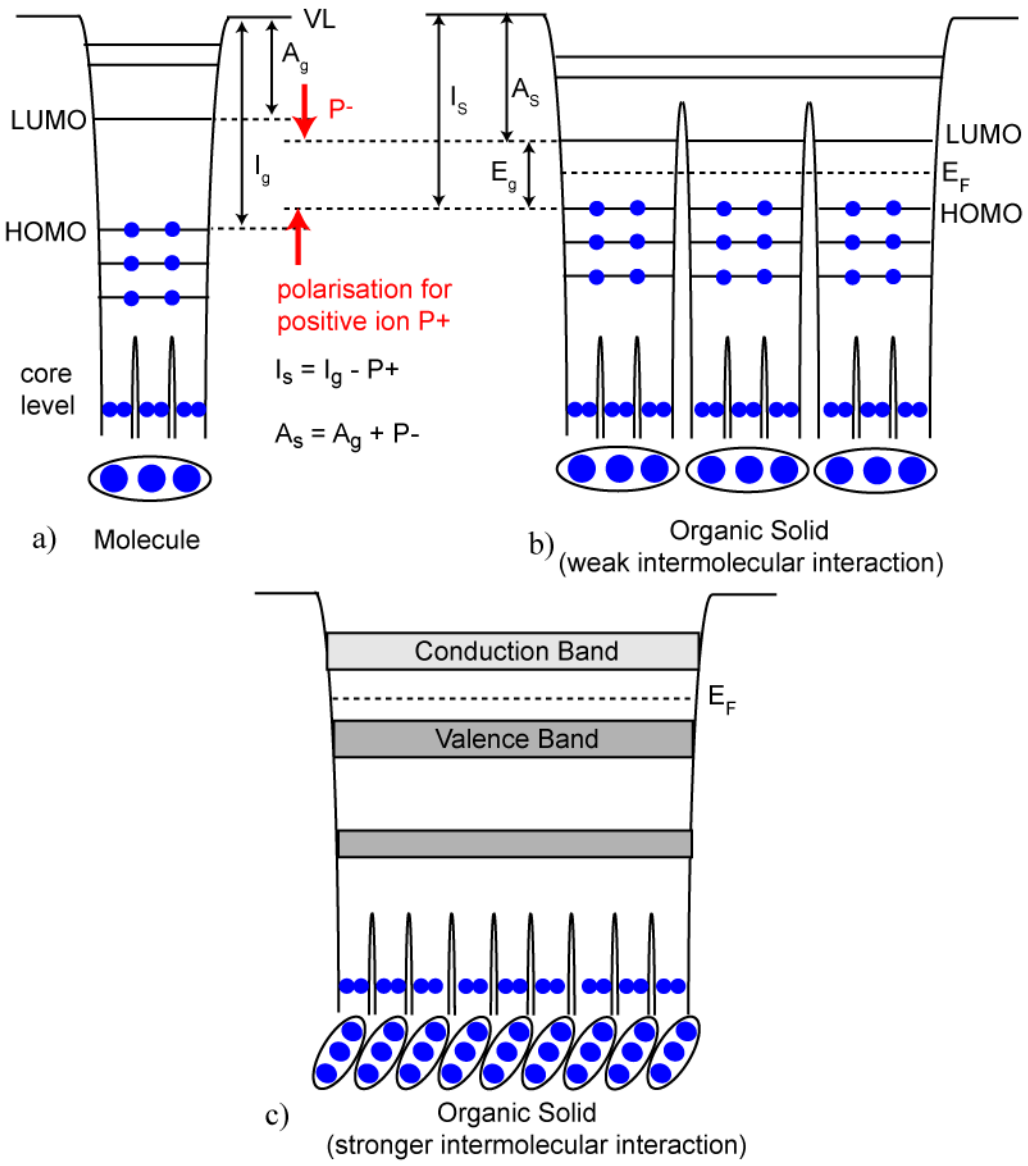

Figure 1.4: Schematic of evolution of the electronic structure from a) single molecule to b) organic solid with weak intermolecular interaction to c) organic solid with stronger intermolecular interaction, adapted from Reference.[41]

The schematic of the electronic structure for a molecule consisting of three atoms is shown in Figure 1.4a. The atomic nuclei form a potential well which isolates the core electrons, and they possess the features of AOs. Further up the potential wells merge to form a broad well which is occupied by various MOs, each having two electrons. The top of the well is the vacuum level (*VL*) and electrons excited above this level

can escape the molecule to the vacuum. The energy separation from the HOMO and the LUMO to the *VL* are defined as the ionisation energy (I_g) and the electron affinity (A_g) of the molecule, respectively. In an organic solid, due to the weak interaction between the molecules, the MOs of the occupied and lower unoccupied states are usually localised on each molecule. This results in a narrow intermolecular energy band width and the electronic structure of an organic solid approximately preserves that of a molecule. In an organic solid with stronger intermolecular interactions the occupied and unoccupied bands become wider because of the increased overlapping of relevant MOs in adjacent molecules and move out of the potential well of the individual molecule.

Moving to an organic solid the I_g and A_g become the I_s and A_s of the solid. When a hole is introduced in the HOMO (likewise for electron in the LUMO) of the solid, electronic polarisation of the surrounding molecules stabilise the ion by screening effects. This leads to a reduction of the ionisation potential and an increase in the electron affinity, lowering the band gap (E_g) of the molecular solid as shown in Figure 1.4.

1.6 Device operation

The principles of operation of an organic photovoltaic device, for the conversion of solar radiation into electrical energy, can be split into four main processes.

1. A photon of light is absorbed and an exciton is created within the photoactive layer (η_{abs})
2. The exciton diffuses to the donor / acceptor interface (η_{ed})
3. The exciton is dissociated into free charges overcoming the exciton and geminate pair binding energy (η_{ct})
4. The free charge carriers are transported through the device and extracted at the electrodes (η_{cc})

A schematic of an OPV device at open circuit showing these processes is shown in Figure 1.5, and further explanation on each of the processes is given in the following sections. The overall external quantum efficiency (*EQE*) is defined as the number of extracted charges per incident photon and can be expressed as the product of the four quantum efficiencies of the operational processes as shown in Equation 1.1.

$$EQE = \eta_{abs}\,\eta_{ed}\eta_{ct}\eta_{cc} \qquad \text{(Equation 1.1)}$$

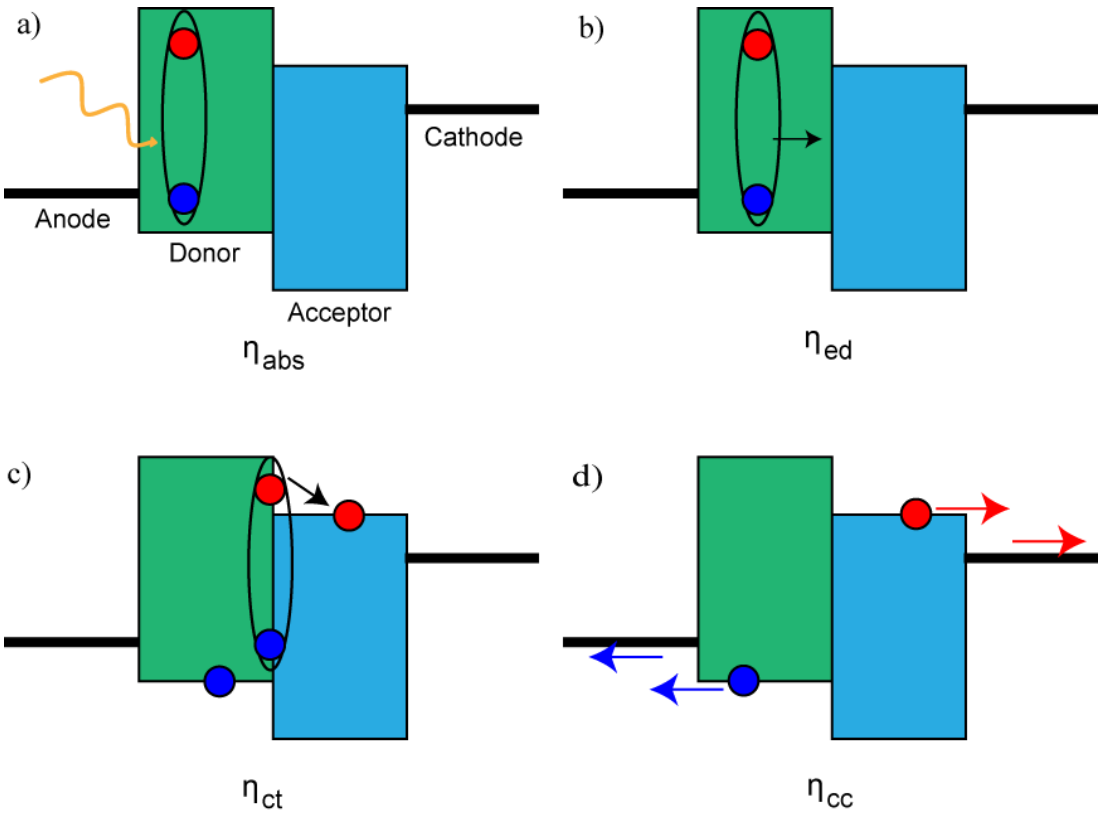

Figure 1.5: A schematic of an OPV device in open circuit conditions showing the principle of operation: a) light absorption and exciton formation, b) exciton diffusion, c) exciton dissociation and d) charge collection. Each process has a quantum efficiency associated with it labelled below.

1.6.1 Light absorption and exciton formation

Organic semiconductors have band gaps which allow for the absorption of light from the visible part of the solar spectrum. The absorption of a photon by an organic semiconductor leads to the promotion of an electron in the HOMO to an excited state in the LUMO leaving behind a vacant positive charge in the HOMO called a 'hole'. Relaxation of the excited state occurs to a more energetically stable bound excited stated due to the Coulombic attraction between the oppositely charged species. This bound electron-hole excited state is known as an 'exciton' which is mobile and electrically neutral.

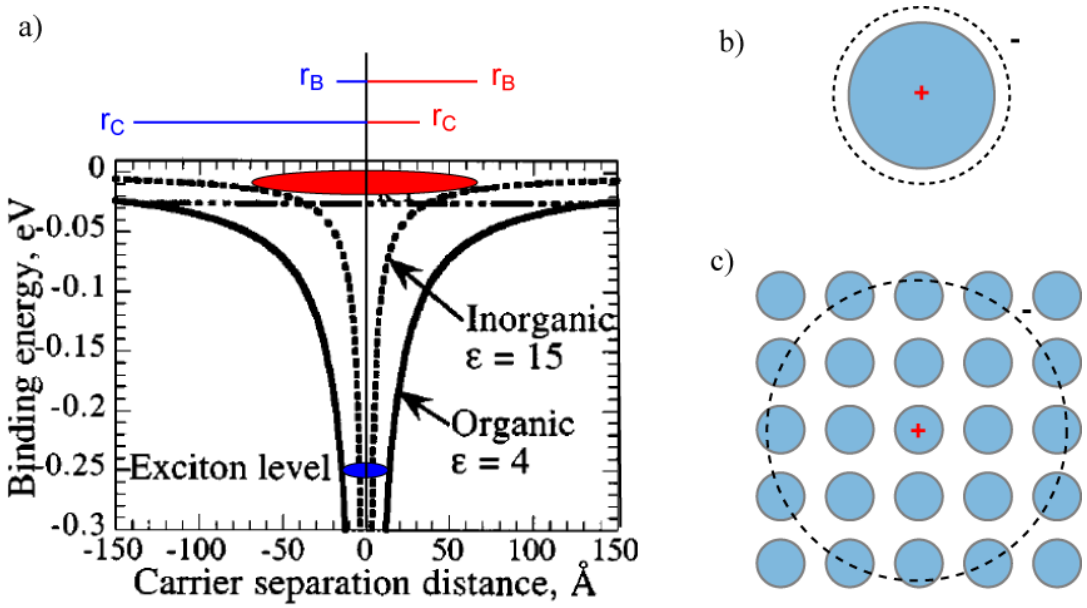

Figure 1.6: a) Binding energy diagram of a typical organic (blue) and inorganic (red) semiconductor showing the comparison between the Bohr radius (r_B) and Coulomb radius (r_C) adapted from Reference [42]. A schematic of the two exciton types b) Frenkel and c) Mott-Wannier exciton.

The strength of the exciton binding energy is highly dependent upon the material properties; most notably the dielectric constant, ε, as shown in Figure 1.6a.[42] In organic semiconductors, ε is low (~3-4) due to the weak electronic interactions between organic molecules resulting in low screening of the electron-hole pair and a large Coulombic interaction. This spatially restricts the electron's wavefunction (approximated by the Bohr radius r_B) as it is localised in the potential well of its conjugate hole.[43] When r_B is less that the lattice spacing in the semiconductor, a tightly bound Frenkel exciton is formed, which is localised on the absorbing molecule (Figure 1.6b). These have typical binding energies of 0.3-0.6 eV[44] and require a loss in potential energy larger than the binding energy to dissociate.

Inorganic semiconductors have a high $\varepsilon > 10$ due to strong interatomic electronic interactions of covalently bound inorganic atoms. This allows for a large r_B

extending across many atoms and leads to generation of free charges upon photon absorption as the r_B extends further than the r_C. Hence, there is sufficient energy at room temperature (k_BT) to overcome the electron-hole Coulombic attraction. This type of exciton is known as a Mott-Wannier exciton (Figure 1.6c).

1.6.2 Exciton diffusion

Excitons are mobile due to the intermolecular interaction between molecules allowing transfer of an excited state from one molecule to another. As excitons are electrically neutral species, they are unaffected by electric fields only move due to diffusion in a random hopping motion. The average distance that an exciton can travel before recombination is quantified by the exciton diffusion length as shown in Equation 1.2.

$$L_D = \sqrt{D\tau} \qquad \text{(Equation 1.2)}$$

The L_D is material specific and is determined by a function of the diffusion coefficient, D, and the exciton lifetime, τ. Typically, L_D for organic semiconductors is in the order of nanometres with some materials having a wide range of quoted values. L_D for C_{60} has been reported as 40 nm[45] and a range between 8 and 28 nm[46,47] has been measured for SubPc. Diffusion in polycrystalline organic semiconductors is limited by grain boundaries and trap sites causing recombination. The L_D becomes an approximation of the optimal thickness of a photoactive layer in an OPV device as efficient exciton diffusion to a D / A heterojunction is required to dissociate the exciton before recombination. This limits the use of thicker layers for increased light absorption and device structures using bulk heterojunctions and multi-junctions have been used to overcome this.

1.6.3 Exciton Dissociation

To separate an exciton into two free charges the exciton binding energy has to be overcome and this is usually achieved by an energy offset at a heterojunction of two organic materials. The material combination is selected such that the energy offset is larger than the exciton binding energy. In the case of an exciton formed in the donor material (Figure 1.7), the ΔLUMO offset must be larger than the exciton binding energy, E_B, for efficient dissociation.[48] The electron is transferred to the LUMO of the acceptor and separated from the hole which remains in the HOMO of the donor. A similar process occurs when the exciton is generated in the acceptor with the driving force being the ΔHOMO offset and the hole being transferred to the HOMO of the donor. The electron and hole at the D / A interface are still Coulombically bound as a geminate pair due to the low dielectric constants of the materials which can make them prone to recombination.[49,50] This attraction is overcome by the electric field created within the device.[48] The maximum obtainable V_{OC} of a D/A heterojunction OPV device has been proposed as the interface gap E_G between the HOMO level of the donor and the LUMO level of the acceptor, corrected for the geminate binding energy.[51,52] Cascade OPV devices have been created which provide multiple heterojunctions for exciton dissociation.[53] This is discussed further in Section 1.8.

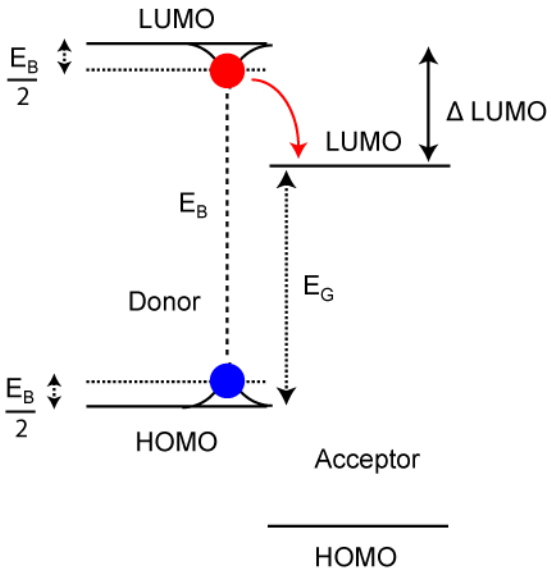

Figure 1.7: Energy level diagram of exciton dissociation at a donor / acceptor interface.

1.6.4 Charge Collection

The free charges after dissociation have to move through the device to be collected at the electrodes to produce an electric current flow in the external circuit. The electrons are transported by the electron acceptor to the cathode and the holes are transported by the electron donor to the anode. The charge collection depends upon the mobility of the material. In inorganic semiconductors with strong covalently bound crystal structures and long range order, the charge mobility is high. In organic semiconductors the intermolecular bonding is weaker and based upon van der Waals and π-π interactions. This leads to a more polycrystalline or even an amorphous structure depending upon the interaction strengths, and charge mobility is orders of magnitude lower as the mobility is dependent upon charge carriers hopping between molecules and domains.[54] The charge carrier mobility of organic semiconductors can vary over several orders of magnitude due to their morphology, from 10^{-6}-10^{-3} cm^2 V^{-1} s^{-1} for amorphous films to > 1 cm^2 V^{-1} s^{-1} for highly crystalline films.[55] The mobility is also affected by the direction of the intermolecular interaction between

molecules with a higher mobility often found in the stacking direction of the molecule.[56]

When the charge reaches the organic / electrode interface it must be extracted into the electrode. For this to occur efficiently, the workfunction of the electrode must align with the appropriate energy level of the organic material (HOMO for anode injection and LUMO for cathode injection). If alignment is poor then injection barriers can be formed by band bending when the Fermi levels of the organic material and the electrode align. As the choice of electrode materials is limited, modification of the electrode workfunction by using self-assembled monolayers (SAMs)[57,58] and metal oxides[59-61] have been used to align the electrode with the organic material.

1.7 Operation of Tandem OPVs

The development of tandem OPV devices as a way to overcome the narrow absorption spectra and thin absorbing layers was outlined in section 1.4. Here we describe the operation of tandem OPV devices, in particular the recombination layer, measuring sub-cells photocurrents and the optical design.

1.7.1 Recombination Layers

The creation of a tandem device of two D/A heterojunctions connected in series requires more than just directly placing the second heterojunction on top of the first to create a D/A/D/A structure. In this circumstance a reverse A/D heterojunction is created between the acceptor of the first cell and the donor of the second. Exciton

dissociation at this interface opposes the two other heterojunctions, reducing the device voltage and performance. Using exciton blocking layers at this interface can eliminate the exciton dissociation, but the resulting free holes and electrons created in the sub-cells need to recombine at this interface to allow for a single current to flow through the device according to Kirchoff's current law. An efficient recombination layer will need make an ohmic contact to the LUMO of the acceptor in the first sub-cell and the HOMO of the donor in the second sub-cell to have high charge extraction and to effectively recombine charges and prevent voltage loss at the interface. In a series connected tandem OPV device, the V_{OC} of the tandem device is the summation of the two V_{OC}s of the single heterojunction sub-cells as shown in Figure 1.8.

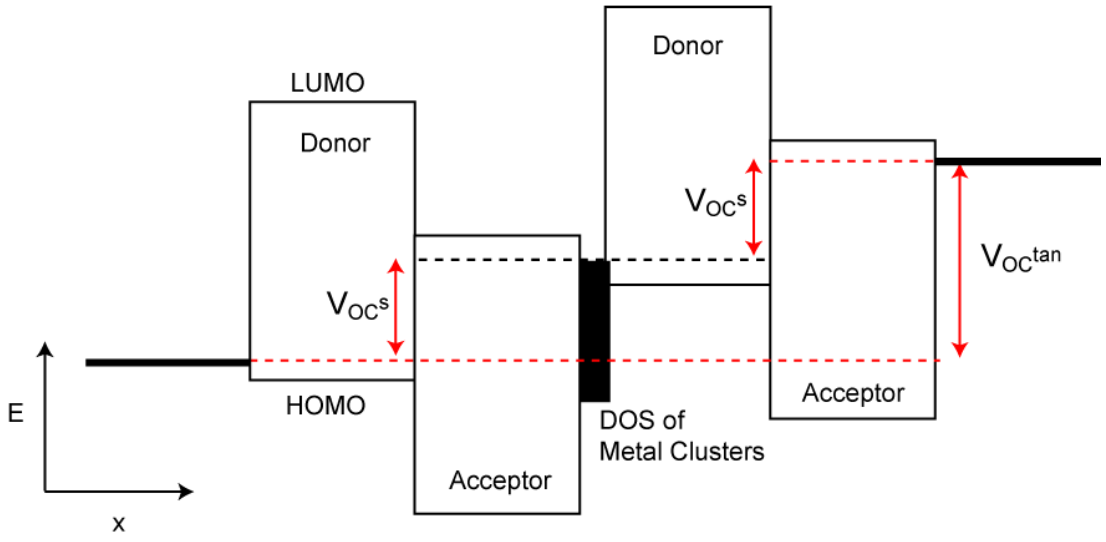

Figure 1.8: Schematic of energy band diagram of a tandem device adapted from Reference [62].

Many types of recombination layer have been used to demonstrate an effective tandem OPV device. The first reported and most widely used recombination contact

in tandem OPV devices are thin metal layers that may be complete or form nanoclusters. A range of metals, including (Au, Ag and Al) have been used and they have a range of energy states in between the HOMO and LUMO of each sub-cell that act as recombination centres for electrons and holes from each sub-cell (Figure 1.8).[63-65] These are usually sandwiched between an exciton blocking layer and a hole transport layer and have provided efficient recombination layers where the V_{OC} has been observed to be close to the summation of the sub-cells. Other recombination contacts in polymer tandem OPV devices have been produced using the high workfunction PEDOT: PSS as a hole transport layer and the low workfunction metal oxides ZnO or TiO_x as an electron transport layer.[34,35] The highly doped PEDOT:PSS acts as a metal and forms an ohmic contact with the photo-doped metal oxides. Recently, PEDOT:PSS modified using ethoxylated polyethylenimine to lower its workfunction from 4.9 eV to 3.6 eV and has been shown to act as a highly transparent, highly conductive recombination layer that has ohmic contacts to both sub-cells.[66] In small molecule vacuum evaporated tandem cells, using thin metal recombination layers has its drawbacks such as migration of the metal nanoclusters and absorption losses from the metal layer. A new recombination design based upon highly doped organic layers was demonstrated by Timmreck et al.[62] The highly doped layers shifts the Fermi level towards HOMO and LUMO levels, resulting in a very small HOMO-LUMO offset and a high recombination rate at the contact. The V_{OC} of the tandem cell achieved no loss in voltage summation and tandem OPV devices based upon this recombination layer have shown high efficiencies of up to 12%.

1.7.2 Sub-cell Photocurrent Matching

The other consideration when fabricating a tandem OPV device is the current matching of the sub-cells. As mentioned previously, the series connection of the sub-cells requires a single current passing through the device. In most cases, each sub-cell will produce a different photocurrent and the J_{SC} of a tandem device is usually higher than the lowest current generated in the two sub-cells. This increase in photocurrent is due to the change in the electric field over the device.[67] An example energy band diagram of a tandem device as short circuit conditions is shown in Figure 1.9a. In this device, sub-cell 1 produces more photocurrent than sub-cell 2 and the electrons extracted from sub-cell 1 are not completely counterbalanced, as fewer holes in sub-cell 2 are reaching the recombination interface. At steady-state, this reduces the electric field across sub-cell 1 and increases the field across sub-cell 2. Therefore, at short-circuit conditions in the tandem device (V = 0), sub-cell 1 is operating in forward bias, whereas sub-cell 2 is operating in a reverse bias of equal magnitude, assisting charge carrier collection in this sub-cell. In tandem OPV devices, this increase can be significant as they display field assisted collection.

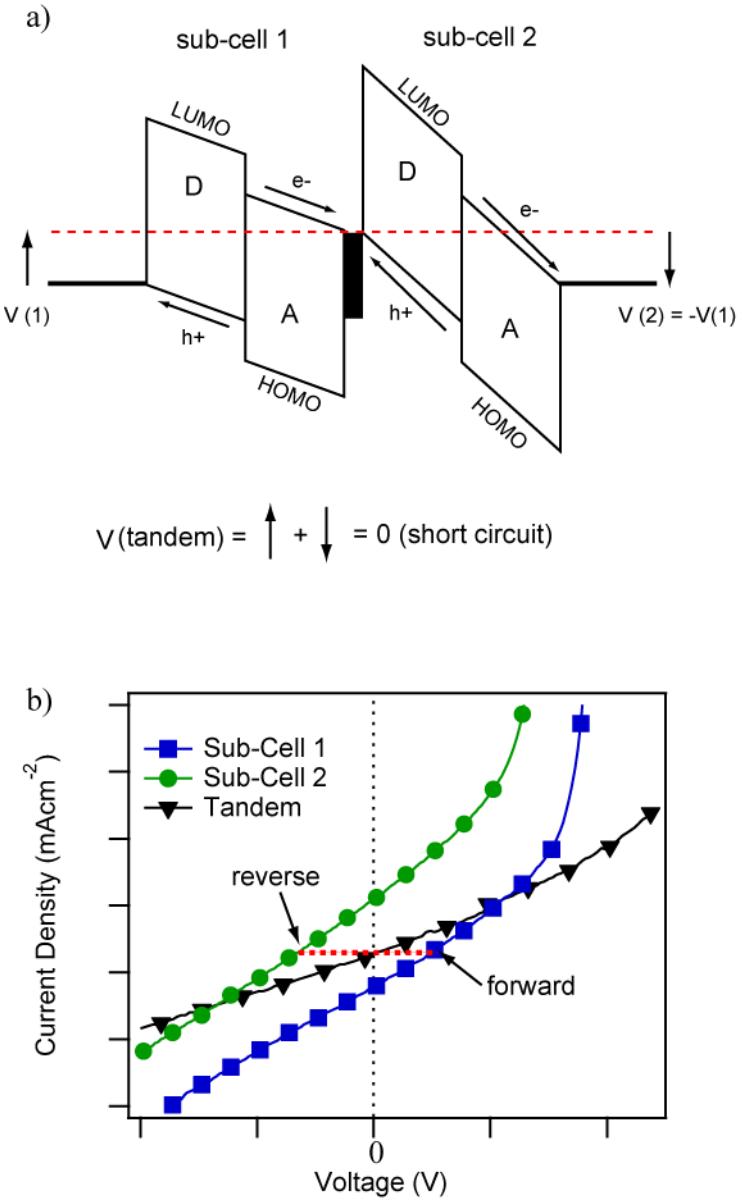

Figure 1.9: a) Energy band diagram of a tandem OPV device with unbalanced sub-cell photocurrents at 0V (short circuit conditions). b) *J-V* characteristics of a tandem OPV device and its sub-cells.

Figure 4.19b shows the current-voltage (*J-V*) characteristics for the tandem OPV device and the sub-cells displayed in the energy band diagram (Figure 4.19a). The J_{SC} of the tandem OPV device occurs at the intersect V = 0 V with the over performing and underperforming sub-cells shown from their respective J_{SC} values. The operation of the sub-cells in the tandem architecture at 0 V is shown by the red dotted line, with a photocurrent at reverse bias for the underperforming sub-cell.

Consequently, the over performing sub-cell operates with a forward bias as seen from the band diagram (Figure 4.19a).

Measuring the *J-V* characteristics of each sub-cell would be beneficial to obtain a deeper understanding on how the sub-cells operate in a tandem OPV device. This can be achieved in parallel connected three terminal devices, where a common anode or cathode acts as the interconnection between the two sub-cells. This requires a recombination layer with a high parallel conductivity which is usually obtained by using a thick metallic layer, e.g. PEDOT:PSS / Au (20 nm).[68] The problem with this configuration for high efficiency devices is the transmission loss from the thick recombination layer.

In a normal two terminal series connected tandem device, the recombination layer has a low conductivity parallel to the surface making it unable to be used for external *J-V* measurements. Methods have been produced to measure the photocurrent of the sub-cells in a tandem OPV configuration by measuring the external quantum efficiency (*EQE*) of the individual sub-cells. This can then be integrated over the AM1.5 solar spectrum to give a J_{SC} for the sub-cell and an insight into the current balancing. Measuring the *EQE* of a tandem OPV device is more challenging than a single heterojunction device as both sub-cells have to absorb light to pass current. The response of the device under monochromatic light will shift the current limiting between the sub-cells as each sub-cell will absorb a different part of the spectrum. To measure the *EQE* of the sub-cell in a tandem OPV device, the sub-cell must be current limiting across the whole spectral range.[32] Gilot et al. has developed a method for measuring the *EQE* of the sub-cells of a tandem OPV device by using bias illumination.[69] The spectrum of the bias illumination is chosen such that the bias light is mostly absorbed in one of the two sub-cells and results in a charge generation

in that sub-cell that exceeds the other sub-cell. The later sub-cell will therefore be current limiting over the entire spectral range and the EQE of the tandem OPV device will represent that of the current limiting sub-cell. As one sub-cell is generating more charges than the other, it will increase the electric field across the current limiting sub-cell and it will be operating at reverse bias (Figure 1.9a), as the *EQE* is measured at V = 0. This will generate an overestimation of the J_{SC} as shown in Figure 1.9b, so a forward electrical bias is applied to the tandem OPV device. The forward electrical bias applied is calculated by using single heterojunction devices and measuring under illumination conditions that represent the sub-cells in the tandem OPV device. The applied bias is the absolute value of voltage of the data points on the *J-V* curves with equal current densities and opposite sign voltages. An alternative method to directly observe current balancing in tandem OPV devices using white light illumination bias has been demonstrated by Howells et al.[24] This technique involved comparing the EQE of tandem OPV devices under white light bias and with no bias, with the least variation between the two measurements resulting from the device with balanced sub-cell photocurrents.

Two improved methods were introduced by Gilot et al. to measure the *J-V* characteristics of the sub-cells in a tandem OPV device.[70] The first method used an extra proximity electrode placed outside the active area but in contact to the recombination layer to act as a voltage probe for the sub-cells. By measuring the *J-V* characteristic of the tandem OPV device and the voltage difference between the proximity electrode and one of the two electrodes, the *J-V* characteristics of the sub-cells can be determined. The second method uses the illumination bias and electrical bias *EQE* as described before, but by applying different electrical biases the *J-V* curve can be constructed for the sub-cells.

1.7.3 Optical Design of Tandem OPV Devices

To design an optimised tandem OPV device with balanced sub-cell photocurrents the optical effects within the layers has to be investigated. In polymer tandem OPV devices the photoactive layers tend to be > 100 nm in thickness and light attenuation through these layers reduces the light intensity in the back sub-cell closest to the Al electrode.[36] The optimal design for this system is to have the wide band gap polymer in the front sub-cell and the low band gap polymer in the back sub-cell. The low energy photons then pass through the front sub-cell without being absorbed and enter the back sub-cell. In the reverse design, photons with a higher energy than the low band gap polymer would be absorbed in the front sub-cell reducing the light in the back sub-cell. To fully optimise the polymer tandem OPV device, optical simulations are used to calculate the photocurrent contribution of each sub-cell with varied photoactive layer thickness, which is then adjusted to balance the photocurrents of the sub-cells.[71] In small molecule vacuum evaporated OPV devices, the photoactive layer thickness is much lower, typically ~50 nm in total and light attenuation is not the dominating factor in absorptance within the layers. The reflecting back electrode causes interference of the incident and reflected light, creating a node in the optical field and a standing wave that propagates through the layer structure.

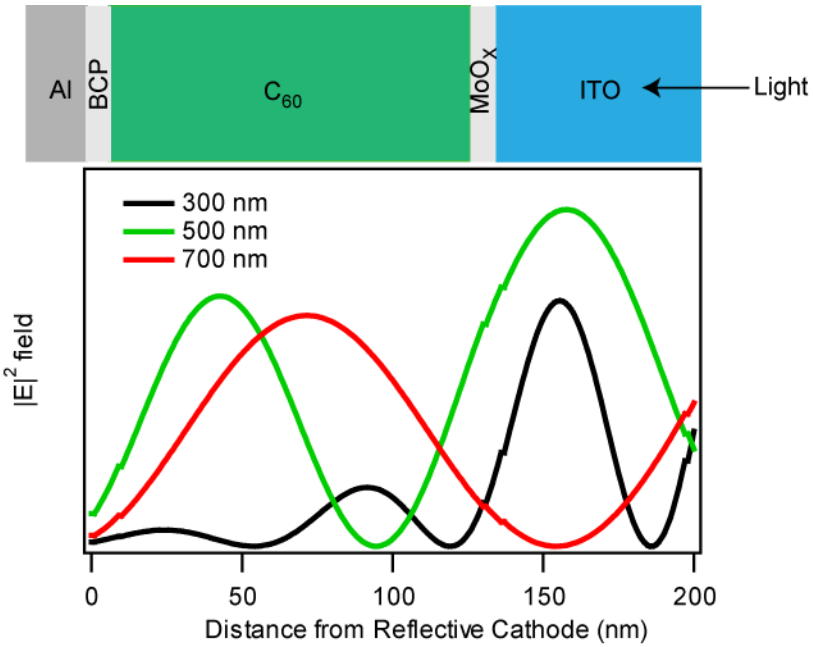

Figure 1.10: Schematic of the electromagnetic field in a typical OPV device, C_{60} is used for simplicity.

Figure 1.10 shows a schematic of the optical field distribution of C_{60} sandwiched between a reflective Al electrode and a transparent ITO electrode. The optical field within the layer is highly dependent upon wavelength, with lower wavelengths (300 nm) peaking multiple times through the layer and longer wavelengths (700 nm) peaking a single time. The position of the optical field peak also varies with wavelength with longer wavelengths peaking further from the reflective electrode. Due to this optical interference effect, small molecule tandem OPV devices tend to have an unconventional sub-cell structure with the small band gap, long wavelength absorbing sub-cell placed first in the incident light path to align it with the optical field.[23]

In OPV devices, the photoactive layer is usually placed next to the reflective cathode with only a small exciton blocking layer between them. In this region, usually ~10 nm away from electrode, the optical field is low resulting in low absorptance. A way

to increase the absorptance is to add a thicker optical spacer layer between the reflecting electrode and the photoactive layer to push the absorbing layer into a peak in the optical field. This has been achieved using transparent metal oxide layers in polymer OPV devices [72,73] and metal doped exciton blocking layers in small molecule vacuum deposited OPVs.[74,75] Another device concept is the a p-i-n OPV device which has p and n-doped wide band gap transport layers on either side of an intrinsic photoactive layer, allowing for the photoactive layer to be tuned into an optical field maximum resulting in high absorptance.[20]

In small molecule tandem OPV devices an optical spacer provides a tool to position each sub-cell in an optical field peak and tune for photocurrent balancing. With thick BHJ photoactive layers, the second sub-cell (furthest from the reflective cathode) cannot be positioned in the first optical field peak, therefore an optical spacer must be used between the two sub-cells to position the second sub-cell in an optical field maxima. By tuning the optical spacer and photoactive layer thickness with optical modelling a balancing of the sub-cell photocurrents can be achieved.

1.8 Cascade OPV devices

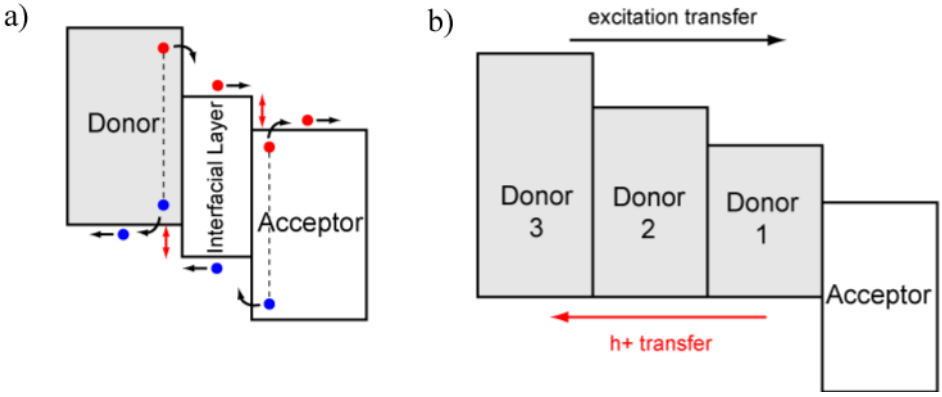

Figure 1.11: a) Energy level schematic of a cascade OPV device. Blue dots represent holes, red dots represent electrons. b) Energy level schematic of a multiple donor cascade OPV device.

A cascade OPV device employs an interfacial layer at the D / A interface that separates the electrons and holes. To ensure exciton dissociation still occurs, the energy levels of the interfacial layer are chosen to form a cascade in energy levels from the donor to the acceptor (Figure 1.11a).[76] The HOMO and LUMO levels must be in between the corresponding HOMO and LUMO levels of the donor and acceptor. The interfacial layer helps to dissociate excitons by a two-step process: the first dissociates the excitons, and the second dissociates the bound charge transfer (CT) state.[77] The interfacial layer can also increase J_{SC} by improving the exciton dissociation and by broadening the spectral coverage. The first demonstration of a cascade device was produced by Sista et al. who used a CuPc interfacial layer in-between a tetraceno-[2,3-b]-thiophene (TT) donor and C_{60} acceptor.[78] An increase in V_{OC} was seen from 0.31 V for the TT / C_{60} device to 0.56 V for a 13 nm CuPc layer cascade device.

Other types of cascade OPV device have been produced that have multiple donor layers (Figure 1.11b). Each of these layers absorbs light then transfer the excitons to the D / A interface through the energy ordering of the excitonic states. This has been

presented for a diphenyl-tetracene, tetracene and ruberene structure giving a V_{OC} of 0.74 V compared to the 0.54 V of the bilayer device.[79] This multiple donor structure is effective for increasing the optical bandwidth of an OPV device.[80,81]

One final type of cascade OPV device is based upon a photocurrent contributing interfacial layer in-between the donor and acceptor. Excitons created in this layer can dissociate at each interface with the donor and acceptor. This was demonstrated by Cnops et al. for a tetracene / SubPc / C_{60} device.[53] The SubPc could dissociate excitons at the tetracene / SubPc and the SubPc / C_{60} interface. An increase from 5.67 mA cm^{-2} to 6.36 mA cm^{-2} was seen when comparing the SubPc / C_{60} device and the cascade structure. This type of cascade device is investigated in Chapter 5.

1.9 Outline of Thesis

In this thesis the design and optimisation of multi-heterojunction OPV device architectures is investigated. Chapter 2 covers the material properties of the organic semiconductors used in the thesis and the experimental techniques used in fabricating and analysing the OPV devices.

Chapter 3 looks at the formation of a tandem OPV device with a broad spectral coverage by selection of a red and green absorbing phthalocyanine based material. The optimisation of a Ag recombination layer is investigated by looking at the layer and device properties for different thicknesses and deposition conditions. Once the optimum recombination layer is found, modification of the sub-cell photoactive layer is performed to improve the device performance. Co-deposition of the photoactive layers is then used to increase the photocurrent generation, and is investigated in single heterojunction devices and then implemented in tandem devices. Finally, the addition of a structural templating perylene-3,4,9,10-tetracarboxylic dianhydride (PTCDA) layer is investigated as a method to increase charge transport in the phthalocyanine layer.

The focus in Chapter 4 is on the use of an optical spacer layer in OPV devices. α-NPD is chosen as the hole transporting optical spacer material and its optical, electrical and morphological properties are investigated along with co-deposition with MoO_x as a method to increase the mobility of α-NPD. The hole transporting and optical spacing properties of the layer are then investigated by implementing the α-NPD layer in single heterojunction OPV devices. Finally, the optical spacer layer is used in tandem OPV devices as a tool to balance sub-cell photocurrents by positioning the sub-cells within the optical field.

Chapter 5 presents another method for improving the photocurrent in a planar heterojunction (PHJ) OPV device by the design of a multi-heterojunction cascade device. α-6T is used to create the cascade device with a phthalocyanine / C_{60} heterojunction. Photoluminescence quenching is used to show exciton dissociation at this new heterojunction and the device properties of the dual heterojunction cascade system are shown.

Finally, conclusions are made and directions for further work discussed.

Chapter 2 Materials and Experimental Methods

2.1 Materials

This section will outline the history and properties of the materials used in this thesis. The focus will be on the photoactive materials which are classed into two categories, electron donors and electron acceptors, and the transport layers.

2.1.1 Electron Donor Materials

2.1.1.1 Aluminium Phthalocyanine Chloride

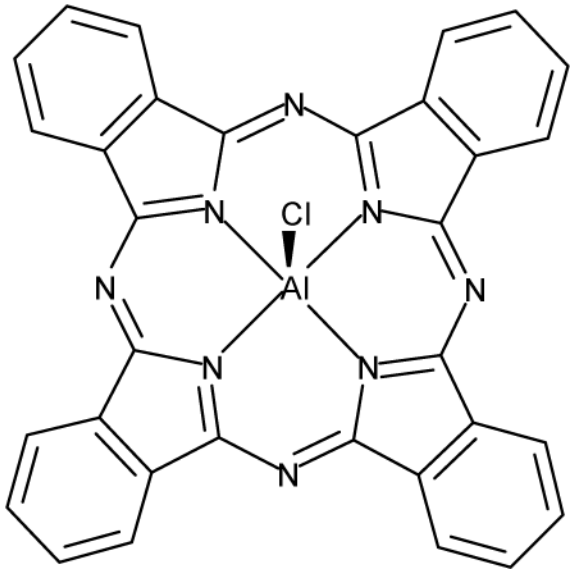

Figure 2.1: The molecular structure of Aluminium Phthalocyanine Chloride (ClAlPc).

Phthalocyanines were discovered in 1928 and have been used as a class of common dyes and colorant.[82] More recently, they have been employed as functional materials in organic electronics such as organic field effect transistors (OFET) and OPV.[10,83] Phthalocyanines are a general class of macrocyclic material with a large 18 π electron system. They contain a central metal atom surrounded by a tetrameric ligand formed from diiminoisoindoline units with the four central nitrogens ligating

the metal. Most metals form phthalocyanines by templating the formation of the ligand during the reaction of the metal halide with phthalonitrile. Phthalocyanines are chemically and thermally stable and can be thermally evaporated. Functionalisation of the chelating ligand can alter the properties of the phthalocyanine, shifting the electronic structure through halogenation[84] or by adding groups to increase solubility.[85]

Due to the relatively weak $\pi - \pi$ interaction between phthalocyanines they are able to form different crystal polymorphs with the α- (monoclinic) and β- (triclinic) forms usually present in thin films. In planar phthalocyanines the α- phase tends to occur on non-interacting substrates at room temperature, while deposition onto elevated temperature substrates, above the phase transition temperature, can lead to the thermodynamically favourable β- phase. The main intermolecular interaction between the phthalocyanines is the face on $\pi - \pi$ overlap. This causes anisotropic charge transport in the material, which in phthalocyanine films on ITO occurs parallel to the substrate.

Aluminium phthalocyanine chloride (ClAlPc) (shown in Figure 2.1), is a non-planar phthalocyanine with an axial chlorine atom attached to the central aluminium. It has been shown to adopt an α- and β- phase, although the non-planar molecule causes the structure to be largely amorphous.[86,87] Deposition onto elevated temperature substrates has been shown to improve crystallinity and induce a switch between crystal phases.[88] Solvent annealing [89] and deposition onto templating layers can also change the molecular packing. PTCDA[90] or graphene[91] can be used to template the growth of ClAlPc so the molecule lies parallel to the substrate and the π – stacking direction is perpendicular to the substrate, a favourable charge transporting channel for OPVs, as shown in Figure 2.2.

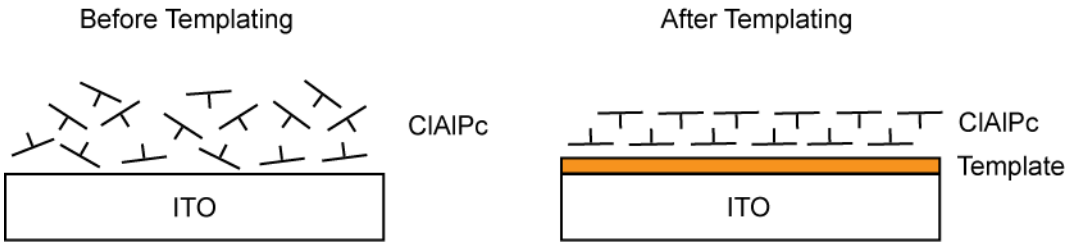

Figure 2.2: Schematic of the proposed molecular packing structure of ClAlPc on ITO and on a structural template adapted from Reference[91].

ClAlPc has two main absorption peaks similar to other phthalocyanines. A low energy Q-band absorbs between 600 and 800 nm with a Soret B band at 350 nm.[86] The absorption into the near infrared makes ClAlPc promising for increasing the spectral coverage in OPVs[92] and its use in tandem OPVs.[93] ClAlPc has a HOMO level of 5.4 eV and a LUMO level of 3.5 eV making it an appropriate electron donor for use with fullerenes.[92]

2.1.1.2 Boron Subphthalocyanine Chloride

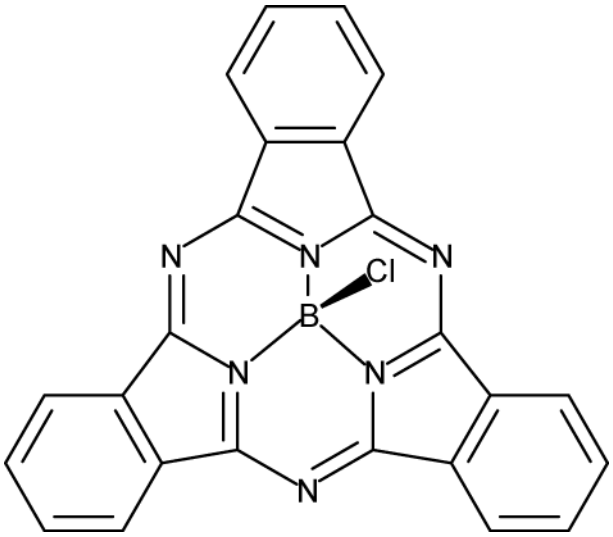

Figure 2.3: The molecular structure of Boron Subphthalocyanine Chloride**.**

Boron subphthalocyanine chloride was accidentally synthesised in 1972 by Meller et al. while attempting to make boron phthalocyanine.[94] Boron has the smallest atomic radius of all the metalloids and this allows for the smaller trimeric homologue of phthalocyanine to be created. The boron is chelated by three pyrrole nitrogens that form part of the diiminoisoindoline ligand creating a 14π electron system. The molecule adopts a non-planar bowl structure as boron is slightly larger than the cavity created.[95]

SubPc absorbs in the visible region of the spectrum. The main low energy absorption band known as the Q-band absorbs from 500-600 nm equating to a band gap of ~2 eV. The Q-band is slightly blue shifted to regular Pcs as a consequence of the reduction in the π conjugated system and corresponds to π-π^* transitions on the C-N backbone.[96] The spectrum also shows absorption from a Soret B band below 400 nm. Boron subphthalocyanine chloride (Figure 2.3) is used as an electron donor with a HOMO level of 5.6 eV and a LUMO level of 3.6 eV.[97] Halogenation of the active site on the diiminoisoindoline ligand can shift the energy levels of the material to act as an electron acceptor.[98] SubPc adopts an amorphous thin film structure due to the weak intermolecular interactions between the non-planar SubPc molecules, leading to considerably lower charge mobility.[99]

2.1.2 Electron Acceptor Materials

2.1.2.1 C_{60}

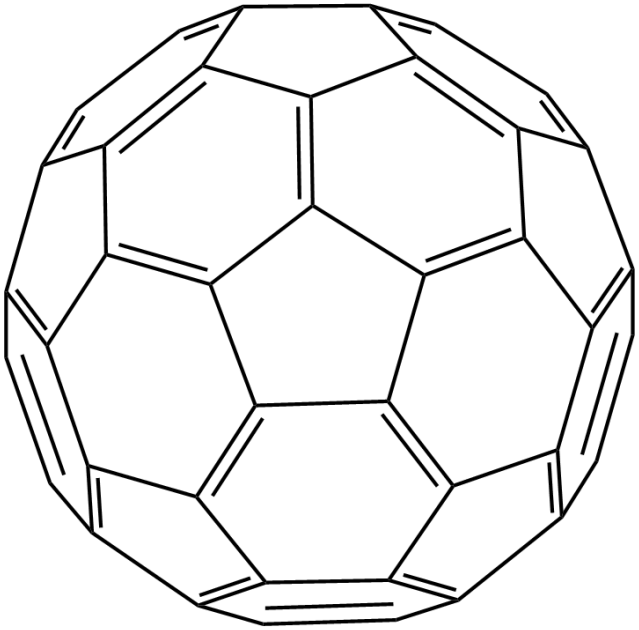

Figure 2.4: The molecular structure of Fullerene (C_{60}).

The only electron acceptor used in this thesis was fullerene, which is an allotrope of carbon consisting of a hollow spherical structure. The smallest fullerene is C_{60} (Figure 2.4) which was discovered by Kroto et al. when investigating carbon chains in interstellar space.[100] The spherical carbon ball consisting of a pattern of pentagons and hexagons was named after Buckminster Fuller due to the similarity between the molecular structure and his geodesic dome architecture. In C_{60} all of the carbons are connected by one double and two single bonds each leading to sp^2 hybridisation. However, the strain from curvature of the spherical structure forces the molecule to adopt an intermediate hybridisation between trigonal sp^2 and tetrahedral sp^3. This makes it susceptible to reactions that saturate the surface, leading to sp^3 hybridisation, e.g. reaction with oxygen.[101]

The extended conjugated π system of C_{60} allows it to accept between 6 and 12 electrons making it a good electron acceptor material.[102] The absorption of C_{60} is dominated by a parity allowed transition below 410 nm in the UV region and a weaker absorption at lower energies up to 650 nm, related to a forbidden transition.[103] C_{60} has a HOMO level of 6.2 eV and a LUMO level of 4.5 eV making it an appropriate electron acceptor for phthalocyanines in OPV devices.[11] The low absorption in the visible region has led to the use of the less symmetric C_{70} fullerene in OPV devices, which has allowed transitions and strong absorption in the visible region.[104]

The spherical nature the molecule leads it to have no preferential orientation in the solid state. Due to the weak intermolecular interactions C_{60} is mainly amorphous in thin films with some crystalline domains.[105]

2.1.3 Organic Transport Layers

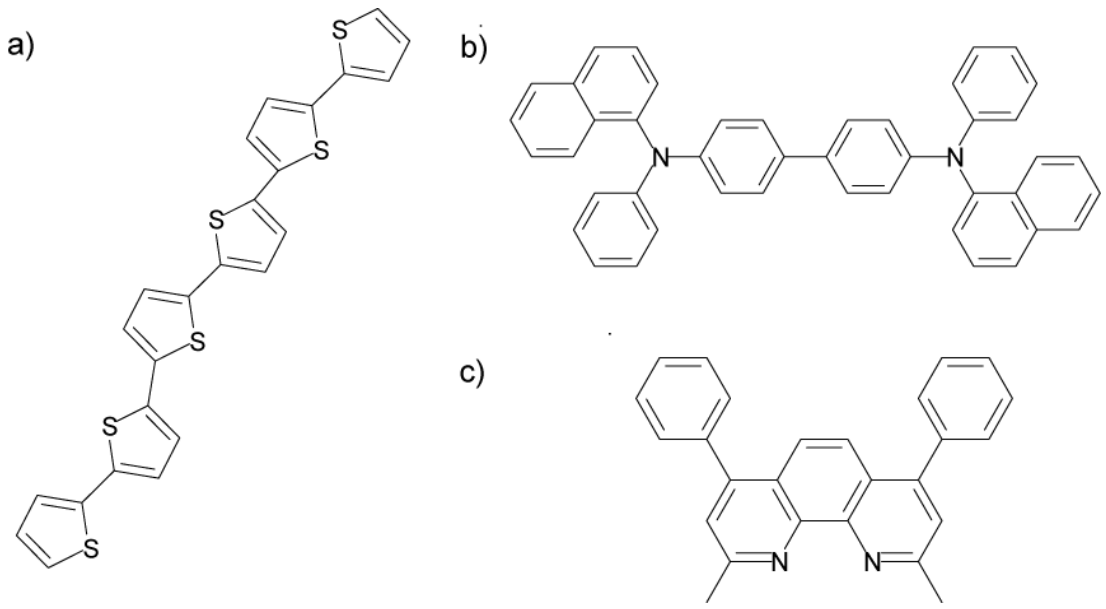

Figure 2.5: The molecular structure of **a)** α-sexithiophene **b)** α-NPD **c)** bathocuproine (BCP).

2.1.3.1 α-sexithiophene

α-sexithiophene (α-6T) is a six ring α linked thiophene oligomer which was first synthesised in 1947 by Sease et al.[106] and its molecular structure is shown in Figure 2.5a. In the 1980s to 90s oligothiophenes became an important class of materials due to their potential for opto-electronic devices.[107] The large interest in α-6T came with the discovery of the favourable charge transport in films[108] and the use in an p type OFET.[109] α-6T was also used in the first all-organic FET on a plastic substrate signalling the start of the organic electronics era.[110] The extended π conjugation of the chain gives the material a high hole mobility and as the molecules are deposited in a standing up orientation on a substrate, the charge transport occurs parallel to the substrate plane. Deposition at room temperature gives mobilities of 2 x 10^{-3} $cm^2V^{-1}s^{-1}$, small 50 nm sized crystallites, and when deposited on heated substrates, larger crystallites are formed leading to mobilities of up to 2.5 x 10^{-2} $cm^2V^{-1}s^{-1}$.[107]

Mechanically rubbing the substrate can change the stacking direction of the thiophene, moving it to a lying down formation with charge transport perpendicular to the substrate.[111] α-6T has also been used as an electron donor for OPV devices with C_{60} achieving an efficiency of 2.0 %.[112] The efficiency is limited by the large 2.2 eV band gap of α-6T which absorbs from 350 – 500 nm.

2.1.3.2 α-NPD

N,N'-diphenyl-N,N'-bis(1-naphthyl)-1,1'-biphenyl-4,4'-diamine (α-NPD, Figure 2.5b) was first used by Van Slyke et al.[113] as a hole transport layer in early OLED devices. It led to an improved operational lifetime due to the stability of the bulky molecule and its glass transition temperature (T_g) of 95°C. The hole mobility of α-NPD has been measured at 8.8 x 10^{-4} $cm^2V^{-1}s^{-1}$ with improved mobility achieved by electrically doping the material.[114,115] α-NPD has also been used as an electron donor in OPV devices by doping it with MoO_X to improve the charge transport.[116] Thin films of α-NPD on ITO have an amorphous structure with a surface roughness of 0.35 nm.[117] The wide band gap of 3.1 eV (absorbing in the UV) and the suitable energy level alignment of the 5.5 eV HOMO level with the phthalocyanine electron donors make it a suitable hole transport layer for OPV devices.

2.1.3.3 Bathocuproine (BCP)

2,9-dimethyl-4,7-diphenyl-1,10-phenanthroline (bathocuproine, BCP, Figure 2.5c) is deposited onto the acceptor layer under the metal cathode. The wide band gap of 3.5 eV allows it to have exciton blocking properties, stopping quenching of excitons at the acceptor/cathode interface and enhancing OPV efficiency.[11] The BCP also provides protection for the photoactive layers from the deposition of hot metal clusters during formation of the electrode. Due to the wide band gap, electron

transport through this layer has been proposed to occur through defect states induced by the metal electrode deposition.[118]

2.2 Experimental

2.2.1 Material Purification

Due to the negative effect of material impurities (e.g. residual solvent and by-products from synthesis) on PV performance, most organic materials used in this thesis were purified by vacuum gradient sublimation before use.[119]

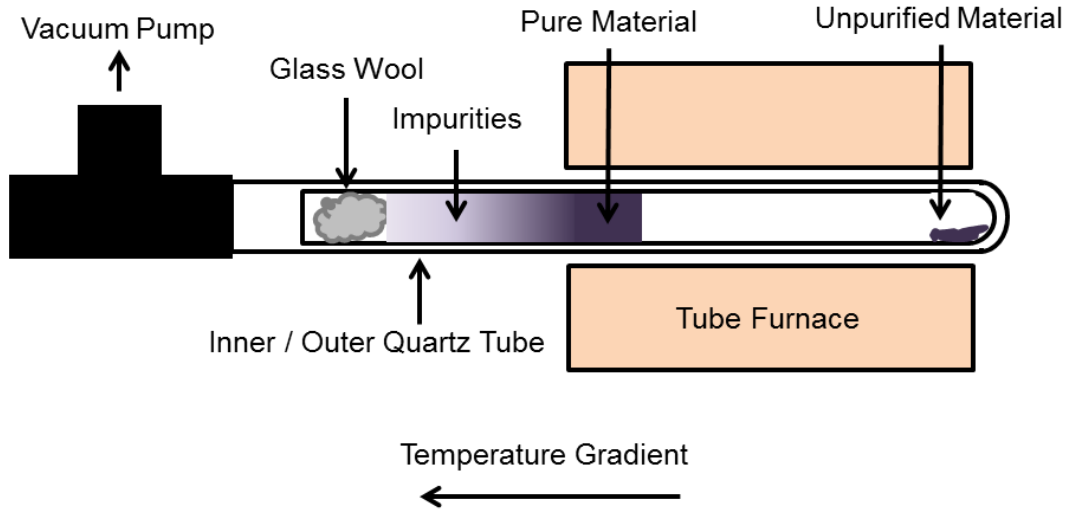

Figure 2.6: Schematic of the vacuum gradient sublimation tool.

The vacuum sublimation system is displayed in Figure 2.6. It consists of a horizontal quartz tube which is placed inside a tube furnace and connected to a turbo molecular pump. An inner tube contains the unpurified material with glass wool to trap material from entering the pumping system. Purification is carried out at ~10^{-5} mbar with a temperature gradient created along the tube from the external tube furnace. The tube furnace temperature is raised at 1 °C min^{-1} and held at sublimation

temperature for at least 10 hours depending upon the material being purified. The unpurified material sublimes and condenses at a lower temperature along the tube separating the low temperature volatile impurities from the pure material. The inner tube is then removed from the system, cut open, and the pure fraction is removed for use. A table of the organic materials and the purification parameters are shown in Table 2.1.

Organic Material	Purification runs	Temperature / °C
C_{60} 99.5% nano-c inc	1 x	500
SubPc Sigma Aldrich 85 %	1 x	350
SubPc Lumtec 99% sublimed	not purified	-
ClAlPc Sigma Aldrich	2 x	350
α-NPD % Sigma Aldrich	1 x	350
α-6T Sigma Aldrich	1 x	350
BCP Sigma Aldrich	not purified	-

Table 2.1: Purification parameters for different materials used in vacuum gradient sublimation

All of the inorganic materials were used as received; MoO_3 (Sigma Aldrich, 99.99%), Ag (Sigma Aldrich, 99.9999%) and Al (Sigma Aldrich, 99.999%).

2.2.2 Sample Preparation

For all of the substrates; ITO coated glass for devices and AFM, and quartz glass for absorption, the same cleaning procedure was used. The substrates were cleaned using the following process: sonication in (20:80) decon:water mix, rinse in water,

sonication in water, rinse in propan-2-ol, sonication in propan-2-ol, dry blowing with nitrogen and 20 minutes UV-ozone treatment. UV-ozone treatment removes any carbon residues left after cleaning.[120] All sonication was carried out for 15 minutes in an ultrasonic bath.

2.2.2.1 Organic Molecular Beam Deposition (OMBD)

OMBD is a thermal evaporation process of highly pure material in a background vacuum of typically below 10^{-6} mbar. It is a widely used deposition technique for small molecules that have low solubility. OMBD allows for sub-nanometre accurate control of molecular thin film thickness and deposition rates, measurable down to 0.1 $Å s^{-1}$. With the high vacuum environment, OMBD provides a clean environment for the growth of films as the deposition rates are higher than the adsorption rate of contaminates.

The deposition of organic semiconductors occurs via thermal evaporation in a Knudsen cell based evaporation source, as shown in Figure 2.7. A purified material is placed in a boron nitride crucible and heated with a resistive coil up to $500^{o}C$, monitored by a thermocouple. A heat shield is used to reduce any thermal gradient within the crucible and a molecular beam is formed out of the small aperture in the evaporation source.

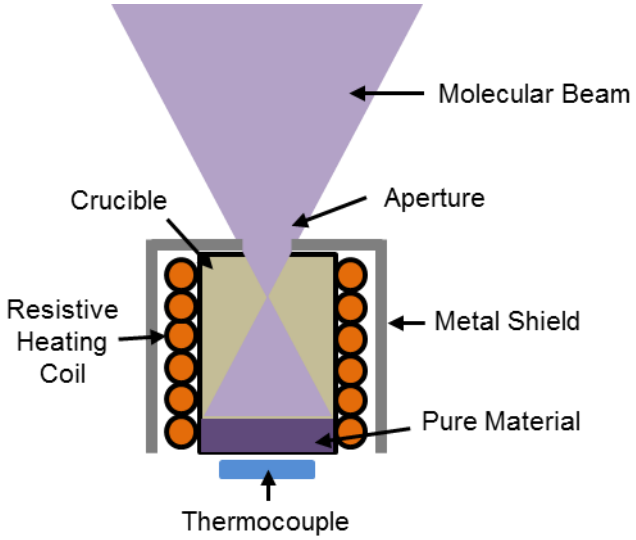

Figure 2.7: Schematic diagram of a evaporation source and formation of molecular beam.

The substrates are placed in the path of the beam and molecules adsorb onto the surface to create a thin film. The deposition rate is controlled by the evaporation source temperature and PID feedback monitoring using quartz crystal microbalances (QCM) placed in the beam path. The film thickness is controlled by an evaporation source shutter which acts as an "on/off" switch for the molecular beam. The film thickness monitored by the QCM has to be calibrated to a real film thickness due to the different densities of the organic materials and the geometry of the evaporation source to the substrate. Calibration using ex-situ AFM step edges is discussed in section 2.2.3.1.

2.2.2.2 OMBD Chamber

A Kurt J. Lesker Spectros vacuum deposition system was used for growth of all thin films and devices. A schematic of the growth chamber is shown in Figure 2.8. The high vacuum environment is created and maintained by a two stage pump system. A scroll pump is used to create a modest vacuum of 10^{-1} mbar and then a cryogenic pump (CryoTorr) is used to further reduce the pressure to the base pressure of $< 10^{-7}$ mbar. The growth chamber contains eight individually controlled organic deposition sources and three metal sources. These are monitored by four QCMs for the organic sources and one for the metal sources. The organic sources allow for single source growth and co-deposition with a main substrate shutter to control the layer thickness and individual source shutters to stop cross contamination. The source temperature is controlled by a Eurotherm Mini8® controller interfaced with a computer and the QCMs are interfaced with Sigma Instruments SQS-242 software to monitor the deposition rate and film thickness. The organic layers were deposited at rates between 0.5 to 1 $Å s^{-1}$.

The samples sit in a sample holder which can accommodate up to 36 substrates that can be shadow masked for deposition of different layers. The sample holders and masks sit in a cassette holder, which holds up to three masks allowing for a complete OPV device to be fabricated without breaking vacuum. Between layer growths the masks are manipulated using a computer controlled transfer arm. The cassette shelf is rotated during the growth to allow for homogeneous deposition. All of the substrates and organic materials are handled under an inert atmosphere from a N_2 glovebox attached to the vacuum chamber due to their sensitivity to oxygen and moisture. The glovebox was maintained at < 10 ppm O_2 and H_2O.

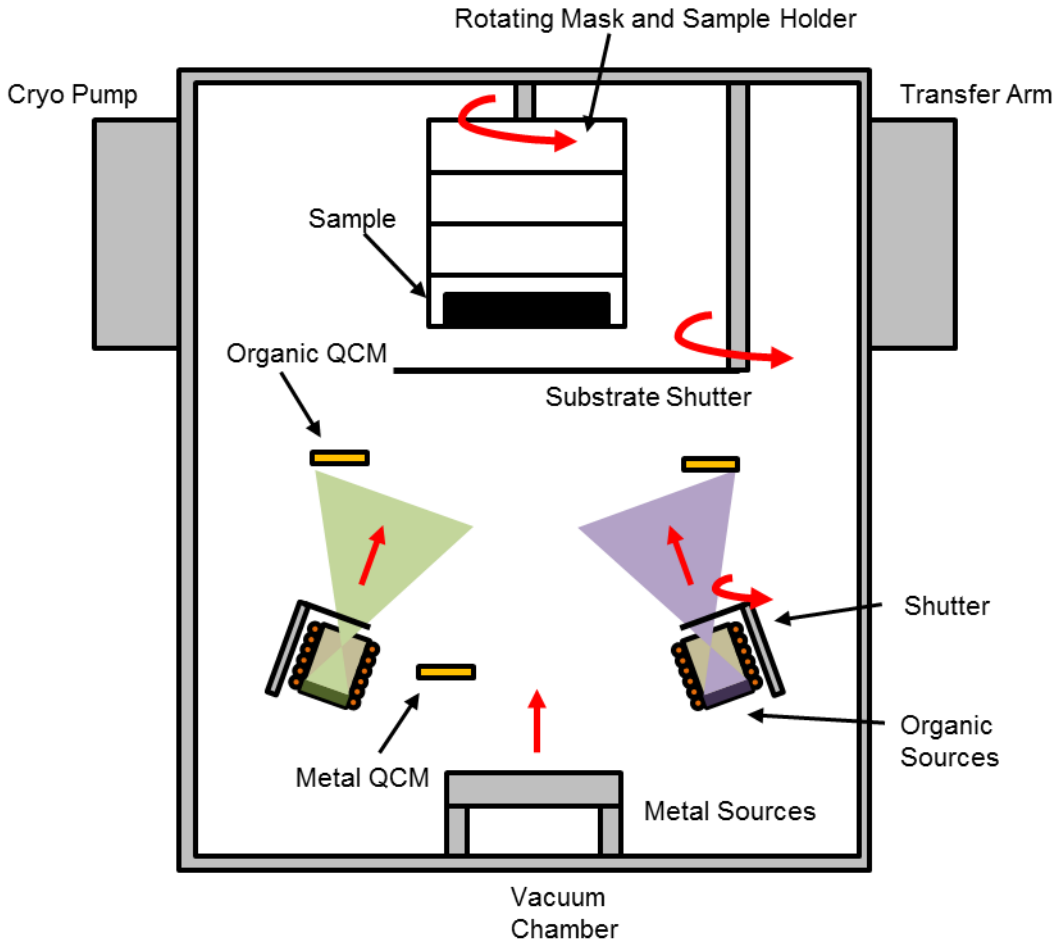

Figure 2.8: Schematic of the Kurt J. Lesker OMBD vacuum chamber.

2.2.2.3 Metal Deposition

Deposition of the MoO_x layer, the top Al cathode and the Ag recombination layer was performed from a high temperature metal source. These are designed differently to organic sources and consist of a heat shielded tantalum crucible heater which is resistively heated by passing high currents at a low voltage. A metal (Al or Ag) pellet is placed in a crucible inside the heater and the current is increased until evaporation is seen, with the deposition rate controlled by the current flow. The first few nanometres of the metal layer are deposited at a low rate of < 1 $Å s^{-1}$ to avoid

damage of the underlying organic layers by the hot metal. The rate was later increased to 2 $Å s^{-1}$ for the remaining deposition of the Al pellet, to a thickness of ~200 nm.

2.2.2.4 Device Design

The ITO substrates used for layer and device growth are supplied by Thin Films Devices Inc. with a sheet resistance of < 15 Ωsq^{-1}. The substrates are 1.2 x 1.2 cm^2 with a 0.8 cm pre patterned strip of ITO, as displayed in Figure 2.9a. The organic layers and the metal cathode areas are defined by using different shadow masks. Figure 2.9b shows the organic layers deposited onto the ITO substrate, leaving a small strip to make the ITO anode contact. Figure 2.9c presents the OPV device configuration used throughout this thesis. Three cathodes are deposited onto each sample through 0.2 cm wide shadow masks with the device area of the OPV determined by the overlap of the ITO and the metal electrode, giving a pixel area of 0.16 cm^2. Silver conductive paint was used to create the ITO contact and improve the connections from the electrodes to the *J-V* testing holder.

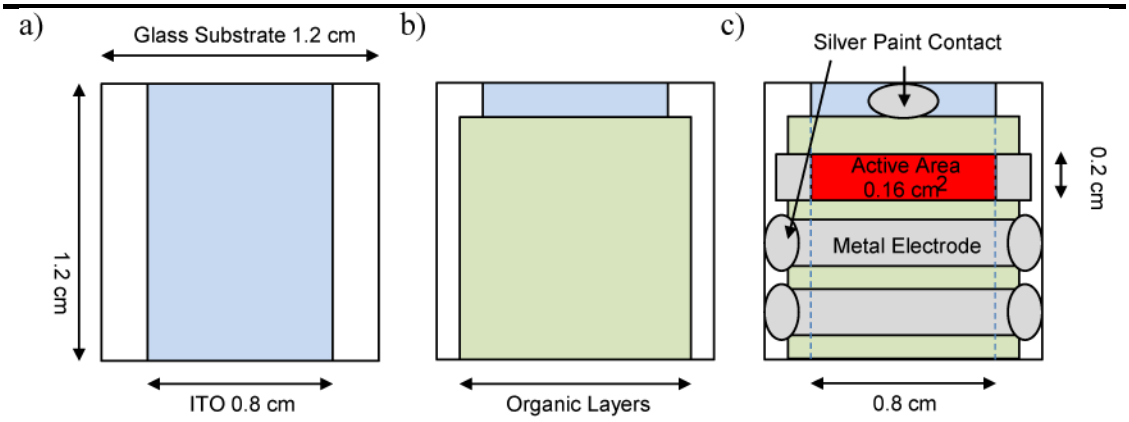

Figure 2.9: Schematic diagrams of a) ITO substrate, b) organic layer on ITO, and c) complete device with metal electrodes displaying active area.

2.2.3 Ex situ characterisation

2.2.3.1 Atomic Force Microscopy

Atomic force microscopy (AFM) was invented in 1986 by Binnig, Quate and Gerber from the previous development of scanning tunnelling microscopy (STM).[121] STM is based upon a conductive scanning tip under applied bias, which measures tunnelling currents from a conductive sample with atomic resolution. The nature of this technique limits the surfaces that can be analysed. AFM is a more versatile technique as it is also able to study non-conductive surfaces with a nanometer spatial resolution to image the surface topography.

AFM is based upon the intermolecular forces between a tip and a surface as they are brought into close proximity. The tip experiences attractive and repulsive forces depending upon distance to the surface. At longer tip – surface separation, the tip experiences attractive van der Waals and capillary forces and at closer separation, electrostatic Coulombic repulsion. The AFM tip is attached to a cantilever which acts as a spring. As the tip is subject to tip-surface forces the cantilever deflects to allow the tip to reduce its potential energy. Attractive forces bend the cantilever towards the surface and repulsive forces deflect it away. A laser beam is reflected off the back of the cantilever and detected by a position sensitive photodiode. The position of the beam on the photodiode is dependent upon the deflection of the cantilever which is related to the force acting on the tip and can be calculated using Hooke's law. The tip is scanned across the surface in two dimensions using separate x and y piezoelectric elements while the tip position is moved vertically using a Z-piezo to maintain a constant height above the sample, which generates the topographical image. A schematic diagram of the AFM setup is shown in Figure 2.10a.

Tapping mode was used to image the organic films, which is a less damaging mode compared to contact mode as the tip is tapped above the surface rather than dragged across it. The cantilever is oscillated close to its resonant frequency by a piezoelectric crystal with measured amplitude. As the tip is brought close to the surface it enters the repulsive force regime in the lower part of the oscillation. This reduces the oscillation amplitude as measured by the photodiode and is related to the tip-surface separation. As the tip is scanned across the sample surface, the height of the tip is adjusted by the Z-piezo to maintain the oscillation amplitude at a desired set point. This displacement of the tip in the Z-direction is equivalent to the height of the feature on the sample surface generating a 3D topographical image of the surface.

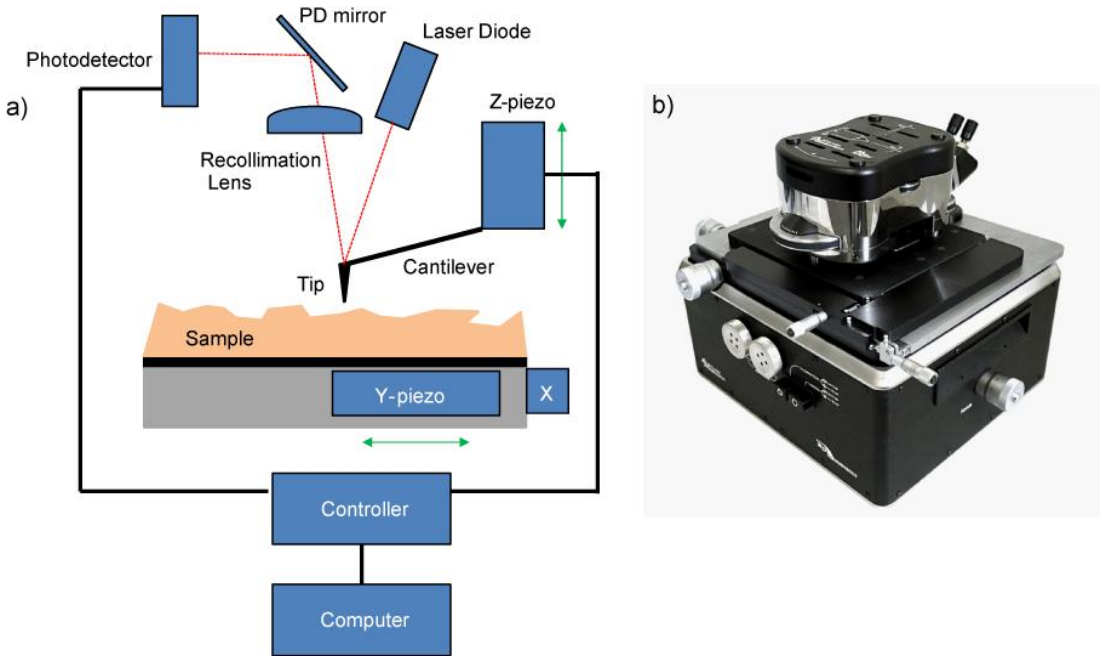

Figure 2.10: a) Schematic of the AFM set up. b) Image of the set-up taken from the Asylum MFP-3D manual.[122]

The AFM images are captured using an Asylum Research MFP-3D (Figure 2.10b) in tapping mode. Commercially available tapping mode tips were used (AC240TS)

with a resonant frequency of 70 kHz and a tip radius of 9 nm. Asylum Research MFP-3D software was used to present and analyse the images. All of the AFM images have been line and plane filtered. For further topographical analysis, the surface roughness parameter, R_q, was calculated using the software. It is defined as the root mean square of the deviation of each point Z_i from the average height Z_{avg} over all N points of the surface, as shown in Equation 2.1.

$$R_q = \sqrt{\frac{1}{N}\sum_{i=1}^{N}(Z_i - Z_{avg})^2} \qquad \text{(Equation. 2.1)}$$

AFM is used for film thickness calibration by step edge analysis of a grown thin film. A thin film of the desired material is deposited onto a substrate with a specific QCM thickness measured during the film deposition. The film is then scratched with a needle to generate a well-defined step edge. An AFM scan is set up across the edge of the scratch analysing the height difference between the substrate and the film as shown in Figure 2.11a and b. The film thickness is then calculated using statistical height distribution analysis (Figure 2.11c). Multiple scans of step edges are performed across different samples of the same film growth and averaged to find the film thickness.

The ratio between the AFM height and the QCM film thickness is referred to as the tooling factor which is specific to the deposition position and material. The tooling factor is inputted into the deposition QCM monitoring system for thin film deposition accuracy.

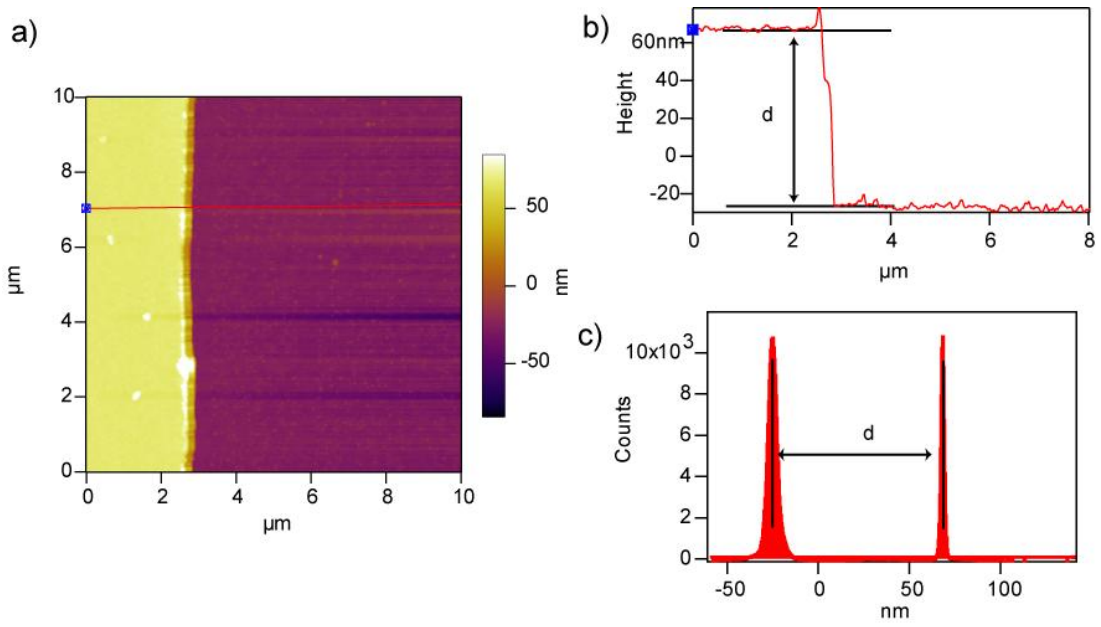

Figure 2.11: a) AFM step edge image of an Ag film with a QCM thickness of 80nm. b) Cross-section height profile of the Ag step edge with thickness d. c) Histogram plot of height distribution of Ag step edge with thickness d.

2.2.3.2 Absorption Spectroscopy

The transmission of light through a sample is quantified by the ratio of the incident radiation intensity $I_0(\lambda)$ to the radiation intensity $I(\lambda)$ leaving the sample.

$$T(\lambda) = \frac{I}{I_0} = 10^{-\varepsilon(\lambda)lc} = 10^{-\alpha(\lambda)d} \qquad \text{(Equation 2.2)}$$

The Beer-Lambert law relates the logarithmic dependence of $T(\lambda)$ to the molar absorption coefficient $\varepsilon(\lambda)$, the path length l and the solution concentration c. For thin films, the concentration of the solid is obtained by the product of the relative molecular mass and the density. The molar absorption coefficient and the concentration can be combined to obtain the absorptivity $\alpha(\lambda)$ and d is the film thickness. The absorbance A can also be defined by the Beer-Lambert Law and

scales linearly with $\varepsilon(\lambda)$, l and c as well as $\alpha(\lambda)$ and d for liquids and solids respectively (Equation 2.3).

$$A(\lambda) = log\left(\frac{I_0}{I}\right) = \varepsilon(\lambda)lc = \alpha(\lambda)d \qquad \text{(Equation 2.3)}$$

Absorbance and absorptance are sometimes mistaken. Absorbance is a measure of all light that is not transmitted and has a logarithmic ratio whereas absorptance is the fraction of light that is absorbed in a layer, taking into account reflectance and has a linear ratio (Equation 2.4). Absorptance is a useful quantity in the optical modelling (Section 2.2.2.3).

$$Abs = 1 - T - R \qquad \text{(Equation 2.4)}$$

Absorption and transmission spectra for this thesis were measured on a Perkin Elmer Lambda 25 spectrometer. All spectra were measured between 300 – 900 nm with a 1 nm resolution. The samples were measured on quartz glass with the spectra corrected for substrate absorption.

2.2.3.3 Transfer Matrix Simulations

Transfer matrix simulations can be used to calculate the η_A as it is dependent upon the optical properties of the material, the layer thickness and the layer configuration in a device. The transfer matrix formalism described by Pettersson et al. can be used to calculate the reflectance, transmittance and absorption of a device as well as the optical electric field and absorptance for any given wavelength, at any point in the device.[123]

The photon absorptance calculated for every point in a device produces an absorptance profile. Since the overall *EQE* of a device depends upon the η_A (section 1.6), comparison of the absorptance of a device with the experimentally measured EQE will obtain an estimate for the *IQE*, given by Equation 2.5.

$$IQE = \eta_{ED}\eta_{CT}\eta_{CC} = \frac{EQE}{\eta_A} \qquad \text{(Equation 2.5)}$$

The absorbed photon power, which is related to the exciton generation rate, for AM1.5 incident radiation can be summed over all wavelengths and positions in the photoactive layers of a device to give a maximum limit of the photocurrent. If the *IQE* of a device can be estimated, multiplying the maximum photocurrent by the *IQE* will lead to a short circuit current estimate for the device. This becomes useful in tandem OPV devices, where the photocurrent estimates of each sub-cell can be calculated to improve the current balancing.

In this thesis, the optical simulation program was written by Thomas Howells. The optical constants n & k for each of the organic materials have been obtained from the literature,[96,105] by measurements carried out by Thomas Howells and from L.O.T-Oriel GmbH & Co. KG (Section 4.6) using a variable angle spectroscopic ellipsometer.

2.2.4 OPV device characterisation

Solar cells are characterised by analysing their *J-V* characteristics under dark conditions and in simulated solar illumination. To gain further insight into current generation, the wavelength dependent photocurrent can be measured to give the *EQE*.

2.2.4.1 Simulating the Solar Spectrum

Nuclear fusion within the Sun's core provides a constant supply of energy that is radiated from its surface. The energy spectrum of this phenomenon can be described by Planck's equation for blackbody radiation (Equation 2.6). A blackbody is an ideal absorber of radiation and at high temperatures it emits radiation with a spectral shape that is temperature dependent.

$$E(\lambda, T) = \frac{2hc^2}{\lambda^5}\left(e^{\frac{hc}{\lambda k_B T}} - 1\right)^{-1} \qquad \text{(Equation. 2.6)}$$

In Equation 2.6, the irradiance, $E(\lambda,T)$, is dependent upon the wavelength λ, Planck's constant h, Boltzmann's constant k_B, the speed of light c, and temperature T.

The blackbody spectra for a range of temperatures are displayed in Figure 2.12a. A low emission is shown at 3000 K and with higher temperatures a large emission peak emerges which is shifted towards the higher energy end of the spectrum (lower wavelength).

The solar spectrum can be closely matched to a blackbody at 5760 K as shown in Figure 2.12b. This high temperature emission makes the simulation of the spectrum difficult.

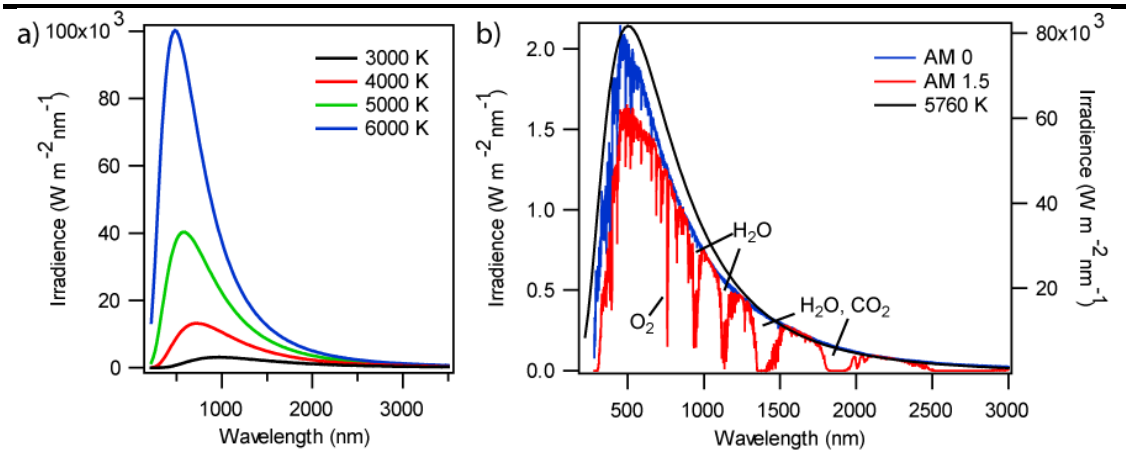

Figure 2.12: a) Blackbody emission at different temperatures: 3000 K, 4000 K, 5000K and 6000K. b) Comparison of the AM 0, AM 1.5 solar spectrum with 5760 K blackbody spectra.

The solar spectrum that reaches the earth's surface is dependent upon its path through the gaseous atmosphere, where absorption and scattering of the light reduces the irradiation and produces features in the spectrum. These features originate from absorption by H_2O, CO_2 and O_2[124] as shown in Figure 2.12b. The path length of the solar radiation through the atmosphere can be written as a function of incident angle (φ) and is defined as an air mass (AM) (Equation 2.7). A schematic diagram for this equation is shown in Figure 2.14.

$$AM = \frac{1}{\cos \varphi} \qquad \text{(Equation. 2.7)}$$

The extra-terrestrial spectra is defined as AM 0, as the radiation passes through no atmosphere resulting in no absorption features (Figure 2.12b). AM 1 is the intensity at φ = 0° when the sun is overhead and the air mass is at its lowest. AM 1.5 and AM 2 are at the angles 48.2 and 60.1 respectively as these have 1.5 and 2 times the path length of AM 1. At AM 1.5 the irradiation intensity is at 1000 Wm^{-2} (quoted 100 $mWcm^{-2}$ in Chapters 3-5).

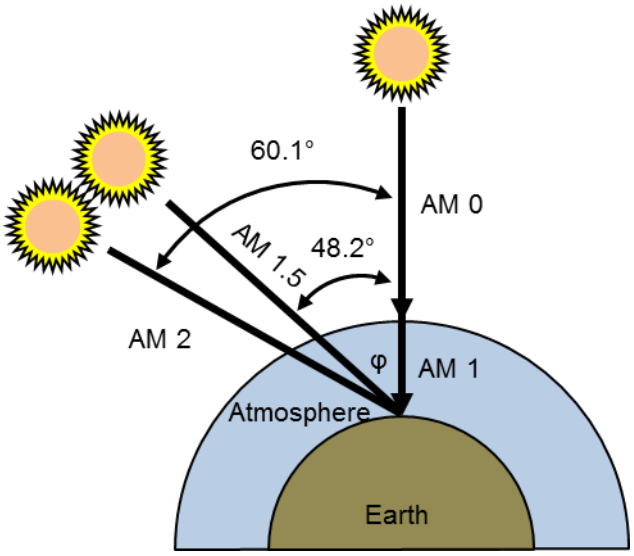

Figure 2.13: Schematic of the angle dependence of AM for φ between the surface of the sun and the earth. AM 0 is measured just outside the atmosphere.

For reproducible characterisation of PV devices the standard test spectrum has been defined as the AM 1.5G spectra, with G representing the global spectra which is a combination of diffuse and direct radiation (including scattering from atmospheric molecules). For the measurement of devices, the AM 1.5G spectra is simulated using a Newport Oriel solar simulator with a xenon arc lamp light source with an AM 1.5G filter. The output of this solar simulator was calibrated to 1 sun intensity (100 $mWcm^{-2}$) using a calibrated Fraunhofer PVM 482 photodiode with a KG-5 filter with no spectral mismatch.

2.2.4.2 *J-V* plots

OPV devices are usually characterised by measuring the *J-V* behaviour in the dark and under simulated solar illumination. Figure 2.14a displays typical *J-V* curves for an OPV device. The device is scanned under applied bias from negative to positive bias (usually from -1 V to 1.5 V) with the current measured at each point. In dark conditions, the ideal device acts as a diode, with no current in negative bias and an

exponential growth in current in positive bias known as the dark current J_{dark} (as shown in Figure 2.14a). Illumination of the device offsets the *J-V* curve due to the production of a photocurrent J_{ph}. The current of the OPV device is a sum of the dark current J_{dark} and the photocurrent J_{ph} with the dark current opposed to the photocurrent.

$$J = J_{dark} - J_{ph} \qquad \text{(Equation. 2.8)}$$

For convention, in this thesis the photocurrent is defined as negative with the operation of the OPV device measured in the fourth quadrant of the *J-V* plot (negative current density, positive bias voltage) as displayed in Figure 2.14a.

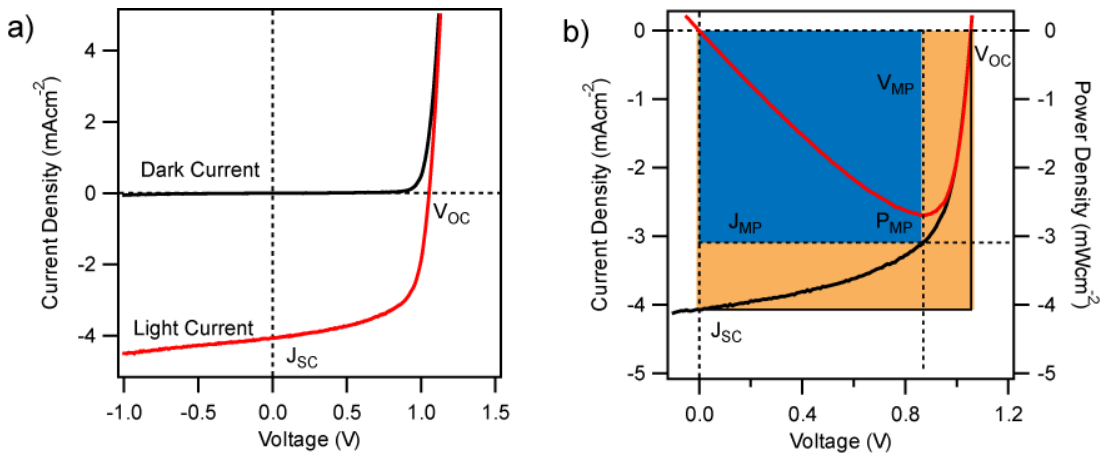

Figure 2.14: a) *J-V* plot of dark and light current of a typical OPV device. b) Power density plot explaining the *FF* of an OPV device.

OPV devices are assumed to be non-ideal diodes due to the nature of the materials and the thin film fabrication process. This can cause shorts, current leakage and poor contacts leading to non-ideal shunt and series resistance. The *J-V* behaviour of the OPV device can be approximated by the generalised Shockley equation (Equation 2.9),[48] which can be represented as an electric circuit, Figure 2.15, with a current

generator in parallel to an opposing diode and two parasitic resistances. One parallel (R_{SH} due to leaks and pinholes) and one in series (R_S) due to the contact resistance.

$$J(V) = \frac{R_{SH}}{R_S+R_{SH}}\left[J_S\left(e^{\frac{q(V-JR_S)}{nk_bT}}-1\right)+\frac{V}{R_{SH}}\right]-J_{ph} \qquad \text{Equation 2.9}$$

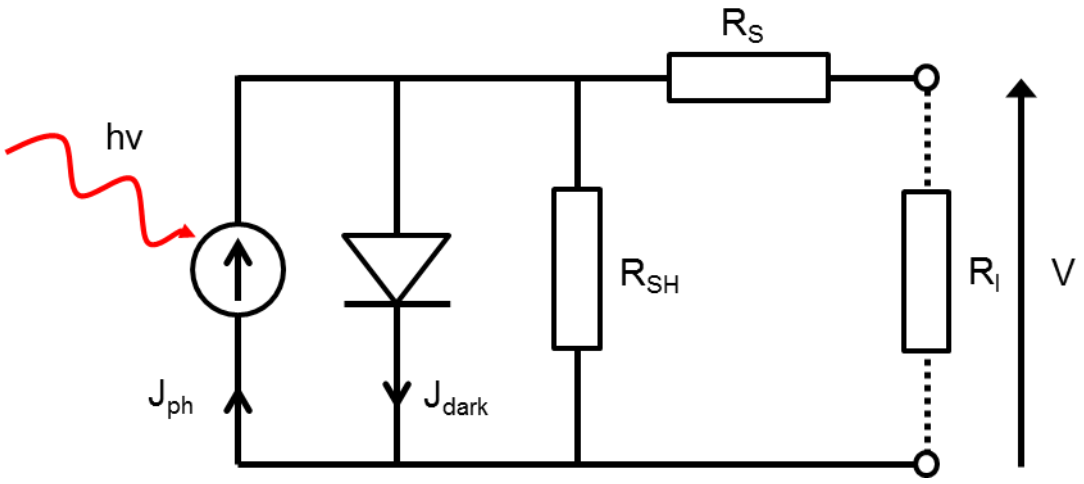

Figure 2.15: Schematic of an equivalence circuit for an OPV device with resistances.

Many parameters can be extracted from the *J-V* plots in the dark and under illumination for characterisation of the OPV devices, i.e. J_{SC}, V_{OC}, *FF*, *PCE*, R_{SH} and R_S.

J_{SC} is the short circuit current density at zero applied bias V=0, the equivalent of R_l = 0 Ω. This occurs at the intercept of the curve with the *J* axis in Figure 2.14b. It is a measure of the collected photocurrent at the electrodes and is therefore dependent upon the absorption, exciton dissociation and the charge transport in the device (section 1.6).

V_{OC} is the open circuit voltage and is the voltage generated across the device when the load resistance is infinitely high, $R_l = \infty$. Photogenerated charges cannot flow out of the device and build up creating an electric field. The V_{OC} is experimentally

obtained by applying a bias to reduce the internal electric field until no current is flowing through the device. It occurs at the intersect of the curve with the *V* axis in Figure 2.14b.

P_{MP} is the maximum power output and is the maximum product of the current and voltage of the device. From a plot of *P-V*, as shown by the red line in Figure 2.14b, P_{MP} can be obtained which is the product of J_M and V_M.

FF is the fill factor and is an ideality factor for the shape of the J-V curve. It is determined by the ratio of the operational maximum power output to the theoretical maximum power output obtained by the product of V_{OC} and J_{SC} as shown in Equation 2.10. The ratio can be expressed graphically as the ratio of the blue and orange square in Figure 2.14b. It is affected by the parasitic resistances within the device.

$$FF = \frac{V_{MP}J_{MP}}{V_{OC}J_{SC}} \qquad \text{(Equation. 2.10)}$$

The power conversion efficiency (*PCE*) is a ratio of the maximum power output (P_{MP}) to incident radiation power intensity (P_{INC}) as shown in Equation 2.11.

$$\eta = PCE = \frac{P_{MP}}{P_{INC}} = \frac{V_{OC}J_{SC}FF}{P_{INC}} \qquad \text{(Equation. 2.11)}$$

Parasitic Resistances such as R_S and R_{SH} reduce the *FF* of a device leading to a loss in *PCE* (Figure 2.16). The series resistance (R_S) results from the resistivity of the materials and the contacts in the device. In an ideal case, R_S = 0 Ω and an increase leads to a decreased slope in positive bias and loss in *FF* (Figure 2.16a). The shunt resistance (R_{SH}) is affected by current leakage through pinholes and defects in the

device. In an ideal case, $R_{SH} = \infty$ and a decrease leads to an increased slope at negative bias and again a loss in *FF* (Figure 2.16b).

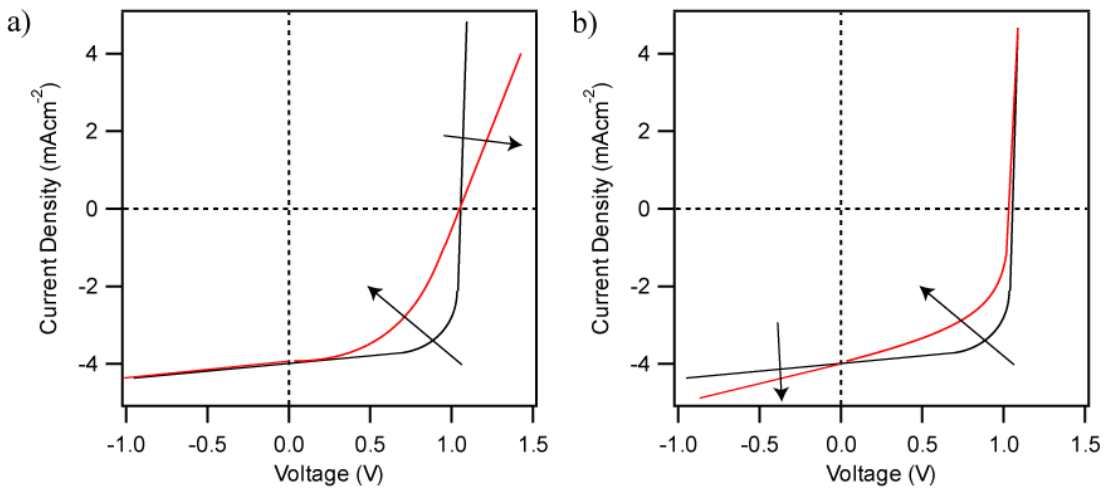

Figure 2.16: Effect of parasitic resistance on the *J-V* curve shape a) R_S, with arrow indicating an increase in R_S. b) R_{SH}, arrow increases a decrease in R_{SH}.

In this thesis the *J-V* measurements were recorded by a Keithley 2400 source-meter controlled by a computer running custom LabView software. All devices were tested in a custom built, sealed sample holder under a nitrogen atmosphere.

2.2.4.3 External Quantum Efficiency (EQE)

To gain further understanding of the photocurrent contribution from the individual components of the PV device, an *EQE* measurement can be undertaken to determine the spectral response. The contribution of an active component should follow the electronic absorption of the material, as absorption of a photon leads to exciton generation. In a multi-component system, where the materials absorb in different

regions of the spectrum, the spectral response will elucidate the contribution of each material to the device photocurrent. EQE (also denoted incident photon conversion efficiency IPCE) is the ratio of the J_{SC} (λ) to the incident photon density flux N (λ) at a particular wavelength as shown in Equation 2.12. q is the elementary charge.

$$EQE\ (\lambda) = \frac{J_{SC}\ (\lambda)}{qN(\lambda)} \qquad \text{(Equation. 2.12)}$$

Experimentally the *EQE* is determined by comparison of the measured device J_{SC}, with a reference silicon photodiode with a known *EQE* using the following Equation 2.13.

$$\frac{J_{SC}(\lambda)(device)}{J_{SC}\ (\lambda)\ (ref)} = \frac{EQE\ (\lambda)(device)}{EQE\ (\lambda)(ref)} \qquad \text{(Equation. 2.13)}$$

The J_{SC} of the reference diode and the device are both measured using the set-up displayed in Figure 2.17. The illumination comes from a Sciencetech solar simulatior with a Xe arc lamp white light source which passes through a PTI monochromator, a mechanical chopper and is focused onto the Si reference diode (818UV, Newport)/ OPV device. The current is measured using a current-voltage amplifier (Femto DHPCA-100) and a lock-in amplifier (Stanford Research SR 830 DSP) connected to a PC. The J_{SC} of the Si photodiode is measured over a determined wavelength range followed by the J_{SC} of the OPV device over the same wavelength range. The ratio of the diode and OPV device J_{SC} is then multiplied by the *EQE* of the reference diode to obtain the *EQE* of the OPV device.

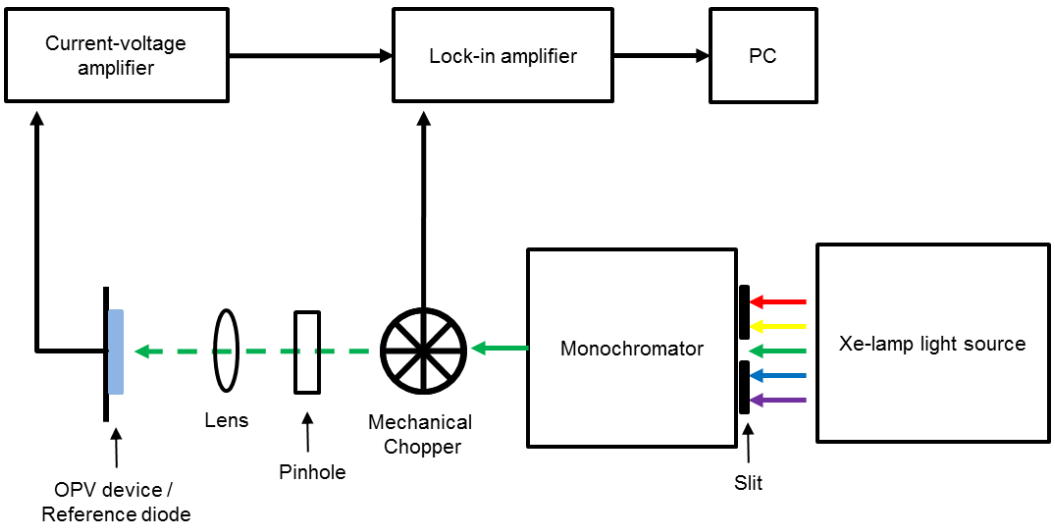

Figure 2.17: Schematic of the *EQE* set up.

Chapter 3 Modification of the photoactive layer in tandem OPV devices

In this chapter the properties of a broad absorption small molecule tandem OPV device based upon SubPc and ClAlPc are investigated. The properties and optimisation of the Ag recombination layer are studied by comparing the Ag layer thickness and deposition conditions on the performance of the tandem OPV device. Subsequently, the influence of the photoactive layer composition on performance in a ClAlPc:C_{60} BHJ OPV device is investigated with implementation in a BHJ tandem OPV device. Finally, the effect of adding a structural templating layer under the ClAlPc to improve charge collection in single and tandem OPV devices is shown.

3.1 Tandem OPV system

The recent progress made in small molecule tandem OPV structures was summarised in section 1.4. To develop an efficient tandem OPV device, the photoactive material choice is important to ensure broad spectrum absorption. The material system investigated here is based upon a green absorbing SubPc and a red-NIR absorbing ClAlPc as the two donor materials. The spectroscopic properties of these materials along with C_{60} are shown in Figure 3.1. The absorption of the photoactive materials extends over most of the visible spectrum with the SubPc peaking at 590 nm and the ClAlPc peaking at 730 nm. In combination with the commonly used C_{60} absorbing in the blue region, there is scope to achieve an efficient tandem OPV with this device

system. Using these materials, efficiencies up to 4.1% have been achieved for a PHJ tandem device.[93]

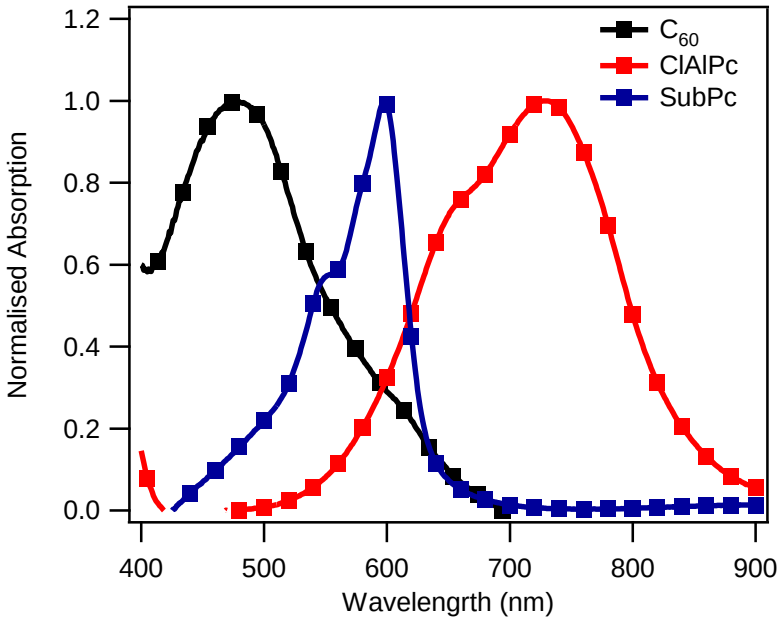

Figure 3.1: Absorption properties of ClAlPc, SubPc and C_{60}. Thin film absorption measured using 20 nm layers on quartz glass.

3.2 Recombination Layer Optimisation

Section 1.7.1 outlined the importance of an efficient recombination layer in tandem OPV devices. Metallic nanoclusters have been used as recombination sites in multiple tandem OPV devices.[18,125] In these devices there is a trade-off between conductivity and parasitic absorption in the selection of layer thickness, affecting both the V_{OC} and the J_{SC} of the device.[19] The optimisation of an Ag recombination layer for a small molecule tandem OPV device is shown here.

3.2.1 Morphology of the Ag layer

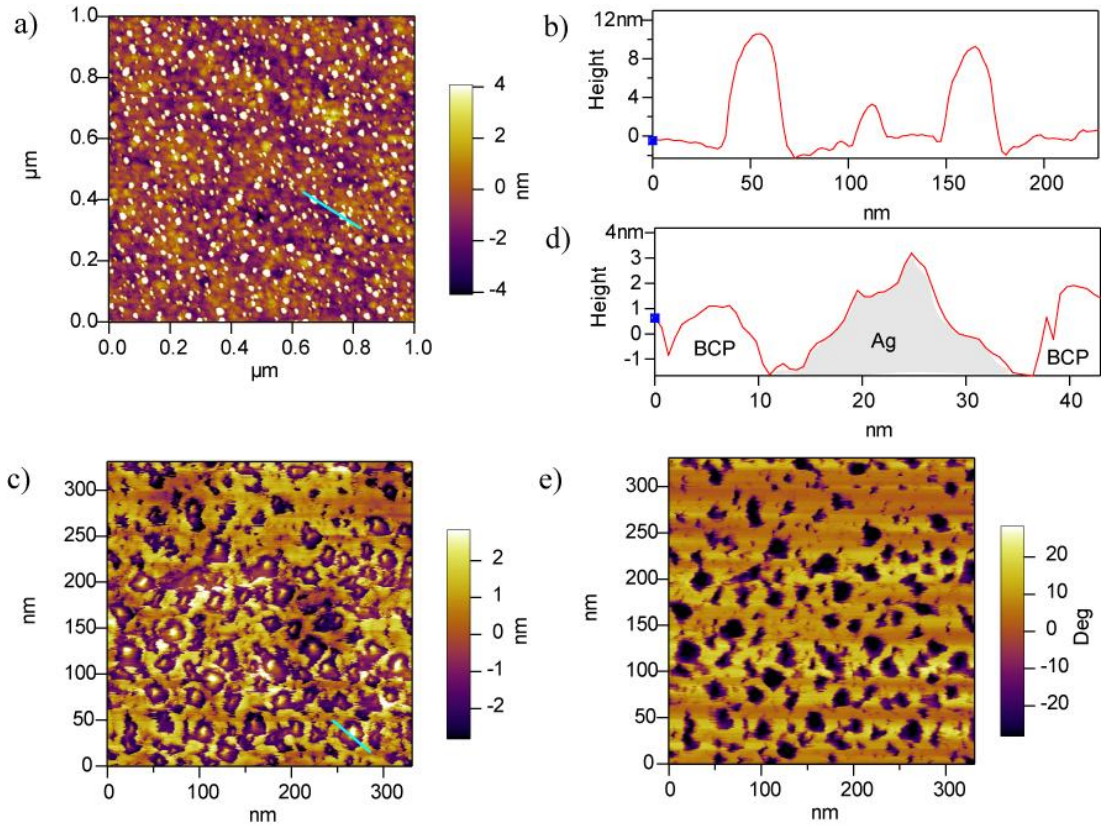

Figure 3.2: AFM images of a) Ag on ITO, b) Cross section of Ag on ITO (Blue line on image a), c) Ag on BCP, d) Cross section of Ag on BCP (Blue line on image c), e) AFM phase image of Ag on BCP.

An AFM tapping mode image of a 0.5 nm layer of Ag evaporated on ITO is presented in Figure 3.2a. A continuous layer is not formed at this thickness; instead spontaneous agglomeration of the Ag forms an irregular array of nanoclusters.[19] These have features up to 30 nm in diameter and 10 nm high (Figure 3.2b), much larger than the thickness assumed from the QCM. In the tandem device structure, the metallic recombination layer is usually located after an exciton blocking layer such as BCP,[125] therefore the morphology of 0.5 nm Ag on 8 nm of BCP was also investigated (Figure 3.2c). Just like the Ag on ITO, agglomeration of the Ag is

favoured over forming a continuous layer. Similar feature sizes are created with diameters up to 30 nm although the height of the nanocluster is lower than the ITO / Ag sample. Figure 3.2c suggests that the Ag nanocluster has embedded into the BCP layer with a reduction in layer height ~4 nm around the cluster peak from the bulk layer (Figure 3.2d). The phase image for the AFM scan is displayed in Figure 3.2e. Areas of a different phase are shown where the Ag nanoclusters are proposed to have formed which don't alter with layer height. This suggests that it is not a formation from the BCP layer but in fact the embedded Ag nanoclusters. Hot metal deposition on to BCP layers inducing states has been proposed as a mechanism for enabling charge transport in the wide band gap exciton blocking layer,[118] and these results suggest that the embedding of Ag within the BCP layer could provide charge transport paths through the layer to act as an effective recombination site.

3.2.2 Optical Properties of Ag layer

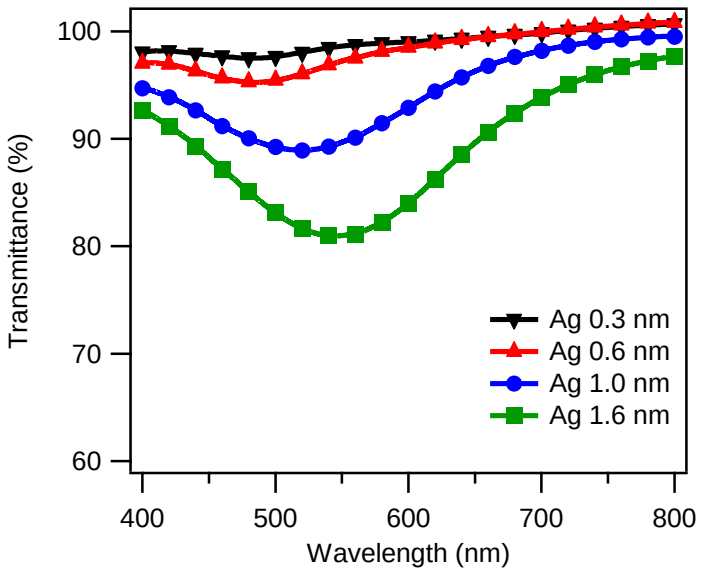

Figure 3.3: Transmittance spectra of Ag on quartz.

Figure 3.3 displays the transmittance spectra of a range of Ag layers deposited onto quartz glass. For thin Ag layers of 0.3 nm, there is little transmittance loss across the visible spectrum. Increasing the thickness up to 1.6 nm, there is an emergence of a peak at 550 nm from the resonant frequency of the plasmonic modes of the Ag particles.[126] The peak position overlaps with the main absorption peak of SubPc (Figure 3.1), and incorporation of a 1.6 nm Ag layer as a recombination layer could result in up to a 20 % parasitic loss in the absorption of SubPc at 550 nm. Previous devices in literature have therefore use sub nanometre thicknesses of metal recombination layers.[19,125]

3.2.3 Tandem OPV Device Properties

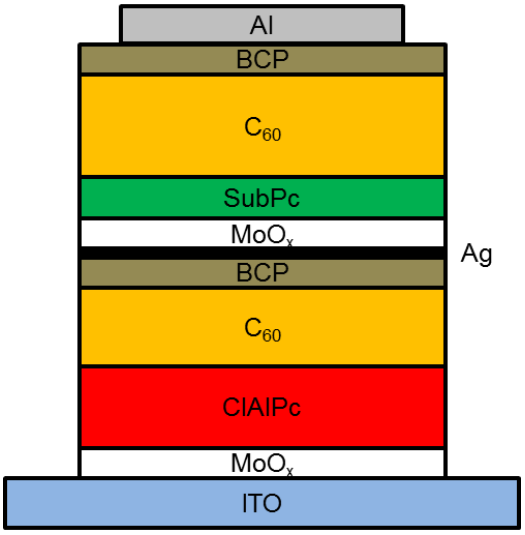

Figure 3.4: A schematic of PHJ tandem OPV device structure used for Ag recombination layer optimisation.

The measurement of tandem device performance for varied Ag thicknesses and deposition rates were used to optimise the Ag recombination layer for a small molecule tandem organic solar cell. Figure 3.4 presents the tandem device schematic used in this investigation ITO / MoO_x (5 nm) / ClAlPc (17 nm) / C_{60} (20 nm) / BCP (8 nm) / Ag / MoO_x (5 nm) / SubPc (10 nm) / C_{60} (32.5 nm) / BCP (8 nm) / Al. The green absorbing SubPc sub-cell (Figure 3.1) is placed closest to the reflective Al cathode with the red absorbing ClAlPc furthest away towards the ITO. As shown in section 1.7.3, the optical field in a thin film OPV device is dominated by the optical interference caused by the reflecting Al electrode which is wavelength dependent. The sub-cells need to be positioned in an optical field maximum to produce high photocurrents and for current balancing. Figure 3.5 shows the simulated absorptance of the tandem OPV device (Figure 3.4) for two sub-cell configurations using the transfer matrix model (Section 2.2.3.3). The absorptance of the device with the SubPc sub-cell closest to the Al cathode is shown in Figure 3.5a. A high absorptance is shown in each of the SubPc and ClAlPc photoactive layers around their specific absorption wavelengths from Figure 3.1. The reverse sub-cell configuration is shown in Figure 3.5b and a lower absorptance is seen throughout the device. Both of the photoactive layers, SubPc and ClAlPc have lower absorptances in this configuration compared to the structure in Figure 3.5a. and will lead to a lower J_{SC} and poorer *PCE* in the tandem OPV device. To maximise the absorptance in the photoactive layers the device configuration show in Figure 3.5a is used as each of the photoactive layers is aligned with the optical field and photocurrents are balanced.

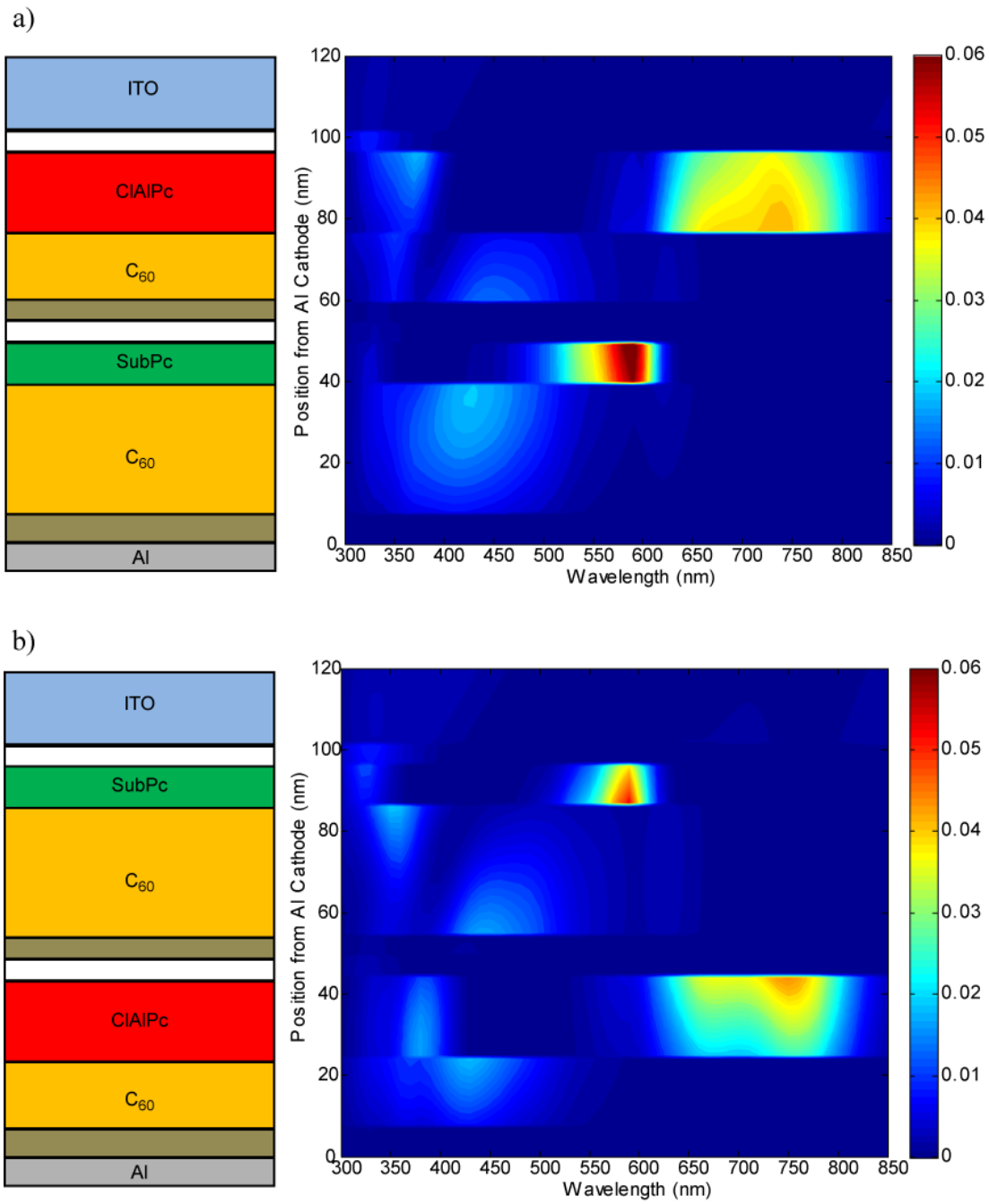

Figure 3.5: Optical simulation plots of the absorptance through the tandem OPV device for two configurations as shown next to the y-axis scale.

3.2.3.1 Ag recombination layer Thickness

The effect of the thickness of the Ag recombination layer on the device performance was investigated by fabricating a series of devices (Figure 3.4) with the range of thicknesses used in section 3.2.2. The *J-V* plots of the devices are shown in Figure 3.6 with performance parameters summarised in Table 3.1.

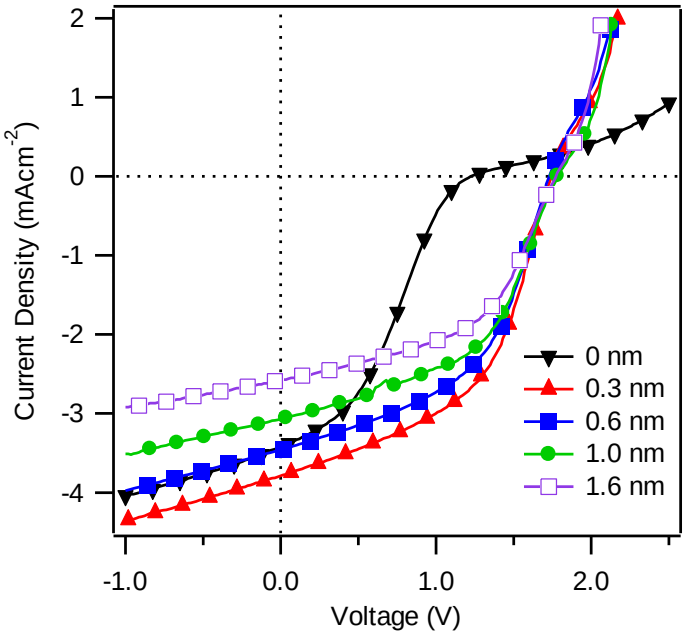

Figure 3.6: *J-V* plots for the PHJ tandem OPV devices with Ag recombination layer thicknesses 0 – 1.6 nm.

Ag thickness (nm)	J_{SC} (mA cm^{-2})	V_{OC} (V)	*FF*	*PCE* (%)
0	3.45	1.18	0.33	1.41
0.3	3.84	1.75	0.50	3.43
0.6	3.42	1.76	0.49	3.07
1.0	3.16	1.78	0.49	2.87
1.6	2.57	1.77	0.51	2.40

Table 3.1: Device parameters of PHJ tandem OPV device with Ag recombination layer thickness 0-1.6 nm.

A reduction in J_{SC} is shown with increased Ag thickness from 3.84 mA cm^{-2} to 2.76 mA cm^{-2} for a 0.3 nm and a 1.6 nm layer respectively. This decrease is caused by the increased absorption of the Ag layer shown in Figure 3.3 reducing the incident light reaching the back SubPc / C_{60} sub-cell. The V_{OC} remains high and consistent across the range of Ag thicknesses close to the voltage summation of the two sub-cells, ClAlPc (0.8 V)[92] and SubPc (1.1 V).[97] A device without the recombination layer has been included with the V_{OC} only reaching 1.18 V and a low *FF* of 0.33, showing the necessity for efficient recombination sites for electrons and holes from different sub-cells.[19] The *FF* is not affected by Ag thickness indicating efficient charge recombination even for very thin non discrete layers. The *PCE* follows a similar trend to J_{SC} with the most efficient device of 3.43 % resulting from a Ag thickness of 0.3 nm. A reduction in *PCE* is seen with thicker Ag layers.

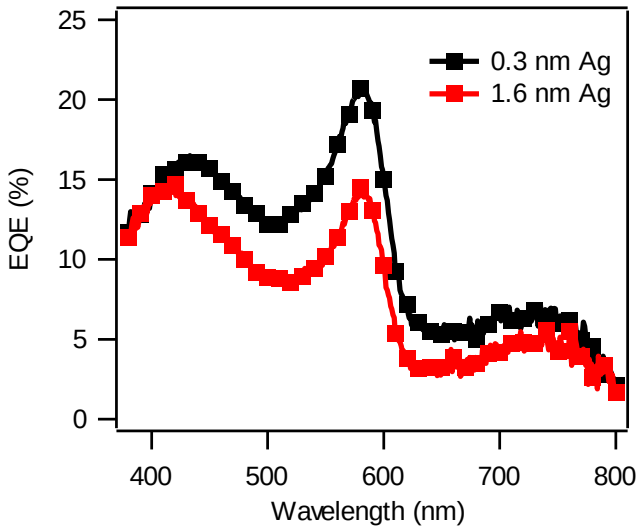

Figure 3.7: EQE spectra of the PHJ tandem OPV devices with an Ag recombination layer of 0.3 and 1.6 nm.

Figure 3.7 presents the monochromatic EQE spectra of the tandem devices for two Ag thicknesses; 0.3 nm and 1.6 nm. Under monochromatic bias the tandem OPV device is still able to produce a photocurrent when only one sub-cell is absorbing due to the non-absorbing sub-cell passing a small photocurrent as it is working under reverse bias.[24] A reduction in the EQE spectra is seen from 400 – 750 nm with increased Ag layer thickness to 1.6 nm. The decrease in EQE is due to the parasitic absorption of the thicker Ag layer as shown in Figure 3.3 across the wavelength region. This result supports the *J-V* data, with the thickness of the Ag layer employed being a trade-off between conductivity and parasitic absorption.

3.2.3.2 Deposition Rate

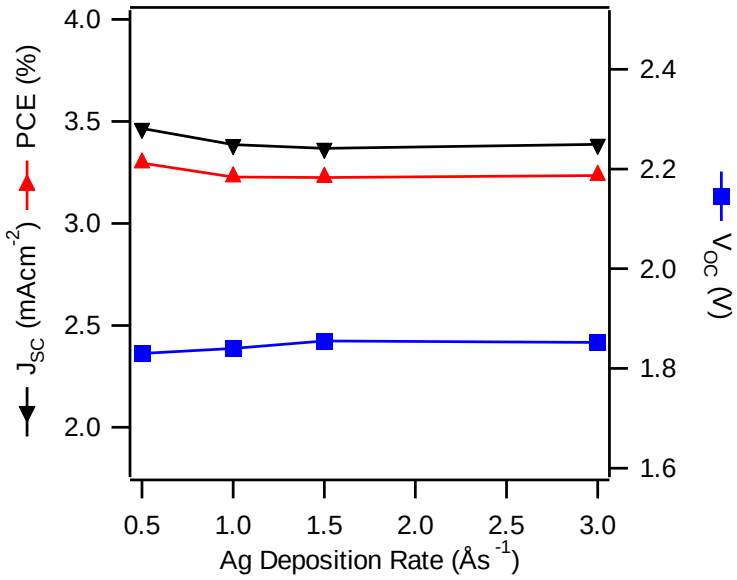

Figure 3.8: Device characteristics for tandem cell (Figure 3.4) with varied deposition rates of the Ag recombination layer.

Figure 3.8 presents the device parameters for a series of PHJ tandem devices (Figure 3.4) with a 0.3 nm Ag recombination layer deposited at different evaporation rates. The device performance; V_{OC}, J_{SC} and *PCE* show little variation across the deposition rates from 0.5 Ås^{-1} to 3 Ås^{-1}. Due to the thin Ag layer used, a slower deposition rate is preferred which will allow for more accurate layer reproduction as the 0.3 nm layer deposited at 0.5 Ås^{-1} requires the shutter to be open for just 6 s. Further increases in deposition rate will introduce inaccuracies from the lag time of shutter opening/closing, e.g. 1 s extra at 3 Ås^{-1} would double the layer thickness, increasing the layer absorbance (Figure 3.3). All further tandem devices will use the 0.3 nm Ag recombination layer deposited at 0.5 Ås^{-1}.

3.3 Bulk-heterojunction OPV devices

3.3.1 ClAlPc : C_{60} BHJ device

PHJ cells, such as those introduced in section 3.2.3, display moderate efficiencies, but increasing the photoactive layer thickness for improved light harvesting is limited by the short exciton diffusion lengths of many organic semiconductors.[127] To overcome this problem, co-deposition of the donor and acceptor layers to form a BHJ can be used to increase the surface area of the D/A heterojunction.[128] This reduces the distance excitons have to travel to reach a heterojunction, increasing the probability for exciton dissociation and removing the diffusion length limit on photoactive layer thickness. The most efficient BHJ D:A composition ratio varies depending upon the system studied with some showing preference for donor rich[129] or acceptor rich[130,131] mixtures. In this section, co-deposition of varying compositions ClAlPc and C_{60} will be investigated for their influence on device performance.

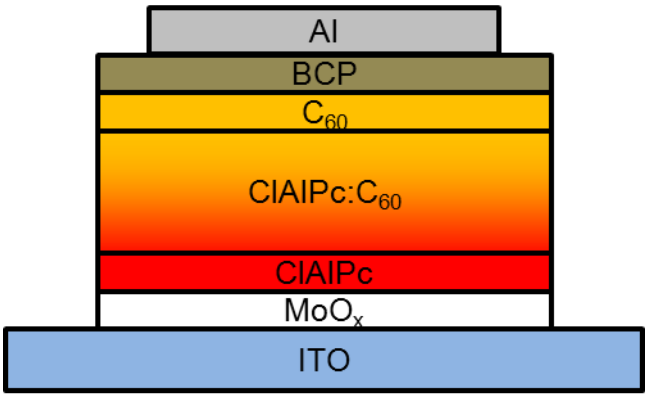

Figure 3.9: A schematic of a BHJ ClAlPc:C_{60} device.

Figure 3.9 displays the device structure of a ClAlPc:C_{60} based single BHJ solar cell. It has the general structure ITO/ MoOx (5 nm) / ClAlPc (10 nm) / ClAlPc:C_{60} x:y (20 nm) / C_{60} (10 nm) / BPC (8 nm) / Al. The BHJ composition (x:y) has been varied from donor rich (3:1), equal (1:1) to acceptor rich (1:3) weight ratio by varying the deposition rate of ClAlPc and C_{60} from 0.75 $Ås^{-1}$ to 0.25 $Ås^{-1}$. J-V curves for the three devices D:A = 3:1, 1:1 and 1:3 are shown in Figure 3.10 with the device characteristics summarised in Table 3.2. The photocurrent is enhanced from 2.61 mA cm^{-2} to 3.57 mA cm^{-2} from the donor rich (3:1) BHJ to the acceptor rich (1:3) BHJ respectively. Preference for a fullerene rich BHJ has been shown for many systems.[130,131] The V_{OC} displays a slight increase with C_{60} content from 0.77 V to 0.82 V with the *FF* having a maximum of 0.48 for the 1:1 BHJ ratio suggesting optimised charge collection efficiency at this point. The *PCE* of the devices improves from 0.92 % to 1.38 % on going from donor rich (3:1) to acceptor rich (1:3) devices.

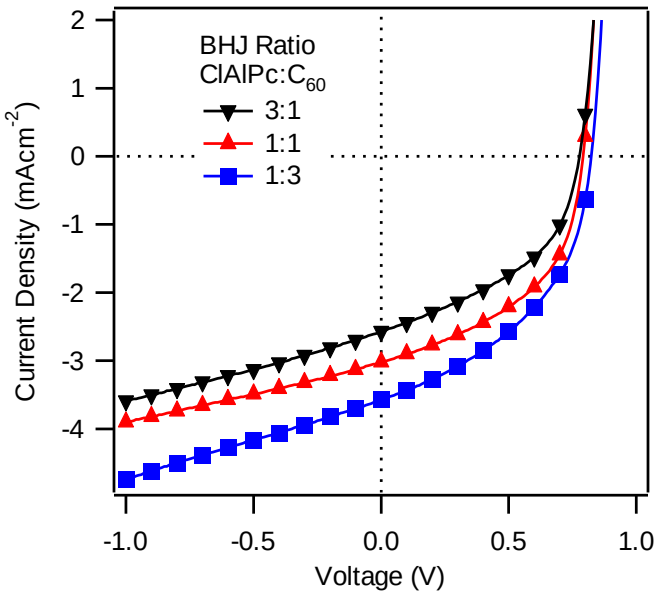

Figure 3.10: *J-V* plots for the ClAlPc:C_{60} BHJ single junction devices of varying D:A compositions.

BHJ Ratio (ClAlPc:C_{60})	J_{SC} (mA cm^{-2})	V_{OC} (V)	*FF*	*PCE* (%)
3:1	2.61	0.77	0.43	0.92
1:1	3.02	0.79	0.48	1.18
1:3	3.57	0.82	0.45	1.38

Table 3.2: Device characteristics for the ClAlPc:C_{60} BHJ devices measured under simulated AM 1.5 illumination at 1 sun.

The *EQE* spectra for the devices are presented in Figure 3.11 and a variation is seen with BHJ composition. A small change is seen in the ClAlPc contribution with varying BHJ composition with the donor rich (3:1) composition peaking at 21 % at 740 nm. The BHJ layers containing a lower ratio of ClAlPc have small contributions although the acceptor rich BHJ (1:3) has a higher peak at 740 nm than the (1:1) BHJ. The main change in the *EQE* spectra is from 400-500 nm resulting from the C_{60} contribution. With increased C_{60} composition the peak at 450 nm increases from 10.3 % to 13.4 % to 20.9 % for the 3:1, 1:1 and 1:3 BHJ compositions respectively. To investigate the varying increase of the ClAlPc and the C_{60} contributions further, optical simulations (Section 2.2.3.3) were carried out for the devices to calculate the absorptance of the different BHJ layers.

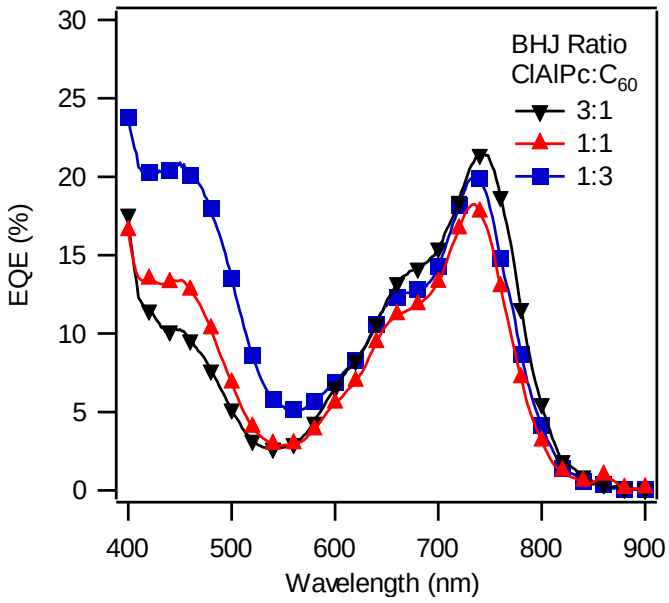

Figure 3.11: *EQE* spectra for the BHJ ClAlPc:C_{60} single devices with varied BHJ D:A compositions 3:1 , 1:1 , 1:3.

Figure 3.12 shows the spectral absorptance calculated from the optical simulation for the three BHJ devices (Figure 3.9). The absorptance of the ClAlPc (600 – 800 nm) varies with the ratio of ClAlPc in the BHJ layer and increasing the ClAlPc content from 25 % to 75 % results in a 20 % gain in absorptance at 750 nm. The C_{60} absorptance (400 – 500 nm) shows a similar trend with it increasing with the C_{60} content from the (3:1) to the (1:3) BHJ layer, with an 80 % improvement. The variation in the absorptance of each photoactive layer with BHJ ratio is due to the optical field within the BHJ layer. At this distance from the Al cathode the optical field is maximised for low wavelengths and the variation with C_{60} content shows the biggest improvement. This larger increase in the absorptance of C_{60} compared with the ClAlPc is the reason for the large gain in the C_{60} EQE shown in Figure 3.11.

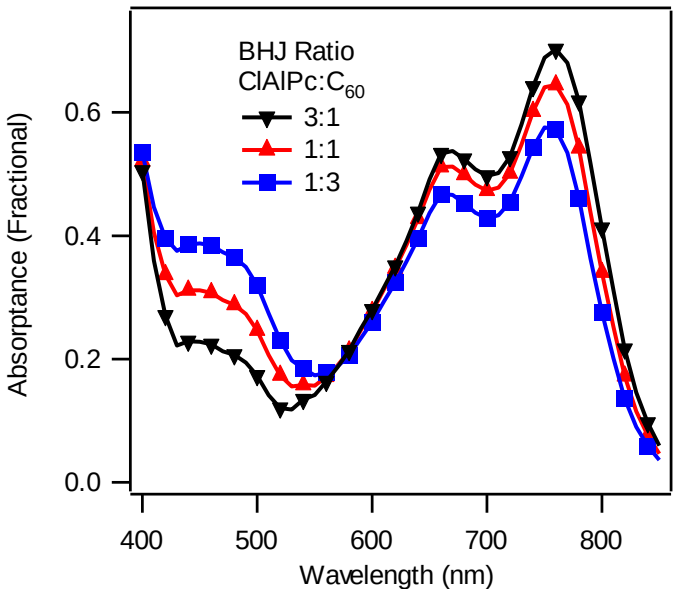

Figure 3.12: Calculated absorptance spectra for the BHJ ClAlPc:C_{60} single devices with varied BHJ D:A compositions 3:1 , 1:1 , 1:3.

3.3.2 BHJ tandem OPV device

To increase the efficiency of the PHJ tandem cell shown in section 3.2, the BHJ concept has been implemented into the sub-cell device structure to enhance the photocurrent. In the tandem device structure, the ClAlPc:C_{60} sub-cell is placed further from the Al cathode in a region that is aligned with the 650 -800 nm optical field (Figure 3.5). Although it may seem preferential to have a high ClAlPc content BHJ composition, photocurrents balancing is important in tandem devices, and sub-cells must be chosen to match the photocurrents produced. A 1:1 BHJ composition is chosen for the ClAlPc:C_{60} sub-cell as this will provide an adequate photocurrent increase over the PHJ device and the highest *FF* of the BHJ compositions, as seen in Table 3.2. SubPc:C_{60} BHJ devices have been widely investigated in the literature

with the most efficient devices obtained from a SubPc:C_{60} 1:4 ratio, due to the improved crystallinity and hole mobility of SubPc.[132] The structure for the tandem device is displayed in Figure 3.13 and is constructed from ITO / MoO_x (5 nm) / ClAlPc (10 nm) / ClAlPc:C_{60} 1:1 (20 nm) / C_{60} (10 nm) / BCP (8 nm) / Ag / MoO_x (5 nm) / SubPc (10 nm) / SubPc:C_{60} 1:4 (30nm) / C_{60} (10 nm) / BCP (8 nm) / Al. The overall device thickness is similar to the PHJ device (Figure 3.4).

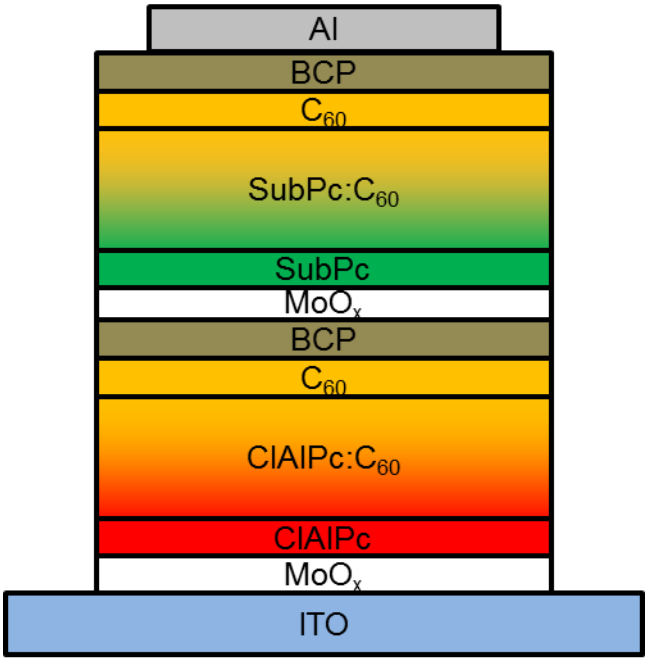

Figure 3.13: Device schematic for the ClAlPc:C_{60} SubPc:C60 BHJ tandem cell.

The *J-V* plots for the PHJ (Section 3.2.3) with a 0.3 nm Ag layer and the BHJ tandem device are displayed in Figure 3.14 with the device characteristics summarised in Table 3.3. As expected for the BHJ device, a higher photocurrent of 4.54 mA cm^{-2} was achieved compared to the 3.84 mA cm^{-2} generated in the PHJ device. This increase is due to the enhancement of the exciton dissociation in each sub-cell from the BHJ structure. The V_{OC} of the BHJ device is slightly improved but a drop in *FF* is seen from 0.50 to 0.46 from the PHJ to BHJ due to the less efficient

charge collection paths in the co-deposited layer.[98] The *PCE* of the BHJ reaches 3.81 % which is an 11 % improvement over the PHJ device.

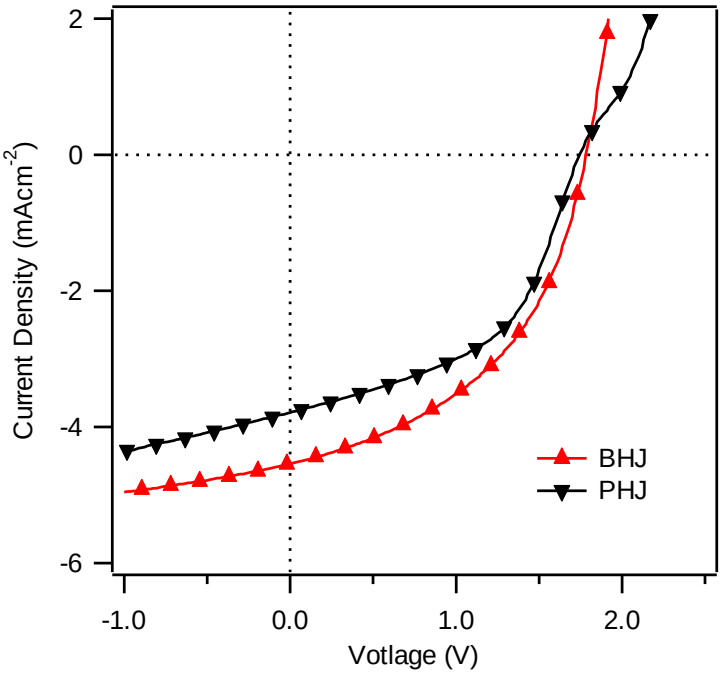

Figure 3.14: J-V plots of the PHJ (Figure 3.5) and BHJ tandem devices.

Tandem Device	J_{SC} (mA cm^{-2})	V_{OC} (V)	*FF*	*PCE* (%)
PHJ	3.84	1.75	0.50	3.43
BHJ	4.54	1.78	0.46	3.81

Table 3.3: Device characteristics of the PHJ and BHJ tandem cell measured under simulated AM1.5 illumination.

3.4 PTCDA as a structural template

The co-deposition of phthalocyanine donor molecules with C_{60} to form a BHJ has been widely studied as a method for improved photocurrent and to overcome the limitations of short exciton diffusion lengths in organic semiconductors.[128] An alternative method to overcome these problems involved utilising a structural template to preferentially align the phthalocyanine molecules.[133] The charge transport in molecular films is anisotropic, with efficiency related to the π stacking of molecules. In planar phthalocyanines, the stacking direction on typical non interacting substrates occurs parallel to the substrate, perpendicular to the preferred charge transport paths necessary for organic solar cells.[54] PTCDA has been shown to act as an effective templating layer, with strong π- π interactions with the phthalocyanines altering the orientation of CuPc and ClAlPc and improving J_{SC} in both device systems.[90,133] In this section, PTCDA was used as a templating layer for both single ClAlPc:C_{60} and tandem devices.

3.4.1 Optical Properties

Figure 3.15 shows the absorption spectra for a 20 nm ClAlPc film and a 1 nm PTCDA / 20 nm ClAlPc bilayer. The ClAlPc film has a maxima around 730 nm with a shoulder at 670 nm, similar to published data.[86] The peak at 670 nm matches with the solution spectra and suggests the presence of monomeric species. The spectrum for the PTCDA / ClAlPc bilayer displays a red shift in the Q band peak for ClAlPc. This higher peak arises from aggregation and ordering of the ClAlPc molecules in

the film.[134] X-ray diffraction has shown an increased crystallintity of ClAlPc when grown onto PTCDA, with molecules adopting a lying down orientation 14° from the plane with closer ClAlPc-ClAlPc distances.[90] This was shown to be beneficial in OPV devices.

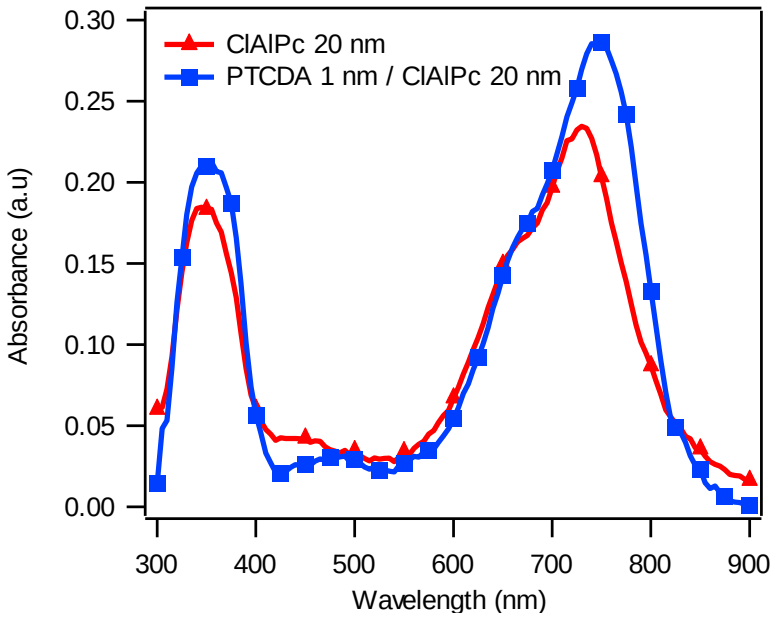

Figure 3.15: Absorption of ClAlPc (20 nm) and PTCDA (1 nm) / ClAlPc (20 nm). All sample were grown onto ITO coated glass

3.4.2 AFM

The morphology of a heterojunction interface can alter the performance of a PHJ device. A larger surface area at the interface may allow for increased exciton dissociation compared to a flat PHJ.[135] Figure 3.16 presents AFM images of two films a) 20 nm ClAlPc and b) 1 nm PTCDA / 20 nm ClAlPc. The ClAlPc film comprises of small crystallites with a RMS roughness of 3.03 nm. The bilayer PTCDA / ClAlPc (Figure 3.16b) has a similar grain size with a RMS roughness of

2.75 nm. With a similar roughness obtained for the templated films, no improvement should be seen from the alteration of the heterojunction interface in OPV devices.

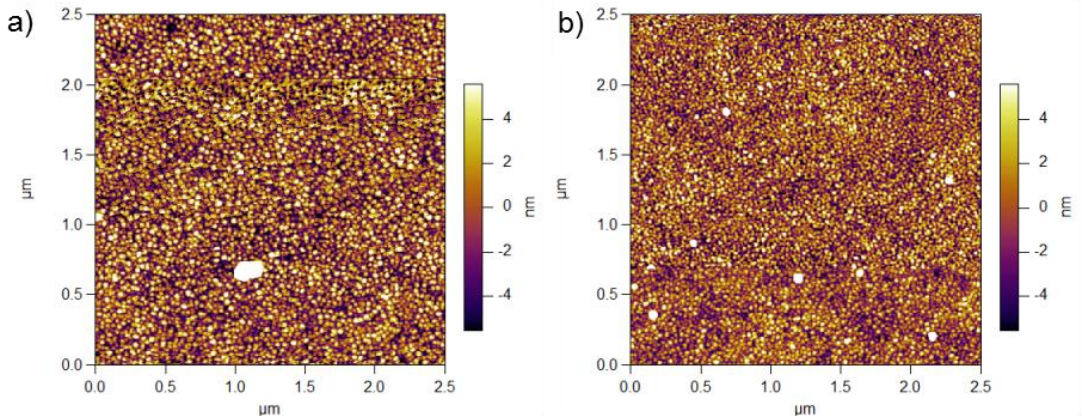

Figure 3.16: AFM images of a) 20 nm ClAlPc b) 1 nm PTCDA / 20 nm ClAlPc. All layers were grown on ITO coated glass.

3.4.3 Device data

To investigate the effect of adding a PTCDA template layer on device performance, both single and tandem devices were constructed. Device schematics are shown in Figure 3.17 with the same device structure as Figure 3.4 with an added 1 nm PTCDA layer. The reference devices exhibited lower J_{SC} and higher V_{OC} than before as the ClAlPc used for these devices was from a different supplier to the previous section. Figure 3.18 presents the *J-V* characteristics for the single and tandem devices, with and without PTCDA and the device parameters are summarised in Table 3.4

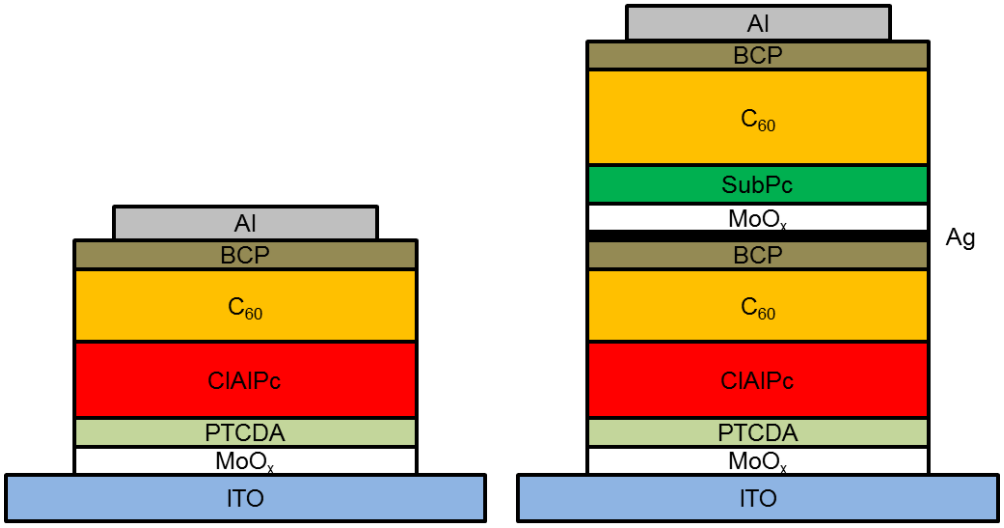

Figure 3.17: Device Schematics of a) PTCDA template ClAlPc / C_{60} single OPV devive and b) PTCDA template ClAlPc / C_{60} / SubPc /C_{60} tandem OPV device.

The single ClAlPc / C_{60} devices show an improvement in J_{SC} from 2.09 mA cm^{-2} to 2.59 mA cm^{-2} on insertion of a PTCDA template layer similar to previous reports.[90] A small increase in V_{OC} is seen and a large improvement in *FF* from 0.49 to 0.57. This can be attributed to the preferential alignment of the ClAlPc with PTCDA, improving charge transport and charge collection. In the tandem device, there is little improvement in the J_{SC} due to the limitation of current matching with the SubPc sub-cell. With a large improvement in photocurrent in one sub-cell, overall J_{SC} is limited by the lowest photocurrent of the two. The main improvements in the PTCDA template tandem device are in V_{OC} and *FF*. The *FF* increases from 0.51 to 0.55 due to the improved charge transport in the ClAlPc film. The overall *PCE* of the tandem device improves from 3.21 % to 3.59 % on addition of a PTCDA template layer.

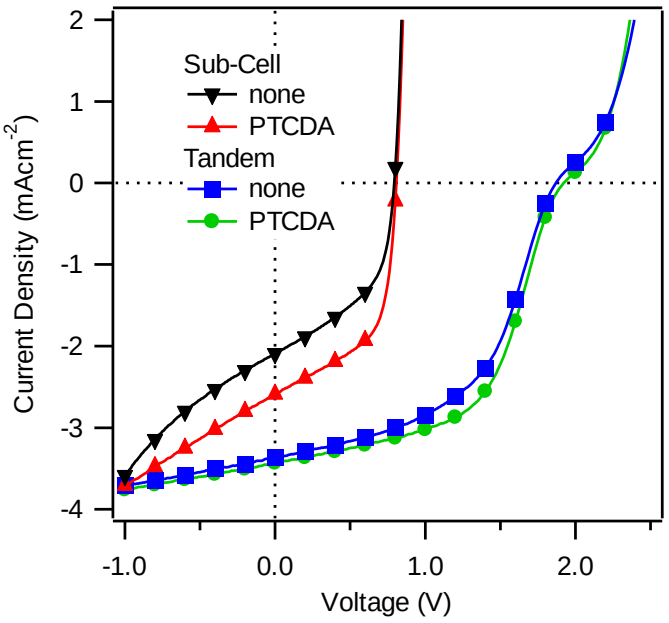

Figure 3.18: *J-V* plots of the single ClAlPc/C_{60} devices, with and without a PTCDA layer and the tandem devices, with and without a PTCDA layer.

Device Structure	J_{SC} (mA cm^{-2})	V_{OC} (V)	*FF*	*PCE* (%)
Single	2.09	0.79	0.49	0.81
Single PTCDA	2.59	0.81	0.57	1.19
Tandem	3.37	1.87	0.51	3.21
Tandem PTCDA	3.43	1.92	0.55	3.59

Table 3.4: Device parameters of the single ClAlPc/C_{60} devices, with and without a PTCDA layer and the tandem devices, with and without a PTCDA layer.

3.5 Summary

This chapter focused on the optimisation of the Ag recombination layer in a tandem OPV device and on the modification of the sub-cell photoactive layers. Thin Ag layers were shown to form nanoclusters up to 30 nm in diameter which embedded in the underneath BCP layer. The influence of the Ag layer thickness was investigated in a ClAlPc / C_{60} // SubPc / C_{60} based tandem OPV device with a 0.3 nm giving the optimum performance of 3.43 %. The parasitic absorbance of thicker Ag layers was shown to hinder the light absorption in the photoactive layers.

Two routes for modification of the photoactive layers were investigated: co-deposition of the donor and acceptor and using PTCDA as a structural template for ClAlPc. Different BHJ ratios in a ClAlPc:C_{60} device were shown to affect the photocurrent with a preference for C_{60} rich compositions shown in the J-V curves and the EQE. The simulated absorptance of the photoactive layers indicated that the preference for C_{60} was due to the BHJ layer being positioned in the optical field that is suited to the 450 nm absorption of C_{60}. Using BHJ sub-cells in a ClAlPc:C_{60}//SubPc:C_{60} tandem device a photocurrent increase from 3.84 mA cm^{-2} to 4.54 mA cm^{-2} was observed leading to an improved performance of 3.81 % compared to the PHJ device of 3.43 %.

The absorption of the PTCDA templated ClAlPc showed a red shift in the Q band suggesting increased ordering of the film. In both single ClAlPc / C_{60} devices and ClAlPc / C_{60}//SubPc / C_{60} PTCDA templating lead to an improvement in the *FF* due to the improved charge transport in the ClAlPc layer.

Chapter 4 α-NPD as an Optical Spacer Layer

In this chapter, the concept of an optical spacer in small molecule tandem OPV devices will be investigated as a method for optimising cell design and performance. α-NPD has been chosen as a candidate for the optical spacer layer and its optical, electrical and morphological properties have been investigated. Co-deposition of α-NPD with MoO_x has been used to improve its mobility.

Subsequently, the performance of this material system as a transport layer in single OPV devices is discussed with demonstration of the optical spacing effect in single BHJ ClAlPc devices and its effect on the device performance.

Finally, the use of an α-NPD optical spacer layer in a series of tandem organic solar cells is investigated. By using optical simulations, *EQE* and *TAE* measurements the function of optical spacing on tandem device optimisation has been found.

4.1 α-NPD

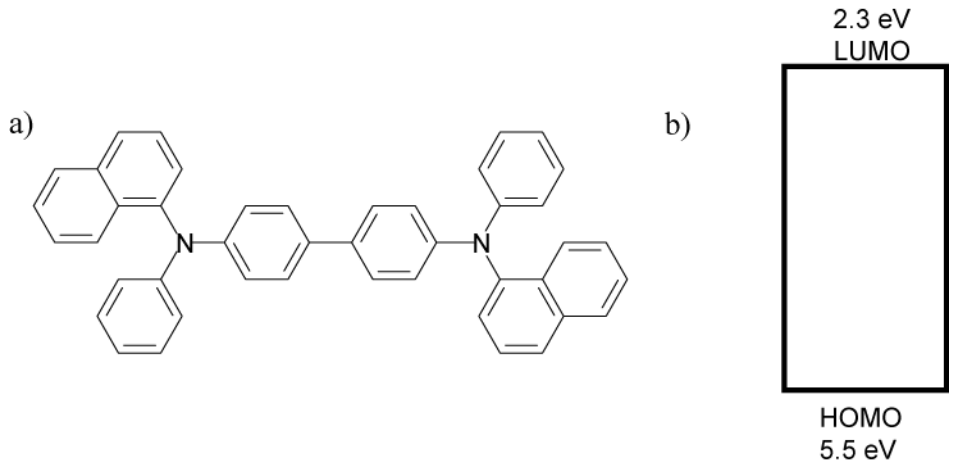

Figure 4.1: a) Molecular structure of α-NPD b) Energy level diagram of α-NPD.

As shown in section 2.1.3.2 α-NPD has been widely used as a hole transporting layer in OLEDs. The HOMO energy level at 5.5 eV[115] can allow for alignment with many phthalocyanine systems such as SubPc with its HOMO level of 5.6 eV.[97] This alignment makes α-NPD a good candidate as a hole transport material for OPV devices based on SubPc.

4.1.1 Optical and electrical Properties of α-NPD

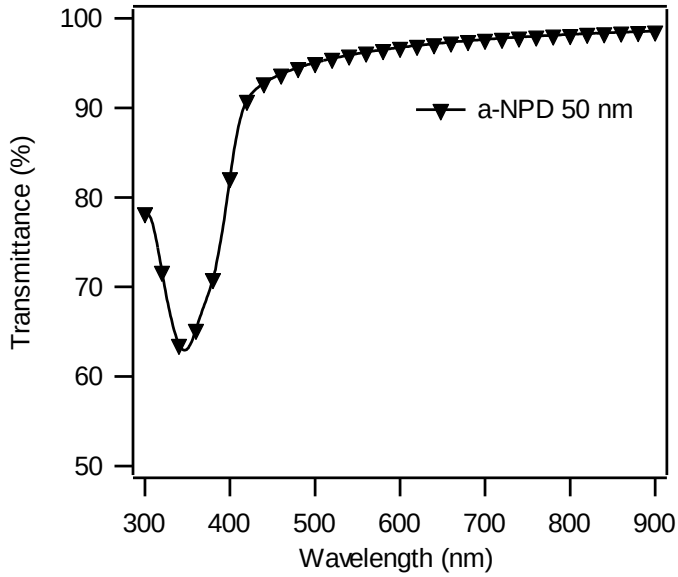

Figure 4.2: Transmittance spectrum of a 50 nm α-NPD film deposited onto quartz.

Figure 4.2 shows the transmittance spectrum of a 50 nm α-NPD film on quartz. Due to its large band gap of ~3 eV (Figure 4.1), most of the absorption occurs in the UV region below 400 nm. Above this and across the visible region, the layer has over a 90 % transmittance which makes it a good candidate for an optical spacer layer in OPV devices. Ideally, transport layers should be transparent to avoid parasitic absorption from the non-photoactive layers in a OPV device. Due to the wide band gap, the hole mobility of the intrinsic α-NPD layer is low. Figure 4.3 displays the J-V characteristics of an α-NPD film with MoO_x interlayers as ohmic contacts to ensure hole-only transport (ITO / MoO_x (5nm) / α-NPD (100 nm) / MoO_x (5 nm) / Al). Charge injection in the device is dominated by hole injection from the ITO with electron injection from the Al blocked by a large injection barrier to the MoO_x. Fitting this plot to the space charge limited current equation,[136] a hole mobility of 2 $\times$ 10^{-4} cm^2 V^{-1} s^{-1} is found. This mobility is low compared to some organic

semiconductors[107] and use in thick optical spacer layers may result in resistance losses.

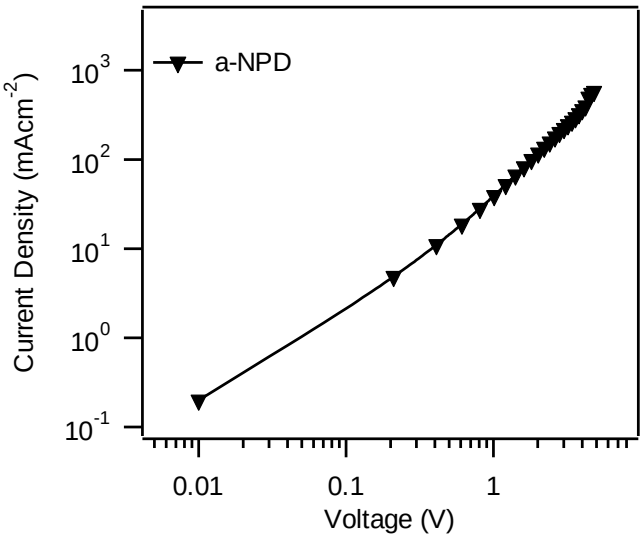

Figure 4.3: *J-V* plot of hole only device ITO / MoO_x (5nm) / α-NPD (100 nm) / MoO_x (5 nm) / Al.

4.2 α-NPD co-deposited with MoO_x

To improve the mobility of organic semiconductors, molecular doping has been demonstrated as a method for increasing charge transport.[137] Electron transfer from a host organic semiconductor matrix to a dopant molecule or vice versa has been shown to provide free charges in the material which help facilitate hole or electron transfer.[138] P-doping in these systems requires molecules with high electron affinities to accept an electron from the host. These materials can be very expensive, e.g. 2,3,5,6-tetrafluoro-7,7,8,8-tetracyanoquinodimethane (F4-TCNQ) which sells for £2870/g.[139] A cheaper solution, MoO_x, has been shown as an effective p-dopant material for α-NPD[115] with the mobility improved by an order of magnitude. In this section, the concentration of MoO_x will be studied as a method to improve the mobility of α-NPD.

4.2.1 Optical properties of α-NPD with different MoO_x concentrations

Figure 4.4 presents the absorption spectra of a range of α-NPD and MoO_x combinations. Figure 4.4a displays the absorption of 50 nm co-deposited layers on quartz with a range of MoO_x concentrations. As before, the pristine α-NPD layer has low absorption in the visible region above 400 nm and a large absorbance in the UV. On addition of MoO_x into the film, there is an emergence of a peak at 500 nm which increases with MoO_x concentration. This peak is due to the radical cation created by electron transfer from the HOMO of the α-NPD to the deep lying acceptor states in MoO_x indicating a doping of the α-NPD layer by the MoO_x.[140] This state also increases absorption in the IR region of the spectrum. The peak in the UV region at ~350 nm decreases with increased MoO_x concentration from the reduction of intrinsic α-NPD in the film. Figure 4.4b shows the absorbance of a bilayer of α-NPD and MoO_x along with the co-deposited layer. This was investigated to show that the peak present was an electrical and not an optical effect of the two materials. As can be seen in Figure 4.4b, the peak at 500 nm is not present in the bilayer film compared to the co-deposited layer. This again indicates that the peak is produced by a charge transfer state of the α-NPD and MoO_x which occurs more efficiently in the co-deposited layer than the bilayer.

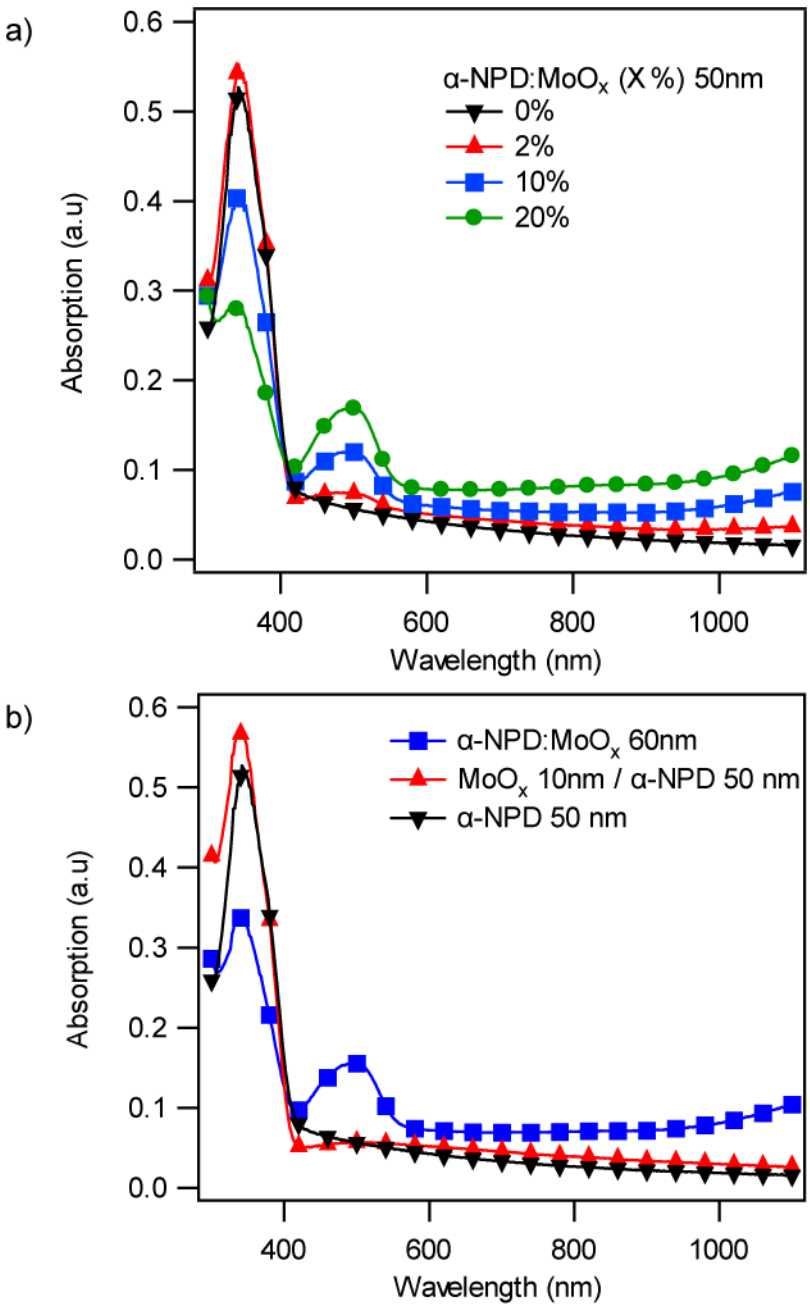

Figure 4.4: Absorption spectra of a) 50 nm codeposited α-NPD:MoO_x films with varied concentration. b) 50 nm α-NPD, 10 nm MoO_x / 50 nm α-NPD and α-NPD:MoO_x 60 nm. All layers were grown on quartz glass.

4.2.2 Charge transport in α-NPD:MoO_x layers

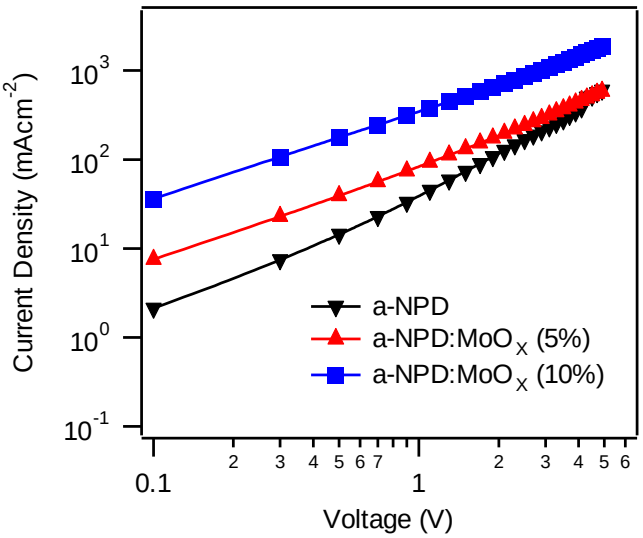

Figure 4.5: *J-V* plots of hole only α-NPD with varied MoO_x concentration 5% and 10 %.

The *J-V* characteristics for hole only devices consisting of α-NPD and α-NPD:MoO_x layers are displayed in Figure 4.5. The α-NPD device is the same structure as discussed in Figure 4.3. With a forward bias applied, the current density passed through the device increases on the addition of MoO_x. This also improves with increased MoO_x concentration, with a large jump in current density from 5 to 10% MoO_x, where ohmic conduction is seen as the slope is near unity ($J \propto V$). The improvement in electrical conductivity is due to the charge transfer from the α-NPD to the MoO_x, generating free carriers for hole transport.[115]

4.2.3 Kelvin Probe

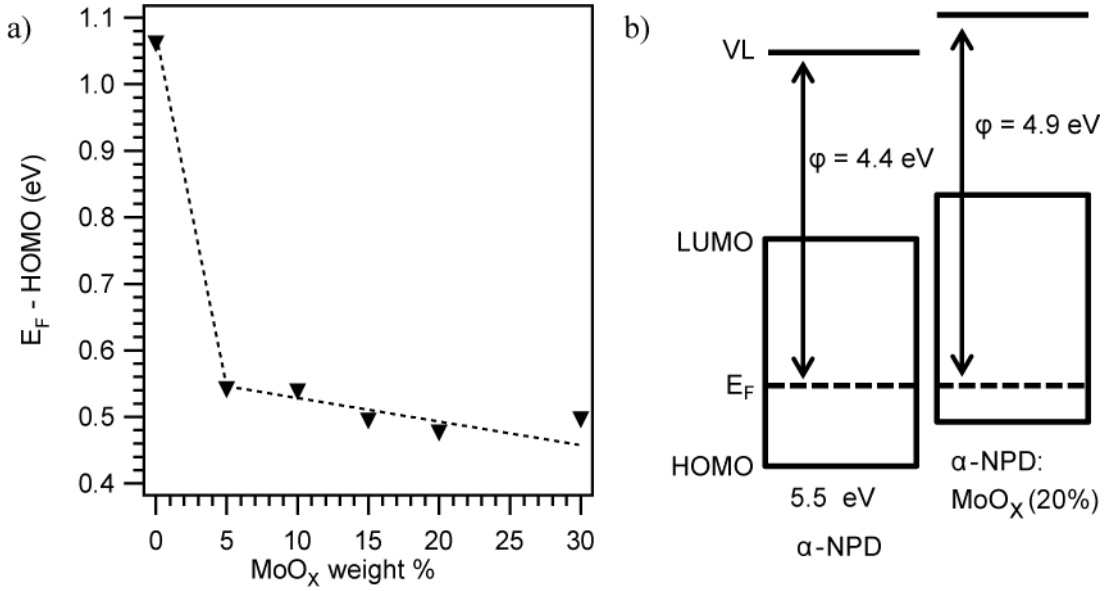

Figure 4.6: a) Energy difference between E_F and HOMO vs MoO_x concentration. Workfunction measured using KP and HOMO level taken from litereature.[115] Dotted line is guide for the eye. b) Schematic of energy level diagrams showing E_F shift towards α-NPD HOMO.

To investigate the extent of electrical doping further in the α-NPD:MoO_x layers surface work function measurements of α-NPD films with increasing concentration of MoO_x were measured using a Kelvin probe. The energy difference between the Fermi level (E_F) and the HOMO of the films is shown in Figure 4.6a for different MoO_x concentrations. There is a large shift in E_F towards the HOMO on the addition of a small concentration of MoO_x to 0.54 eV above the HOMO, corresponding to an increase in carrier concentration as the α-NPD layer turns from intrinsic to electrically doped.[115] Further increases in MoO_x concentration result in a small shift in E_F which is finally pinned at around 0.5 eV above the HOMO beyond 20% MoO_x. Figure 4.6b displays a schematic of the E_F shifts in the α-NPD layer with the addition of small concentrations of MoO_x. The reduction in hole injection barrier from the ITO can clearly be seen in the α-NPD:MoO_x (20%) layer.

4.2.4 Layer topography

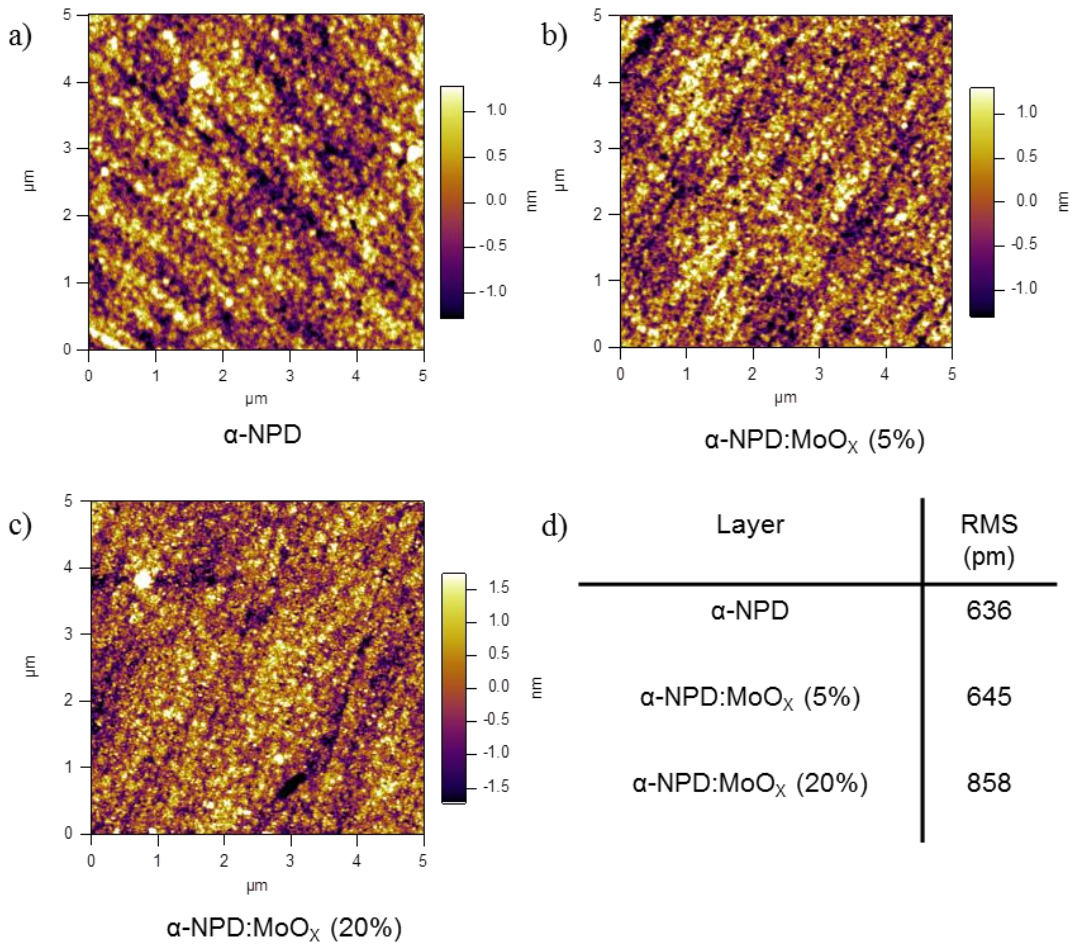

Layer	RMS (pm)
α-NPD	636
α-NPD:MoO$_X$ (5%)	645
α-NPD:MoO$_X$ (20%)	858

Figure 4.7: AFM topography images of 20 nm layers of α-NPD on ITO with varied concentration of MoO_x. a) α-NPD, b) α-NPD:MoO_x (5%), c) α-NPD:MoO_x (20%), d) A table of the RMS roughness of each of the layers

The effect of MoO_x concentration on the surface topography of the α-NPD layer is displayed in the AFM images in Figure 4.7. The surface topography is important as a large roughness will alter subsequent layer deposition. The topography of α-NPD and the two co-deposited layers have similar features, with small grains seen across the surface. All the layers show very low RMS roughness with the neat α-NPD layer

having an RMS of 636 pm. With the addition of MoO_x into the layer, there is a slight increase in roughness to 645 pm and 858 pm for 5% and 10% concentrations respectively. The similarity in layer morphology for the α-NPD and the α-NPD:MoO_x layer follows from reports in the literature where the MoO_x consists of small nanoclusters of < 1.5 nm in diameter, dispersed inside the α-NPD host.[141] The co-deposited layer should therefore have no adverse effects upon subsequent layer morphology.

4.3 Device Data

4.3.1 α-NPD as a hole transport layer with MoO_x interlayers

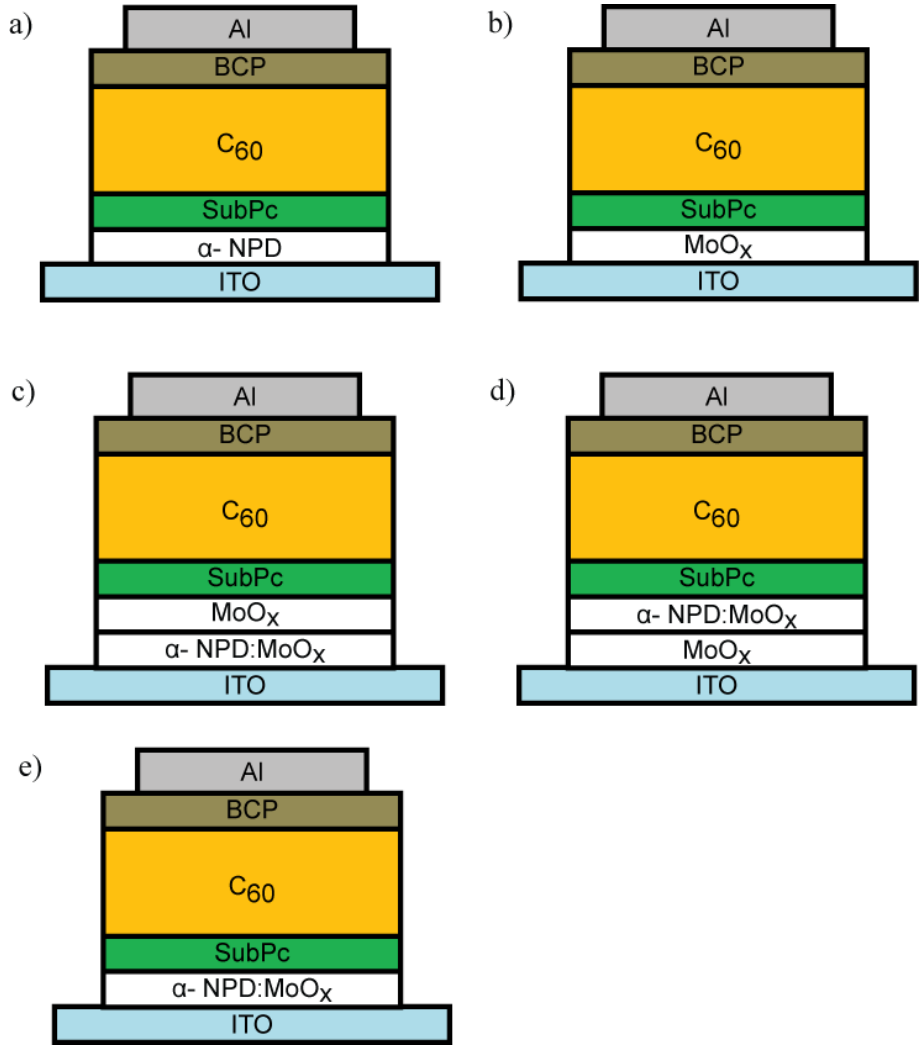

Figure 4.8: Structure of a SubPc / C_{60} single junction OPV device with different HTLs; **a)** α-NPD **b)** MoO_x **c)** α-NPD:MoO_x (10%) / MoO_x **d)** MoO_x / α-NPD:MoO_x (10%) **e)** α-NPD:MoO_x (10%).

For α-NPD to act as an efficient optical spacer layer in tandem OPV devices it must show effective hole transporting characteristics and form a suitable interface with the donor layer for hole extraction. A comparative set of devices consisting of α-NPD and α-NPD:MoO_x (10%) HTLs were investigated as shown in Figure 4.8. These

consisted of the general device structure ITO / Hole Transport Layer (HTL) / SubPc (10 nm) / C_{60} (32.5 nm) / BCP (8 nm) / Al where the HTL had multiple configurations. A HTL of MoO_x (5 nm) was used as the reference device for this system.[60] The intrinsic α-NPD HTL has the structure; α-NPD (50 nm) while three structures were studied for the co-deposited α-NPD:MoO_x (10%) HTLs; α-NPD:MoO_x (10%) (50 nm), MoO_x (5 nm) / α-NPD:MoO_x (10%) (50 nm) and α-NPD:MoO_x (10%) (50 nm) / MoO_x (5 nm).

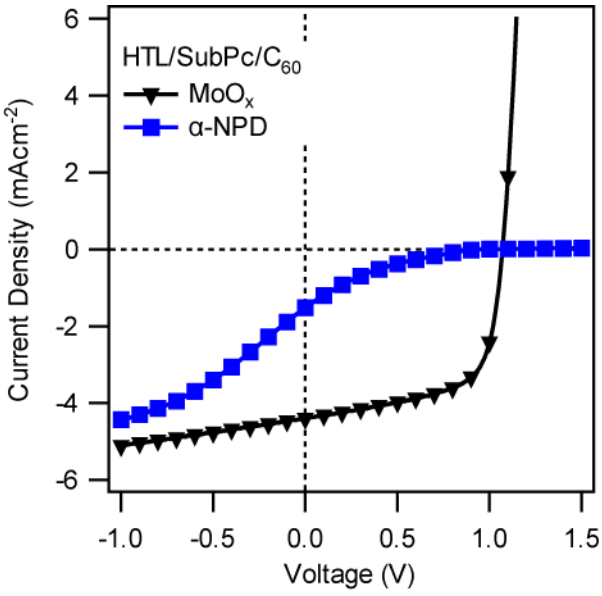

Figure 4.9: *J-V* plots for the SubPc / C_{60} device with two HTLs; MoO_x and α-NPD.

The *J-V* characteristics of the plain α-NPD and the MoO_x HTLs (Figure 4.8a,b) are displayed in Figure 4.9. The reference MoO_x HTL device shows a J_{SC} of 4.39 mA cm^{-2} and a *FF* of 0.64. The V_{OC} is consistent with previous SubPc/C_{60} reports of 1.07 V [60] and gave an overall power conversion efficiency of 2.98 %. The α-NPD HTL device showed a dramatically reduced performance with a J_{SC} of 1.51 mA cm^{-2} and a *FF* of 0.14 while the V_{OC} remained close to 1 V. The drop in efficiency is due to the high series resistance of the 50 nm α-NPD layer as shown by the low current density

in forward bias in Figure 4.9. This makes the layer problematic for use as an optical spacer as the charge transport needs to be unaffected by the layer thickness.

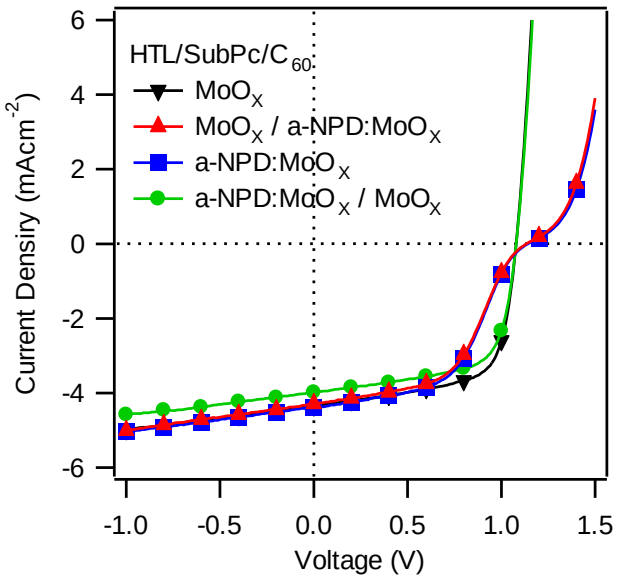

Figure 4.10: *J-V* plots for the SubPc / C_{60} device with four HTLs; α-NPD:MoOx (10%) , MoOx / α-NPD:MoOx (10%) , α-NPD:MoOx (10%) / MoOx and MoOx.

Figure 4.10 presents *J-V* characteristics for the α-NPD:MoO_x based HTLs. The reference MoO_x HTL device shows a similar performance to the device presented in Figure 4.9 achieving a V_{OC} of 1.08 V, a *FF* of 0.66 and a *PCE* of 3.21 %. The device with α-NPD:MoO_x as a HTL shows a much improved performance over plain α-NPD (Figure 4.9) with a similar J_{SC} to the MoO_x HTL device (4.40 mA cm^{-2}) and a V_{OC} of 1.13 V. The *FF* is reduced heavily to 0.55 due to the S-shaped curve present in the power quadrant. From previous reports by Tress et al. this suggests that α-NPD:MoO_x forms a barrier for hole extraction reducing the efficiency of this process.[142] Two other devices were fabricated which included a MoO_x layer either on the ITO or the SubPc side of the α-NPD:MoO_x. The *J-V* plots show two distinct characteristics. The device with the additional MoO_x layer at the ITO side of the α-

NPD:MoO_x has a similar shape to that of the device with no additional layer, with a V_{OC} of 1.13 V and a *FF* of 0.51, suggesting that this S-shape curve is due to the poor interface between α-NPD:MoO_x and SubPc and not the ITO. Placing the additional layer next to the SubPc showed similar performance for hole extraction as the plain MoO_x layer, with a V_{OC} of 1.08 V and a *FF* of 0.66. The J_{SC} of the device was slightly reduced due to the parasitic absorption of the α-NPD:MoO_x but overall shows the possibility for the use of α-NPD:MoO_x as a hole transport layer.

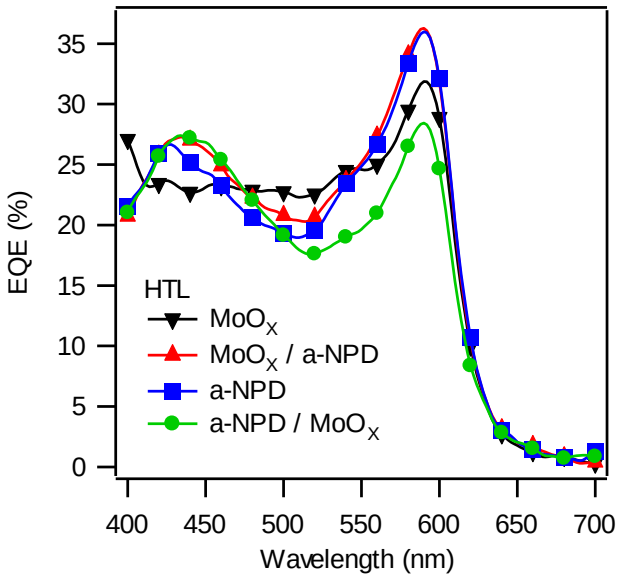

Figure 4.11: EQE spectra for the SubPc / C_{60} device with four HTL; α-NPD:MoO_x (10%) , MoO_x / α-NPD:MoO_x (10%) , α-NPD:MoO_x (10%) / MoO_x and MoO_x.

The external quantum efficiencies for the four devices shown in Figure 4.10 are shown in Figure 4.11. All of the devices show an EQE for the SubPc peak at 590 nm above 25%, and most of the variation in J_{SC} of the devices is due to the SubPc contribution at 500-600 nm. Devices that contain α-NPD:MoO_x have a distinctly different shape to the MoO_x HTL device, with a peak at 430 nm and a trough at 350

nm and 500 nm. Transfer matrix simulations of the SubPc/C_{60} absorptance (Figure 4.12) show that this is an optical effect from the parasitic absorption of the 50 nm α-NPD:MoO_x layer.

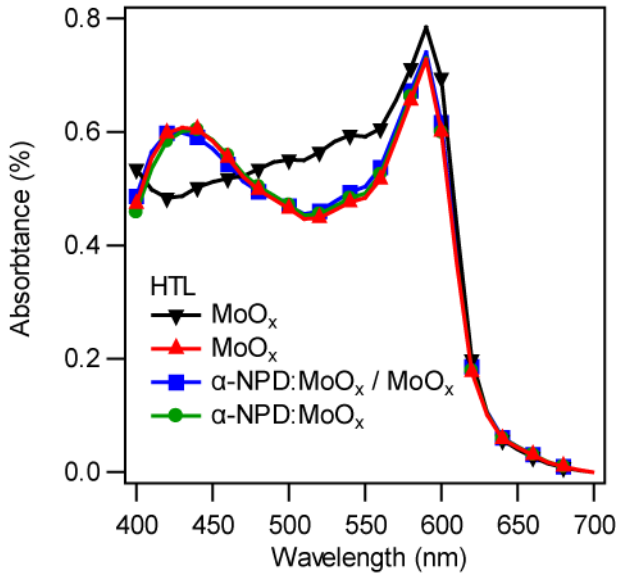

Figure 4.12: Optical simulation of the absorptance of the SubPc/C_{60} layers for the four devices in Figure 4.8b.

4.3.2 Thickness dependence

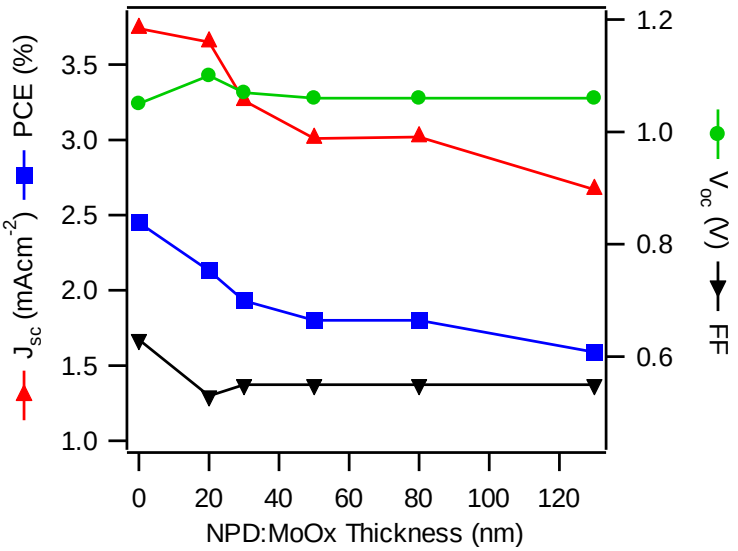

Figure 4.13: Device characteristics for a SubPc / C_{60} heterojunction with varied thickness of an α-NPD:MoO_x HTL (0 – 130 nm).

With the desire to use α-NPD:MoO_x as an optical spacer, the layer must have properties that are independent of thickness up to ~150 nm.[143] A range of devices were fabricated with the structure; ITO / α-NPD:MoO_x (10 %) (d nm) / MoO_x (5 nm) / SubPc (10 nm) / C_{60} (32.5 nm) / BCP (8 nm) / Al with d varying from 0 to 130 nm. The device characteristics are shown in Figure 4.13 with variations in α-NPD:MoO_x thickness. The overall performances are slightly reduced to those shown in section 4.3.1, but they are comparable to each other as they are fabricated with a similar batch of materials. The device with 0 nm α-NPD:MoO_x corresponds to a reference MoO_x HTL device. This device shows a J_{SC} of 3.74 mA cm^{-2} and a *FF* of 0.63. The V_{OC} of 1.05 is typical of a SubPc/C_{60} device. On addition of the α-NPD:MoO_x layers of different thickness, there is a reduction in J_{SC} up to ~30%, although only 20 % at thicknesses up to 80 nm. This is consistent with the parasitic absorption of this layer (section 4.3.1). The V_{OC} and *FF* of the device give an

indication of the thickness independence of this HTL with device operation. There is only a slight reduction in V_{OC} from 1.10 V at 20 nm to 1.06 V at 130 nm and a reasonable *FF* of 0.55 is maintained with 130 nm of α-NPD:MoO_x. These thickness independent hole transporting properties suggest potential for α-NPD:MoO_x as an optical spacer layer in tandem OPV devices.

4.4 Optical spacing effect in single junction devices

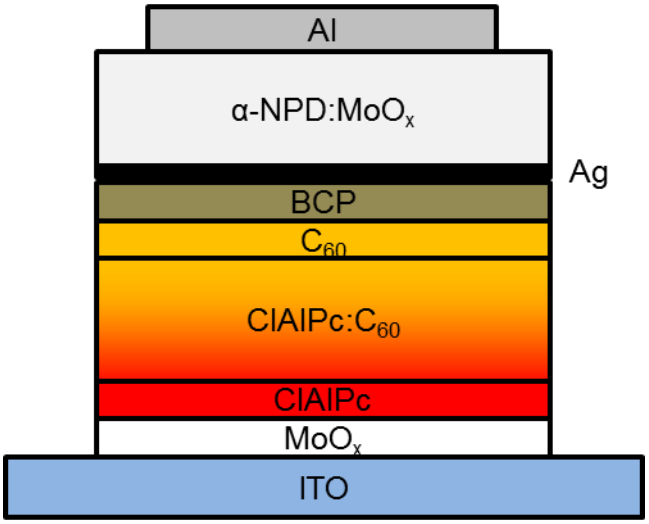

Figure 4.14: Schematic of a ClAlPc:C_{60} BHJ single junction OPV device with an α-NPD:MoO_x optical spacer layer.

To provide an experimental measurement of the optical spacing effect in OPV devices using α-NPD:MoO_x, a simple BHJ single junction device was investigated. This allowed for the optical effects of the active layers to be probed without dealing with the hurdles of current matching in tandem OPV devices. Figure 4.14 shows the device structure used for this investigation; ITO / MoO_x (5 nm) / ClAlPc (10 nm) /

ClAlPc:C_{60} (1:1) (20 nm) / C_{60} (10 nm) / BCP (8 nm) / Ag (0.3 nm) / α-NPD:MoO_x (0-190 nm) / Al. The thin Ag layer acts as a recombination site for electrons in the BCP and holes in the α-NPD:MoO_x (Section 3.2). This simulates the HTL effect of α-NPD:MoO_x in a tandem OPV device. As the device is in operation, the photo-generated electrons that are extracted by the BCP layer are recombined at the Ag nanocluster sites by holes that are injected from the external circuit and travel through the α-NPD:MoO_x layer.

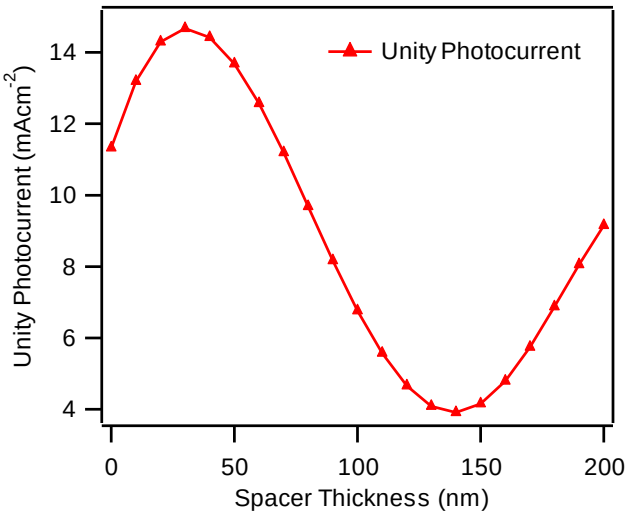

Figure 4.15: Unity photocurrent as a function of spacer thickness for the device shown in Figure 4.14 calculated from a transfer matrix simulation.

Before fabricating the device a transfer matrix model (Section 2.2.3.3) was used to investigate the variation in absorptance within the device layers with spacer thickness. The absorptance of the photoactive layers of ClAlPc / ClAlPc:C_{60} (1:1) / C_{60} has been integrated over the AM1.5 solar spectrum (Figure 2.11b) and a plot of unity photocurrent (the J_{SC} assumed with 100% IQE) versus spacer thickness is displayed in Figure 4.15. The absorptance in the device will be dominated by the interference pattern created by the reflecting Al cathode which acts as a node for a

standing wave interference pattern. Figure 4.15 shows an increase in photocurrent of 30 % to a maximum at 30 nm spacer thickness as the photoactive layer is placed in an optical interference maximum. A further increase in spacer thickness reduces the photocurrent and a minimum is reached at 140 nm with a 65 % reduction in the original photocurrent. At thicknesses beyond 150 nm, the photocurrent starts to recover as the photoactive layers move towards the second interference maximum.

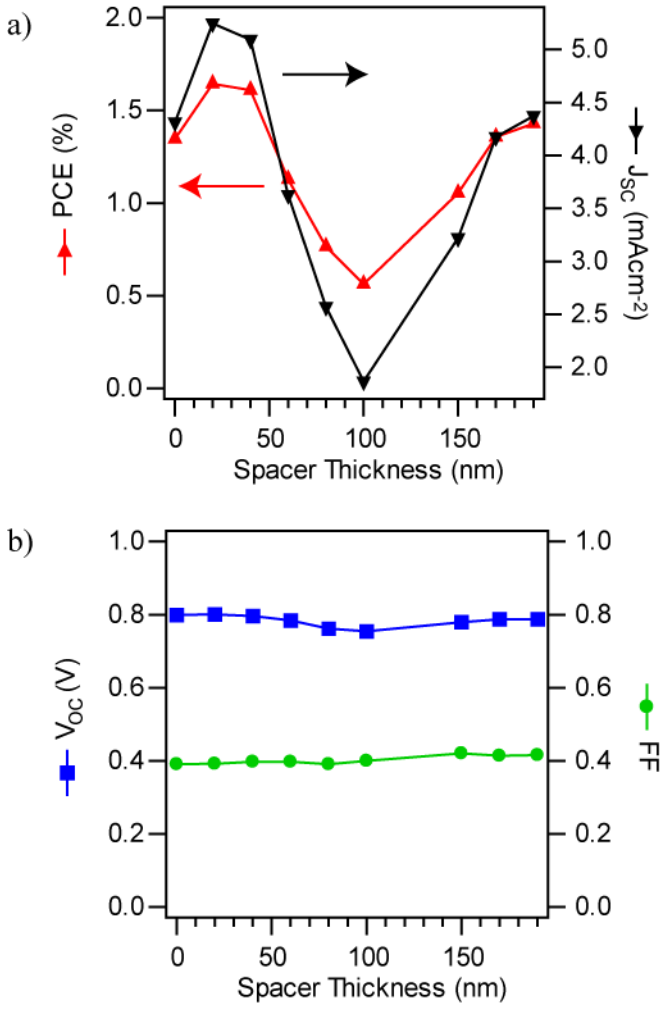

Figure 4.16: Performance characteristics of the ClAlPc / C_{60} BHJ device versus spacer thickness **a)** J_{SC} and *PCE* **b)** V_{OC} and *FF*

The device performance characteristics for the fabricated devices are shown in Figure 4.16. The J_{SC} varies substantially with spacer thickness because of the

interference pattern of the optical field within the active layers (Section 1.5). The device without an optical spacer layer has a J_{SC} of 4.31 mA cm^{-2}. On addition of a 20 nm α-NPD:MoO_x spacer layer this increases to 5.25 mA cm^{-2}. This is the result of moving the active layers into the first optical interference maximum. Increasing the spacer thickness to 100 nm shows a rapid decrease in J_{SC} reaching a minimum of 1.87 mA cm^{-2} when the active layers are placed in an interference minimum. The J_{SC} of the device recovers again with further spacer thickness reaching its original value of 4.37 mA cm^{-2} at 190 nm when the active layers are positioned close to the second maximum. The J_{SC} of the experimental devices follows the sine wave interference pattern expected from the optical model (Figure 4.15) although the peak positions vary slightly due to the inaccuracy of the model data and the simplification of the layers (Section 2.2.3.3). The V_{OC} and *FF* are also displayed in Figure 4.16b showing thickness independence on resistance losses in these devices (section 4.3.2) with the V_{OC} remaining around 0.8 V and the *FF* at ~ 0.4. The *PCE* of the devices therefore varies with the J_{SC} and an increase from 1.4 % to 1.6 % can be achieved by using the optical spacer layer. Depending upon the active layer position in the optical field a large variation can be seen from 0.5 % to 1.6 %.

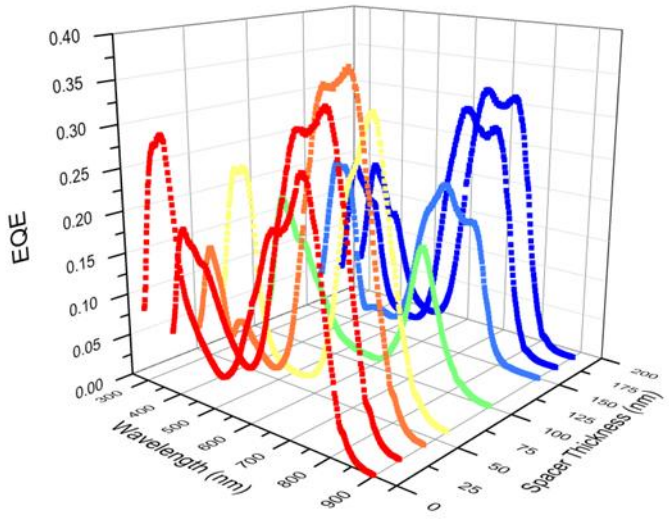

Figure 4.17: EQE spectra for the ClAlPc / C_{60} device as a function of α-NPD:MoO_x optical spacer layer thickness.

To investigate the origins of the variation in J_{SC}, *EQE* measurements were carried out at a range of spacer layer thicknesses, and are shown in Figure 4.17. Both the model (Figure 4.15) and the experimental J_{SC} (Figure 4.16) suggest a wave like change in J_{SC} with spacer thickness and this is reflected in the EQE. The general shape of the EQE follows the absorption spectra for the photoactive layers (Figure 3.1) with bands at 400-500 nm from the C_{60} and at 650-850 nm from the ClAlPc. There is a rise in the ClAlPc peak at 730 nm from 29 % to 38 % with small spacer thicknesses up to 40 nm which suggests this to be optimum position for ClAlPc absorptance. This does not however result in the overall highest J_{SC} as the contribution from C_{60} at 430 nm is reduced in the 40 nm spacer compared to the 20 nm spacer device to 6.9 % compared to 11.9 %. This suggests that the model of the device photocurrent could be improved by including the relative *IQE*s to calculate the photocurrent contributions of the two components. The peak at 730 nm decreases to a minimum of 16 % in the 100 nm spacer device when the photoactive layer is

placed in an optical interference minimum and recovers again back up to 31.1 % with a spacer thickness of 190 nm, higher than the reference device without an optical spacer layer.

In Section 1.5, wavelength-dependent optical interference was discussed as an important factor for optimising device absorptance. Figure 4.18 displays the integrated *EQE* photocurrent and the *EQE* at 430 nm and 730 nm (the peaks of C_{60} and ClAlPc) for the varying spacer thicknesses. It is clear from this plot that individual wavelength patterns do not follow the overall trend in J_{SC}. The 730 nm *EQE* peaks at 40 nm spacer thickness and reaches a minimum at 100 nm. However, the 430 nm peak shows the opposite trend, dipping at 40 nm and peaking at 100 nm. The overall J_{SC} then becomes a combination of all of the different wavelengths which each have maxima at different spacer thicknesses. Optimising device performance using an optical spacer therefore has to account for the whole spectral absorption range and not just the peak wavelength of the photoactive layer.

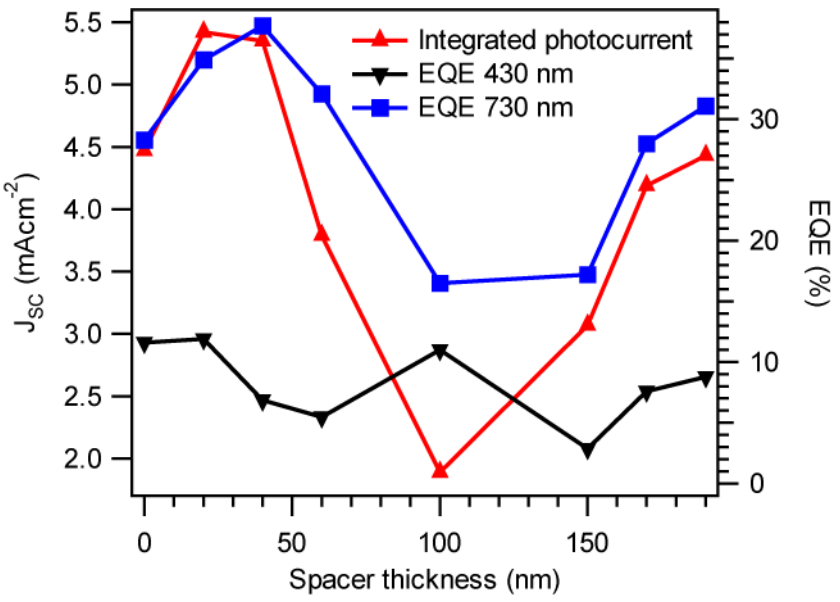

Figure 4.18: Integrated EQE photocurrent and peak wavelength EQE at 430 and 730 nm versus spacer thickness of ClAlPc:C_{60} BHJ device.

4.5 Optical spacer in a PHJ tandem OPV device

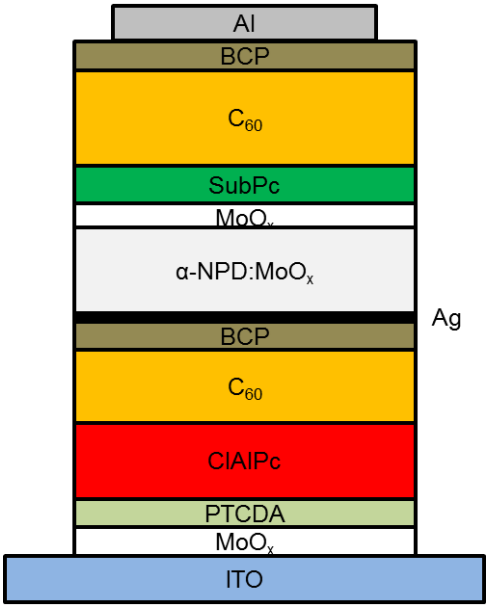

Figure 4.19: Schematic for the ClAlPc / C_{60}, SubPc / C_{60} PHJ tandem OPV device with an α-NPD:MoO_x optical spacer layer.

With the hole transport and optical spacing properties of α-NPD:MoO_x investigated in the previous two sections, the effect of an optical spacer layer in a tandem OPV can be measured. The device structure used (Figure 4.19) has the same photoactive structure as the one used in (Section 3.4) when producing the PTCDA templated tandem device; ITO / PTCDA (1 nm) / MoO_x (5 nm) / ClAlPc (17 nm) / C_{60} (20 nm) / BCP (8 nm) / Ag (0.3 nm) / α-NPD:MoO_x (5%) (d nm) / MoO_x (5 nm) / SubPc (10 nm) / C_{60} (32.5 nm) / BCP (8 nm) / Al. The α-NPD:MoO_x layer is placed between the Ag recombination contact and the MoO_x HTL to transport the holes from the back cell to the recombination layer which matches the two investigated single junction architectures.

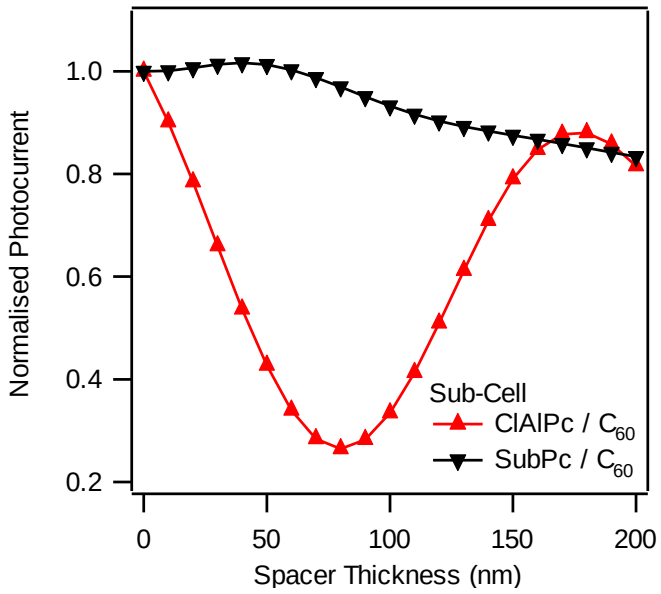

Figure 4.20: Plot of normalised photocurrent of the two sub-cells (ClAlPc / C_{60}, SubPc / C_{60}) versus optical spacer thickness from the optical simulation.

As with the previous section (4.4), a transfer matrix simulation of the absorptance within the investigated device for varied spacer thickness was carried out. The resulting absorptance was integrated over the AM1.5 solar spectrum for each active heterojunction and a plot of the normalised photocurrent is displayed in Figure 4.20. Taking the normalised photocurrent at 0 nm spacer, addition of the optical spacer causes a reduction in the front ClAlPc / C_{60} sub-cell photocurrent as it is pushed into a minimum optical interference at 80 nm. This then increases to an interference peak at 180 nm. The back sub-cell exhibits a slight increase in photocurrent due to the reduction of light absorbed in the front sub-cell, but with increased spacer thickness the photocurrent decreases due to the parasitic absorption of the optical spacer (Figure 4.4). Assuming the maximum photocurrent occurs with 0 nm spacer then the addition of an optical spacer will reduce the photocurrent and the overall performance of the tandem device.

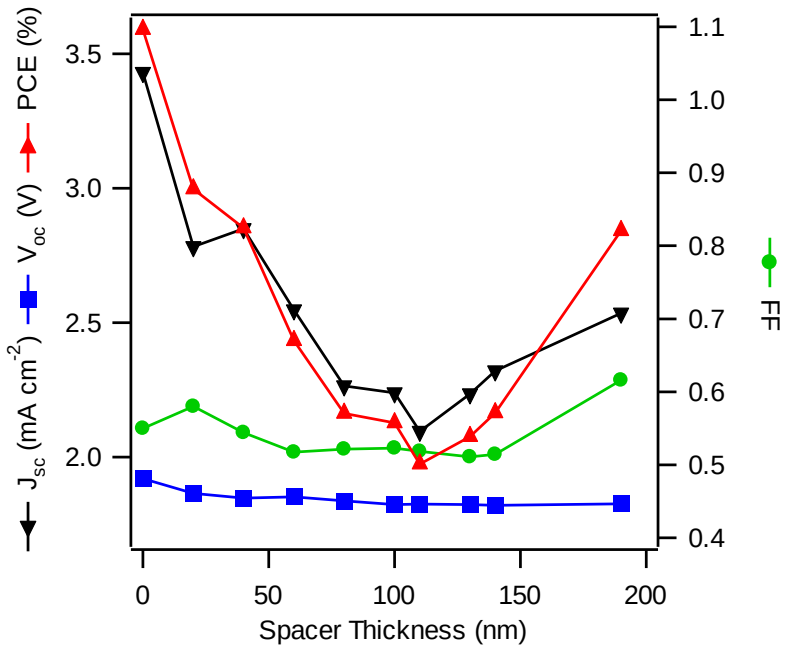

Figure 4.21: Performance characteristics of the ClAlPc / C_{60} : SubPc / C_{60} tandem OPV device versus spacer thickess.

Figure 4.21 presents the performance characteristics of the tandem device (Figure 4.19) as a function of spacer thickness. As expected from the optical simulation, a dramatic reduction in device performance occurs with the addition of an optical spacer. This reduction is mainly attributed to the J_{SC}, which reduces from 3.59 mA cm^{-2} to 2.78 mA cm^{-2} on insertion of the 20 nm optical spacer layer. The photocurrent continues to decrease to 2.10 mA cm^{-2} for a spacer thickness of 110 nm, where the front ClAlPc/C_{60} sub-cell is placed in an interference minimum. There is a gentle recovery in J_{SC}, gradually increasing for larger spacer thickness up to 190 nm as the ClAlPc/C_{60} is moved towards the second maximum. Overall the J_{SC} recovery is low as both sub-cells suffer from increased parasitic absorption of the transport layers. There is little change in the V_{OC} and the *FF* with increased spacer thickness consistent with the previous section (4.4).

As the device was designed and optimised in the previous chapter, the highest efficiency was achieved without an optical spacer as the photoactive layer thicknesses were chosen to match the first optical interference peak. These results present a proof of the concept which will be applicable to other systems.

4.6 Optical spacing effect in a BHJ tandem OPV device.

To investigate the effect of an optical spacer in a BHJ tandem organic solar cell a device structure has been chosen based upon a SubPc:C_{60} BHJ in both sub-cells. This will ensure that both sub-cells cannot be placed in the first optical field maximum and will require optical spacing to maximise the cell photocurrent.

Figure 4.22 shows the device structure used in this study comprising of two SubPc:C_{60} BHJ layers with 1:4 weight ratio which have been shown as the most effective composition.[130] The α-NPD:MoO_x optical spacer layer is placed between the Ag recombination layer and the MoO_x hole transport layer, the same position as in the previous device (Figure 4.19). This allows for optical spacing of the front SubPc:C_{60} cell whilst acting as a HTL for the back sub-cell, transporting holes to the recombination layer.

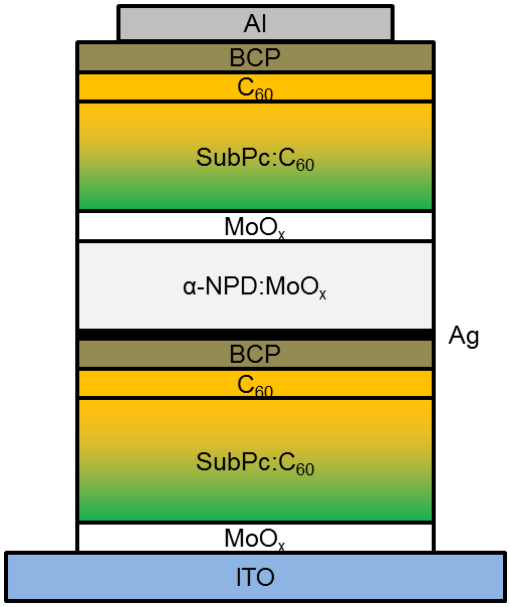

Figure 4.22: Schematic design of the SubPc:C_{60} BHJ tandem OPV device with an α-NPD:MoO_x optical spacer layer.

The tandem device structure consisted of ITO / MoO_x (5 nm) / SubPc:C_{60} (1:4) (70 nm) / C_{60} (10 nm) / BCP (5 nm) / Ag (0.3 nm) / α-NPD:MoO_x (5%) (0-80 nm) / MoO_x (5 nm) / SubPc:C_{60} (1:4) (65 nm) / C_{60} (10 nm) / BCP (8 nm) / Al. The variation in thickness of α-NPD:MoO_x from 0-80 nm allows for the investigation of spacing the front sub-cell away from the Al cathode on the overall device performance. Varying the distance of the front sub-cell from the Al cathode will alter its position in the optical interference field providing a tool for balancing the photocurrents of both sub-cells.

To analyse the magnitude of the individual sub-cell photocurrents with varying optical spacer thickness, a transfer matrix optical model was used to calculate the absorptance profile within the layers of the device stack. For accurate calculation of the SubPc:C_{60} BHJ layers, the optical constants n and k were measured for the 1:4 ratio films using VASE ellipsometry obtained by L.O.T-Oriel GmbH & Co. KG and are shown in Figure (4.23).

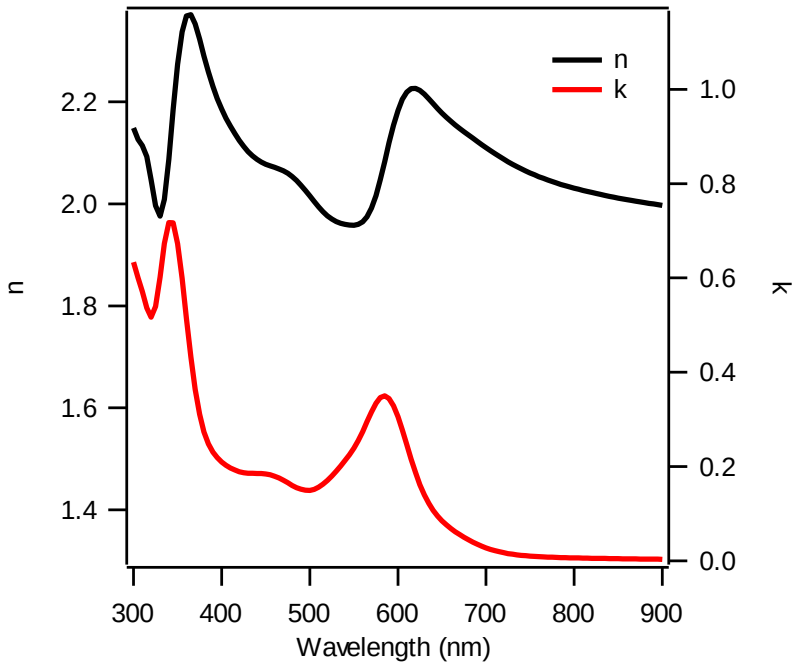

Figure 4.23: Optical constants n and k for SubPc:C_{60} (1:4) BHJ films.

The wavelength dependent absorbtance calculated for the tandem device (Figure 4.22) with an α-NPD:MoO_x thickness of 0 nm and 50 nm is shown in Figure 4.24. The device without an optical spacer layer (Figure 4.24a), shows a large absorptance in the back sub-cell with contributions from both C_{60} (400-450 nm) and SubPc (500-650 nm). In the front sub-cell, a high absorptance is shown from the C_{60} but the SubPc contribution is low as the sub-cell is located at an optical interference minimum for radiation of ~500-600 nm and absorptance is only seen on the anode side fringe of the front sub-cell in the onset of the second interference peak. A high peak is seen at 350 nm from the SubPc although current generation from this is low due to the reduced intensity of the AM1.5 spectrum at this wavelength. With the addition of a 50 nm α-NPD:MoO_x optical spacer layer (Figure 4.24b), the absorptance is still strong in the SubPc section of the back sub-cell but an enhancement is seen in the 500-600 nm region in the front sub-cell as it is positioned in the second interference maxima. The absorptance of C_{60} in the 400-500 nm

section also varies with the spacer layer, with the absorptance peaking in the discrete C_{60} layer in the front sub-cell and a small reduction seen in the BHJ layer.

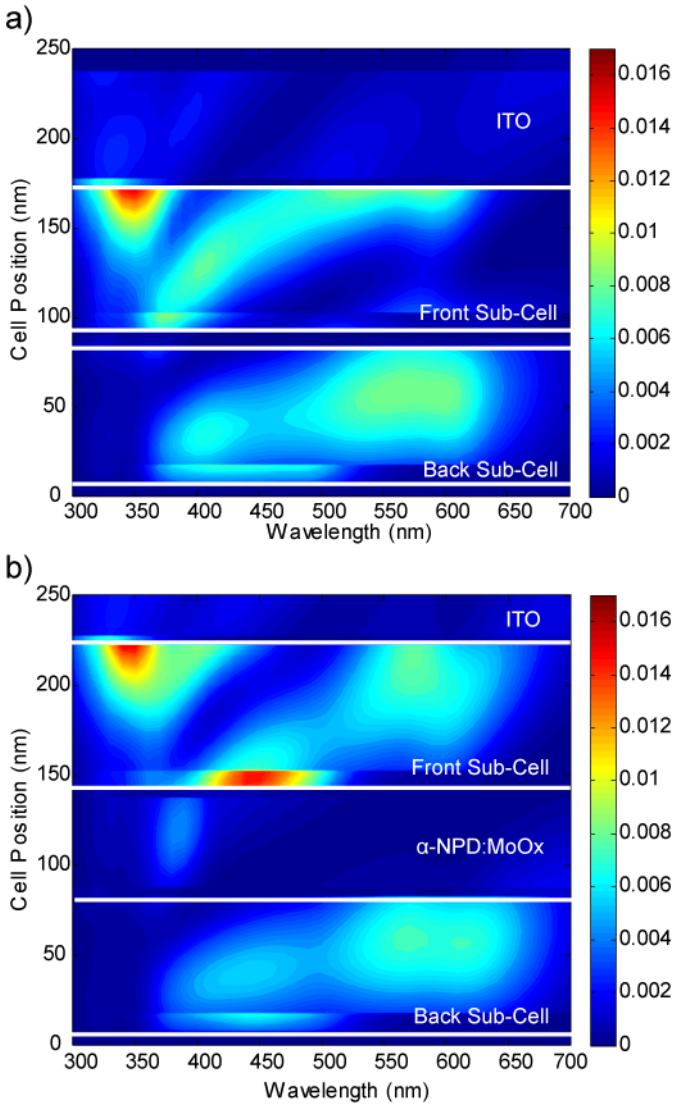

Figure 4.24: Optical simulation plots of spectrally resolved absorptance though the device for two optical spacer thicknesses of a) 0 nm and b) 50 nm.

The absorptance profile of the device was integrated over the AM1.5 solar spectrum to calculate the predicted sub-cell photocurrents. An internal quantum efficiency (*IQE*) was calculated using the method described in section 2.2.3.3 by matching the

absorptance of a single junction device to the measured *EQE*. The single heterojunction device had the structure of the back sub-cell; ITO / MoOx (5 nm) / SubPc:C_{60} (1:4) (65 nm) / C_{60} (10 nm) / BCP (8 nm) / Al. The EQE, calculated absorptance of SubPc:C_{60} and the *EQE* fit is shown in Figure 4.25. A numerical value for the *IQE* is chosen such that the absorptance is scaled to fit with the *EQE*. For the SubPc:C_{60} BHJ cell, an IQE value of 0.8 obtained the best fit.

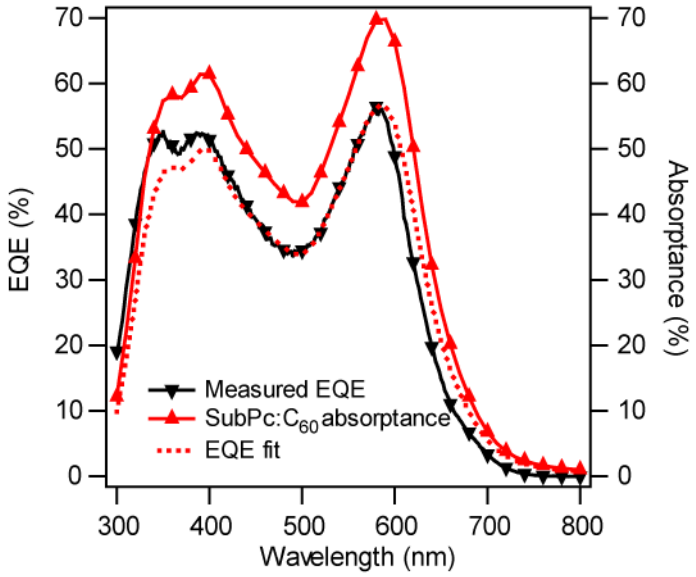

Figure 4.25: Measured external quantum efficiency and modelled absorptance for a SubPc:C_{60} BHJ single junction device. A fit of the measured *EQE* with the absorptance is shown as the red dotted line.

The calculated photocurrent with an *IQE* value of 0.8 is shown in Figure 4.26. A large photocurrent imbalance is shown for a spacer thickness of 0 nm from the low SubPc contribution in the front sub-cell. The photocurrent from this sub-cell improves with increased optical spacer thickness as it is moved into an optimum optical interference position with a spacer thickness of 60 nm. This increased

absorptance in the front sub-cell has a negative effect on the back sub-cell, reducing its photocurrent with increased spacer thickness. An optimum current balancing is observed for an optical spacer thickness just above 40 nm with a predicted photocurrent of 5.1 mA cm^{-2}, which is a 35 % increase in the minimum photocurrent from the front sub-cell of the device without an optical spacer layer. From the optical simulation, a large increase in device performance is expected with addition of an α-NPD:MoO_x optical spacer layer, with the enhancement due to increased photocurrent from the SubPc in the front sub-cell.

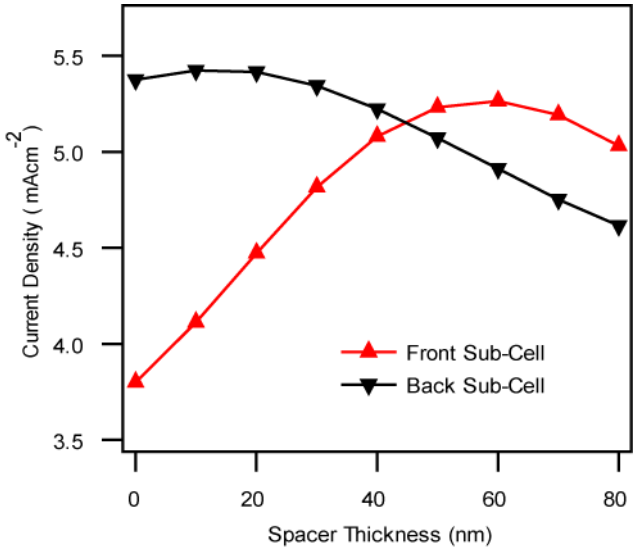

Figure 4.26: Predicted photocurrent for front and back SubPc:C_{60} sub-cell versus optical spacer thickness calculated from the optical simulation.

A series of devices were fabricated with a range of α-NPD:MoO_x thicknesses from 0 – 80 nm with all other layers remaining the same in all devices. This allowed for direct measurement of the optical spacer effect without batch to batch variations of

the photoactive layers. Figure 4.27 displays the device parameters for the fabricated solar cells with varied spacer thickness.

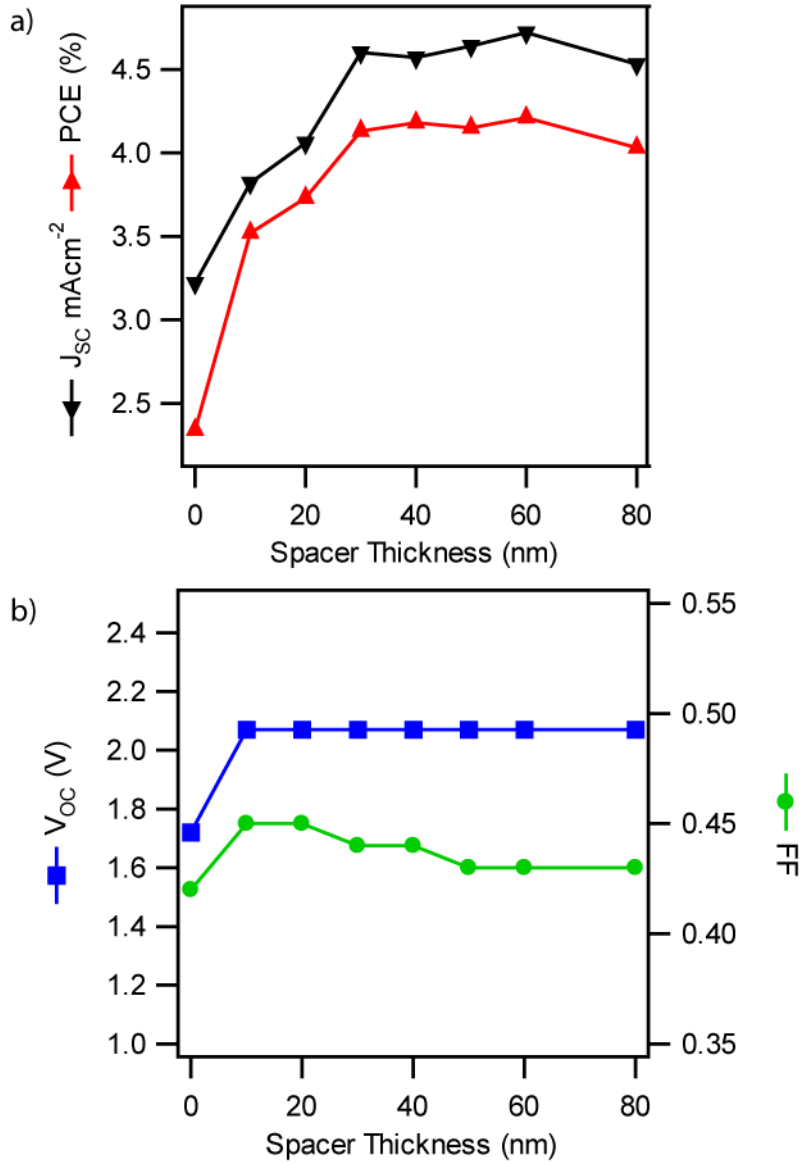

Figure 4.27: Performance characteristics of the SubPc: C_{60} BHJ tandem OPV device versus spacer thickess a) J_{SC} and *PCE* b) V_{OC} and *FF*

The photocurrent increases with spacer thickness, with the *Jsc* rising from 3.22 mA cm^{-2} for an optical spacer of 0 nm, to 4.72 mA cm^{-2} for a 60 nm optical spacer. This improvement in J_{SC} is similar in magnitude to the increase in sub-cell photocurrents calculated from the optical simulation in Figure 4.26. The *FF* remains consistent

across all α-NPD:MoO_x thicknesses indicating little resistance losses from the spacer layer due to its high mobility.[143] The devices show a slight enhancement in V_{OC} on addition of the optical spacer layer from 1.72 V to 2.07 V and it remains independent of further optical spacer thickness increases, close to the summation of the two single junction device voltages (1.05 V). This shows the effectiveness of utilising an α-NPD:MoO_x layer in the recombination zone, leading to a lower voltage loss.

The trend in *PCE* follows the J_{SC}, rising by 80 % from 2.34 % to a maximum of 4.21 % on the addition of a 60 nm optical spacer. The photocurrent and efficiency trend follows that of the optical simulation (Figure 4.26), with highest values achieved using an optical spacer of 40-60 nm where the sub-cell photocurrents are balanced.

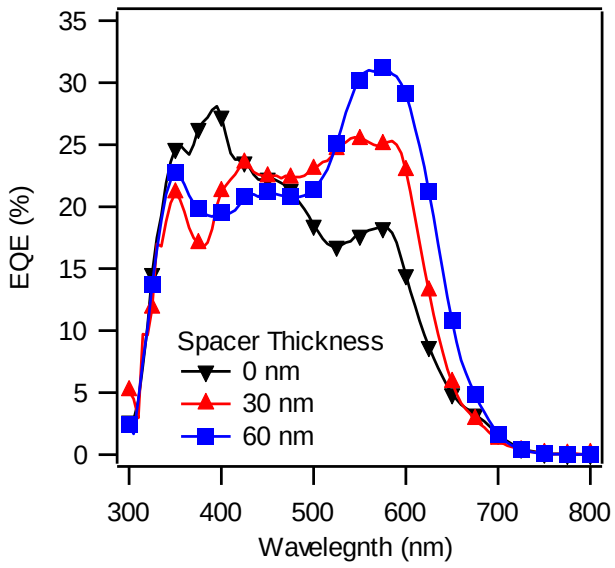

Figure 4.28: EQE spectra of the SubPc:C_{60} BHJ tandem OPV device for three α-NPD:MoO_x thickness; 0 nm, 30 nm, 60 nm.

EQE spectra for the devices with 0, 30 and 60 nm of the α-NPD:MoO_x optical spacer are shown in Figure 4.28. Devices were measured with monochromatic light conditions and no external light bias. The reference device without the optical spacer

exhibits a peak in the SubPc absorption region (590 nm) of 17 % with a higher peak in the C_{60} absorption region (450 nm) of 23 %. The device with a 30 nm optical spacer displays a similar peak in the C_{60} absorption region, but an improvement in the SubPc region (500–600 nm) is seen with a peak of 24 % from increased contribution of the SubPc. Further enhancement with a 60 nm optical spacer is present in this region with a peak at 590 nm of > 30%. This increase in the SubPc *EQE* shows the improvements in the sub-cell balancing in this absorption region as seen in the optical model (Figure 4.24b), with an increase in SubPc absorptance from 500-600 nm in the front sub-cell on the addition of an optical spacer. The shift in the absorptance profile of the C_{60} region seen in Figure 4.24 provides no improvement in the monochromatic *EQE* between 400-450 nm.

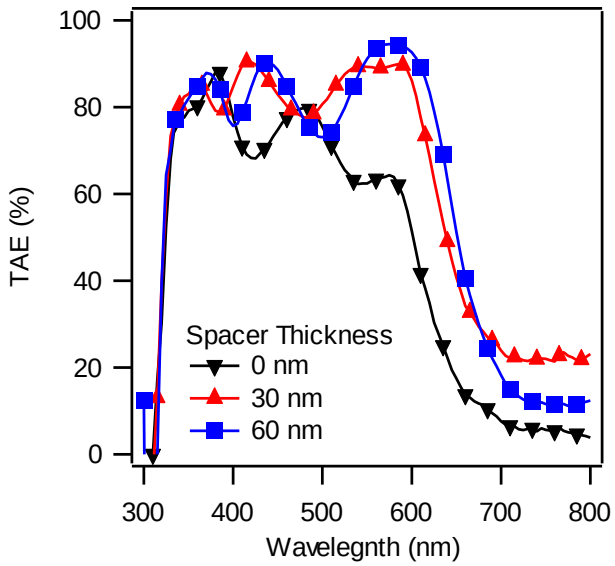

Figure 4.29: *TAE* spectra of the SubPc:C_{60} BHJ tandem OPV device for three α-NPD:MoO_X thickness; 0 nm, 30 nm, 60 nm.

Increased absorptance in the SubPc region of the front sub-cell is suggested by the optical model and a measurement of the total absorption efficiency efficiency (*TAE*) in the device is presented in Figure 4.29. This represents light absorbed in all layers

of the device taken from reflection measurements of a double pass of monochromatic light through the device. As with the optical simulation and the *EQE* measurement, a low absorption for the SubPc peak at 590 nm is seen in the *TAE* plot (Figure 4.29) with no spacer layer. This increases for the device with a 30 nm spacer layer with improved absorption above 600 nm. Further improvements in absorption are also displayed for the 60 nm spacer device, where the shape of the SubPc peak follows the profile of the *EQE* (Figure 4.28). The *TAE* corroborates the optical simulation and the *EQE*, showing that the BHJ tandem device has been optimised by positioning both sub-cells in interference peak maxima for SubPc absorption to balance the photocurrents of both sub-cells.

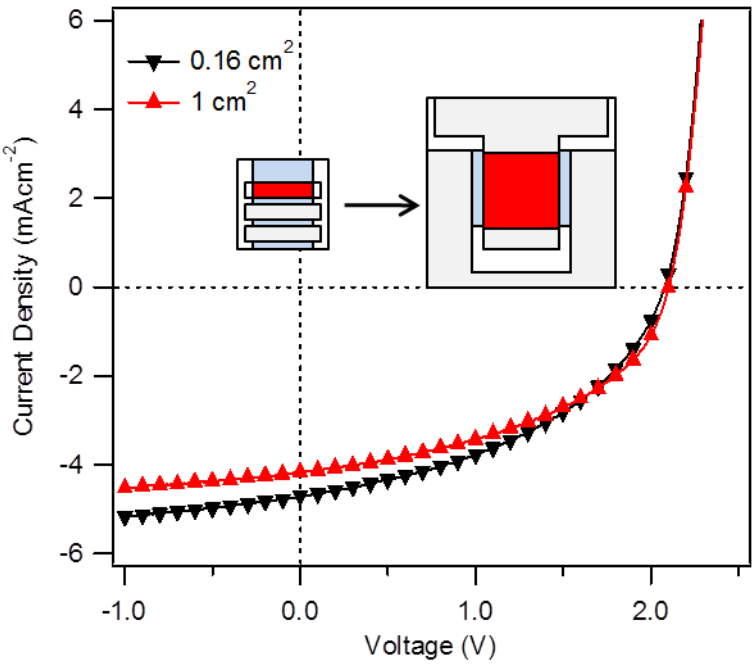

Figure 4.30: *J-V* plots of the SubPc:C_{60} BHJ tandem OPV device with 40 nm α-NPD:MoO_x for a 0.16 cm^2 and a 1cm^2 device.

Device Size (cm^2)	J_{SC} (mA cm^{-2})	V_{OC} (V)	*FF*	*PCE* (%)
0.16	4.70	2.08	0.44	4.32
1	4.16	2.10	0.47	4.10

Table 4.1: Device parameters of the SubPc:C_{60} BHJ tandem OPV device with 40 nm α-NPD:MoO_x for a 0.16 cm^2 and a 1cm^2 device.

Depending upon the fabrication method, the active area is usually defined by the overlap of the ITO and the evaporated metal cathode. There is not a standard device area used internationally and variations from 1 mm diameter circles up to larger module sizes have been published.[144] There are some reports that measurement inaccuracies occur at small active areas from inhomogeneity in the light source and shadow masking effect of the cathode area.[145] The trend in device fabrication is to move away from small area pixel size into larger sizes of at least 1 cm^2 as a standard for certification.[146] In Figure 4.30 a comparison of the standard 0.16 cm^2 pixel used throughout this thesis and a 1 cm^2 active area pixel of the 40 nm spacer BHJ device (Figure 4.24) is shown. This pixel design has been used as a standard device for degradation measurements. The larger area allows for encapsulation using a glass cover slip which is sealed using light-curable epoxy purchased from Ossila Ltd.[147] A decrease in J_{SC} from 4.70 mA cm^{-2} to 4.16 mA cm^{-2} is shown when the pixel size increases from 0.16 cm^2 to 1 cm^2. The V_{OC} and *FF* are similar when moving up device size but the overall efficiency is reduced from 4.32 % to 4.10 %.

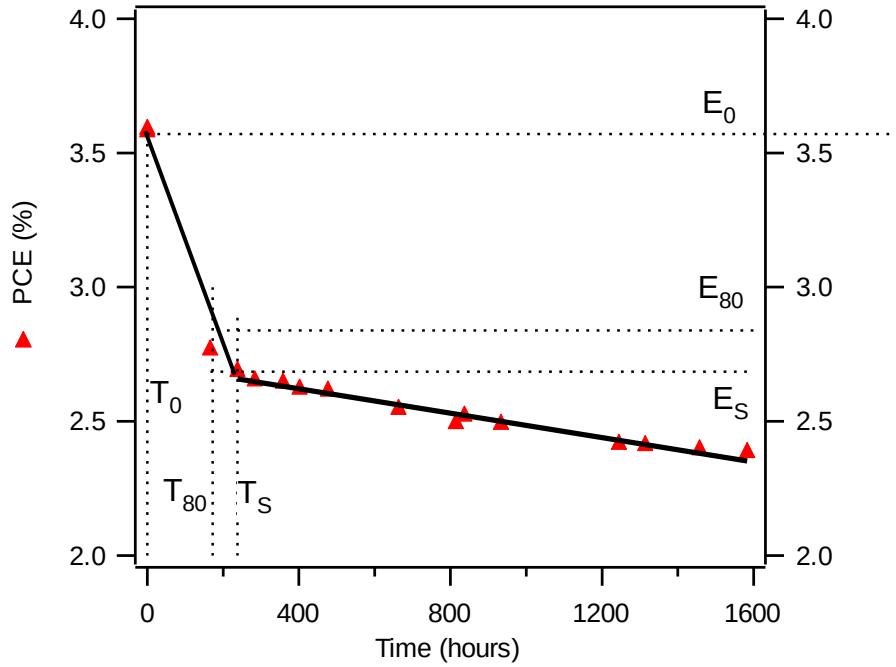

Figure 4.31: Stability plot of *PCE* for the encapsulated 1cm^2 SubPc:C_{60} BHJ tandem OPV device under constant illumination 100 mWcm^{-2}.

The SubPc:C_{60} tandem OPV device was subject to stability measurements under constant illumination at 100 mW cm^{-2} using a home built set up and the *PCE* is displayed in Figure 4.31 as a function of time. A rapid decrease in *PCE* is initially seen and T_{80} (the time at which the *PCE* is 80 % of the initial value) is approached after 172 hours. This is the initial 'burn in' degradation seen for many devices.[148] After this, a second testing time (T_S) is taken and stability to T_{S80} is measured. [149] After nearly 1600 hours T_{S80} had not been reached so a linear extrapolation was performed to calculate the lifetime of the device which occurred at 2452 hours. The lifetime of these devices still has a long way to improve although promising data has been published on small molecule tandem OPV device.[150]

4.7 Summary

In this chapter α-NPD was used as a hole transporting and optical spacer layer in multiple OPV devices. The conductivity of α-NPD was improved by co-deposition with a small % of MoO_x with an emergence of a radical cation peak at 500 nm in the absorption spectra from the electron transfer. The Fermi level of the α-NPD layer shifts towards the HOMO on addition of MoO_x as is eventually pinned 0.5 eV above the HOMO. A similar topography was seen for different MoO_x concentrations with very low RMS roughness.

α-NPD:MoO_x was shown to be an effective HTL for SubPc / C_{60} PHJ devices and as an optical spacer layer for ClAlPc:C_{60} BHJ devices, with transport layer thicknesses over 100 nm without loss in V_{OC} or *FF*. Implementation of the α-NPD:MoO_x optical spacer into a PHJ tandem OPV device showed comparable performance to the reference device, although optical simulations showed that device performance would be better without the optical spacer layer.

Finally, the α-NPD:MoO_x optical spacer layer was used as a tool to optimise the current balancing in a SubPc:C_{60} based tandem OPV device. Optical simulations showed a mismatch in the sub-cell photocurrents without an optical spacer and the possibility of a 30 % gain with an optical spacer of ~40 nm. Experimental results showed an improvement in J_{SC} and V_{OC} with optical spacer thickness, reaching an optimal efficiency of 4.21 % for a 60 nm spacer compared to 2.34 % without. The *EQE* and *TAE* measurements showed that the photocurrent gain was due to an increase in SubPc absorption in the front sub-cell. Increasing pixel size to $1cm^2$ showed a small decrease in performance to 4.10 % and it had a good stability for ~100 days under constant illumination.

Chapter 5 Multi-heterojunction cascade device

In this chapter a new device structure consisting of a multi-heterojunction cascade is presented as a method of increasing the photocurrent in PHJ OPV devices by creating two D/A heterojunctions in a cascade structure. α-sexithiophene (α-6T) has been selected as the interlayer for the SubPc / C_{60} heterojunction to create a dual heterojunction device and PL spectroscopy is used to show exciton dissociation at both interfaces. Subsequently, the performance characteristics are shown for the cascade device and for the thickness dependence of the α-6T layer. Finally, this device architecture is investigated using a ClAlPc / C_{60} heterojunction.

5.1 Introduction to cascade heterojunctions

Many approaches have been undertaken to improve the photocurrent in OPV devices such as forming a BHJ from intermixing of the donor and acceptor materials to increase the D / A interface area,[128] and using structural templating layers to adjust the stacking orientation of the donor molecules to improve the exciton diffusion lengths.[133] Another method to improve exciton dissociation is to construct a cascade heterojunction,[151] either by adding a thin layer between the donor and acceptor to provide an energy gradient for charge separation,[76,81] or by using multiple donor materials with cascading exciton energies to broaden the spectral absorption and promote exciton dissociation to the interface.[79,80] Multiple heterojunction dissociation can also be achieved in a three-layer cascade device by having two heterojunctions that form an interface gap large enough for exciton dissociation.[53] In these devices the middle organic semiconductor acts as both an electron acceptor and an electron donor for each of the heterojunctions.

5.2 α-6T / SubPc / C_{60} cascade device

Figure 5.1a. displays the energy level diagram of a SubPc / C_{60} heterojunction as found in the PHJ single devices from section 4.3. Exciton dissociation occurs at the D/A heterojunction interface with the thickness of the D and A layer limited by the small L_D of the materials.[127] Excitons generated at the anode side of the SubPc layer have to diffuse through the layer to reach the D / A heterojunction without succumbing to recombination which becomes a problem as the thickness of D approaches L_D. A way to improve exciton dissociation would be to provide a second heterojunction at the anode side of the SubPc to reduce the effective distance needed to diffuse to a heterojunction. Figure 5.2b presents the energy level diagram of a cascade heterojunction of α-6T / SubPc / C_{60}. In these devices, α-6T was chosen for the second heterojunction as it possesses a high hole mobility[152] and a HOMO level of 4.95 eV[111] giving an interface HOMO energy gap of 0.6 eV with SubPc; large enough to overcome the exciton binding energy for dissociation. This should provide two heterojunctions for exciton dissociation in SubPc. The cascade device structure investigated in this study is shown in Figure 5.2c.

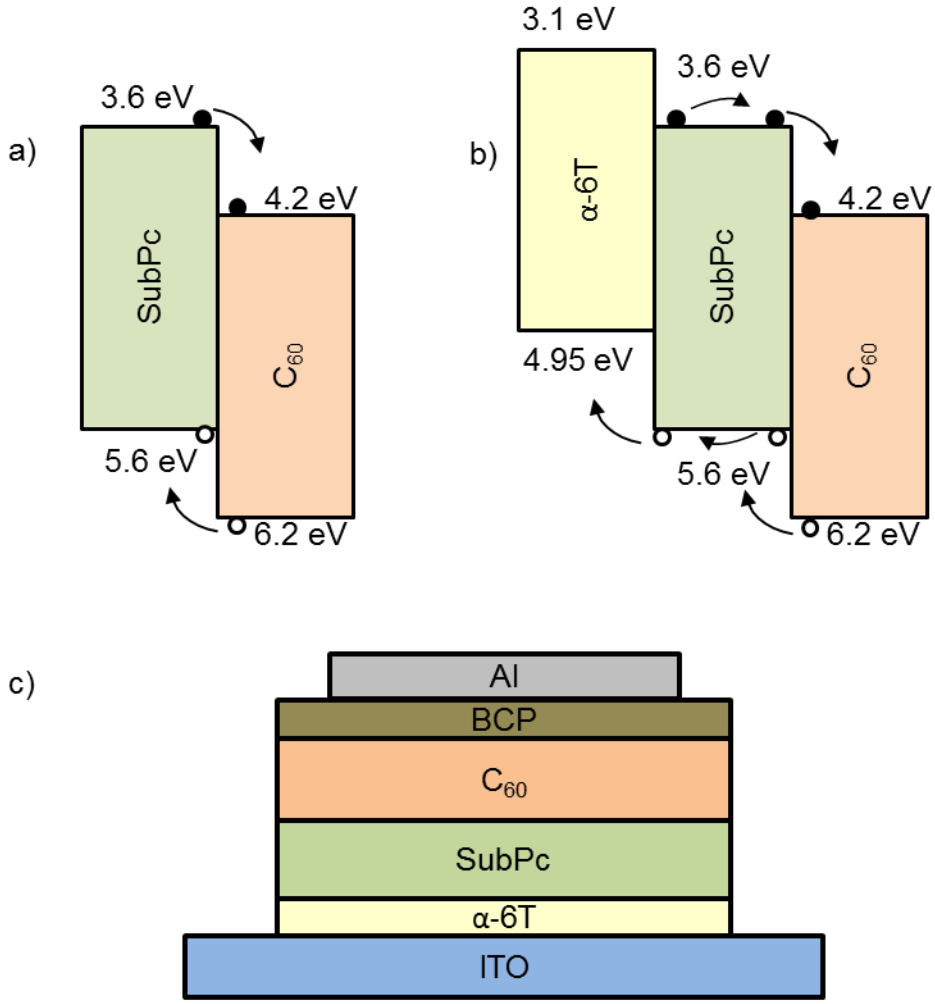

Figure 5.1: a) Energy level diagram of a SubPc / C_{60} heterojunction displaying exciton dissociation. **b)** Energy level diagram of α-6T / SubPc / C_{60} cascade heterojunction displaying two exciton dissociation interfaces for the SubPc layer. **c)** Device structure for the α-6T / SubPc / C_{60} cascade OPV device.

5.2.1 AFM

The topography AFM images of multiple thicknesses of α-6T; 5 nm, 10 nm and 30 nm are shown in Figure 5.2. The topography of the 5 nm layer, Figure 5.2a, displays a pitted structure with 4 nm trough to peak heights and several larger crystallites of 14 nm in height. The overall surface has an RMS roughness value of 2.2 nm. Increased thickness of α-6T to 10 nm (Figure 5.2b) reveals larger grains developing

and the large crystallites have increased to 30 nm in height. The RMS roughness doubles to 4.6 nm and the thicker 30 nm α-6T layer has a further increase in roughness to 8.9 nm with grain size increasing again. The larger roughness of the thick layers may cause incomplete coverage of subsequent layers of SubPc and C_{60} so the 5 nm layer will be investigated in the device structure (Figure 5.1c).

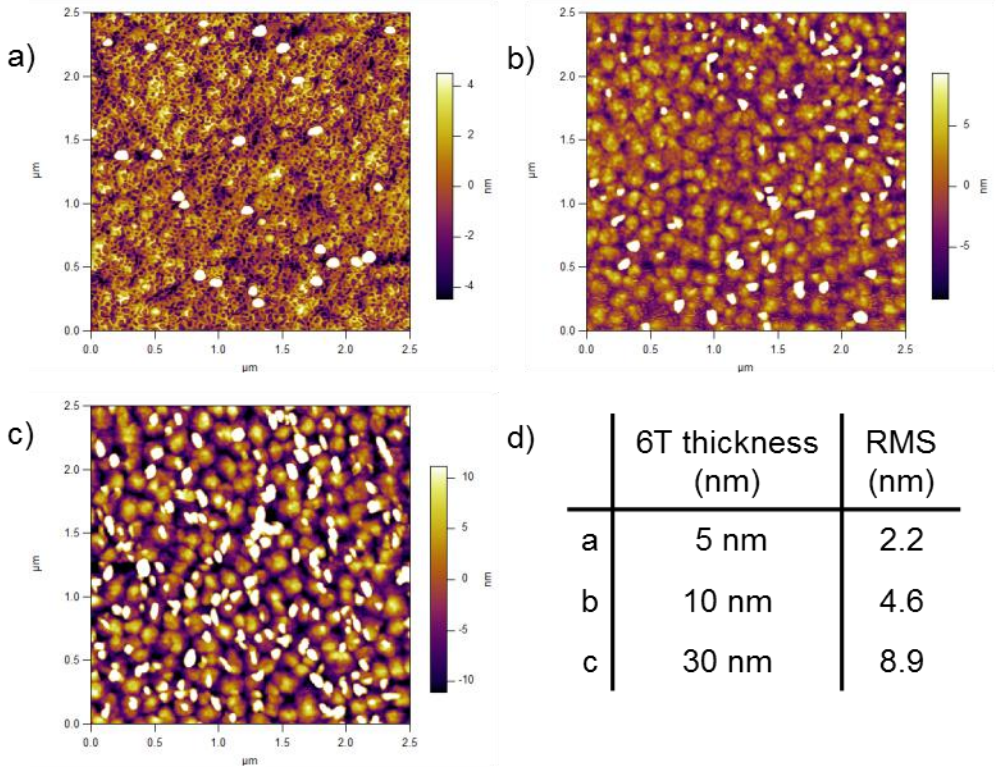

	6T thickness (nm)	RMS (nm)
a	5 nm	2.2
b	10 nm	4.6
c	30 nm	8.9

Figure 5.2: AFM images of ITO / α-6T; **a)** 5nm, **b)** 10 nm, **c)** 30 nm and **d)** the RMS roughness for the three layers.

5.2.2 Photoluminescence

To verify that exciton dissociation occurs at the interface between α-6T and the SubPc the photoluminescence (PL) quenching effects of α-6T and C_{60} on SubPc films were measured. Figure 5.3 displays the PL emission spectra of SubPc excited

at 575 nm, with peaks seen at 625 and 714 nm. The peak at 714 nm corresponds to emission from molecular aggregates.[153] With the addition of a 10 nm layer of C_{60} (a thin layer used to minimise optical interference), the signal is highly quenched implying exciton dissociation at the SubPc / C_{60} interface as expected from device data.[97] The PL spectra for the α-6T / SubPc bilayer also show quenched emission, indicating that excitons can be dissociated at this interface and could provide a boost to the photocurrent in a cascade structure, although the quenching efficiency is much lower than that of SubPc/C_{60}. The dual heterojunction cascade structure displays the lowest PL signal due to the quenching at both heterojunction interfaces. The quenching ratio for both SubPc: α-6T / SubPc and SubPc / C_{60}: α-6T / SubPc / C_{60} are ~ 40 % which indicates that the increased quenching of the SubPc is due to the addition of the α-6T layer to create a second heterojunction for exciton dissociation and not an alteration of the SubPc / C_{60} interface.

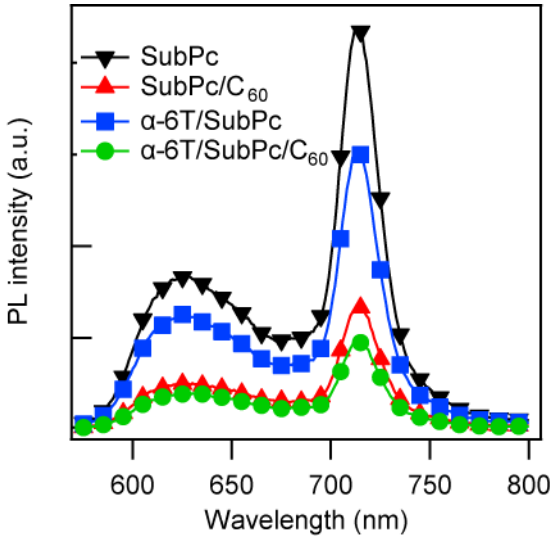

Figure 5.3: PL spectra (575 nm excitation) of 15 nm SubPc films with and without 10 nm C_{60} and 5 nm α-6T quenching layers grown on quartz glass.

5.2.3 Device Data

The cascade device structure investigated in Figure 5.1c has the structure ITO / α-6T (5 nm) / SubPc (14 nm) / C_{60} (32.5 nm) / BCP (8 nm) / Al. To further prove that exciton dissociation occurs at each interface within the cascade device, control devices of α-6T / SubPc and SubPc / C_{60} D/A heterojunctions were fabricated using the same layer thicknesses. The J-V characteristics of all three devices are shown in Figure 5.4 and the performance parameters are summarised in Table 5.1**.** The SubPc / C_{60} device displays a J_{SC} of 5.23 mA cm^{-2} and a V_{OC} of 0.74 V. A low *FF* of 0.47 is observed due to the S-shaped kink in device operation giving an overall efficiency of 1.81 %. The V_{OC} and *FF* are reduced from the previous SubPc / C_{60} devices presented in Figure 4.9 due to the lack of MoO_x which improves hole extraction.[60] The α-6T / SubPc device acts as an effective heterojunction displaying a V_{OC} of 0.96 V, a J_{SC} of 2.41 mA cm^{-2}, a *FF* of 0.52 and a *PCE* of 1.19 %. This proves that exciton dissociation is occurring at the α-6T / SubPc interface and demonstrates the ambipolar ability of SubPc to act as an efficient donor and acceptor.[98,154] The α-6T / SubPc / C_{60} cascade device shows an increase in J_{SC} to 6.23 mA cm^{-2} representing a 20 % improvement over the SubPc / C_{60} device due to the additional exciton dissociation at the α-6T / SubPc interface. A V_{OC} of 0.78 V was achieved which shows an increase over the 0.4 V obtained for an α-6T / C_{60} device[112] with reduced recombination loss of the bound CT state proposed as the mechanism for the improved V_{OC} in the cascade structures.[76] The reduction in *FF* to 0.34 compared to the 0.47 for the SubPc / C_{60} device results in an overall *PCE* of 1.66 % which is lower than the SubPc / C_{60} device. The origin of the S-shape kinks in this system is from poor hole extraction at the ITO / SubPc interface leading to a mismatch in

charge carrier density in the SubPc. MoO_x has been used as an effective hole extraction layer in SubPc / C_{60} device leading to a reduction in the S-shape kink and improved performance.[60]

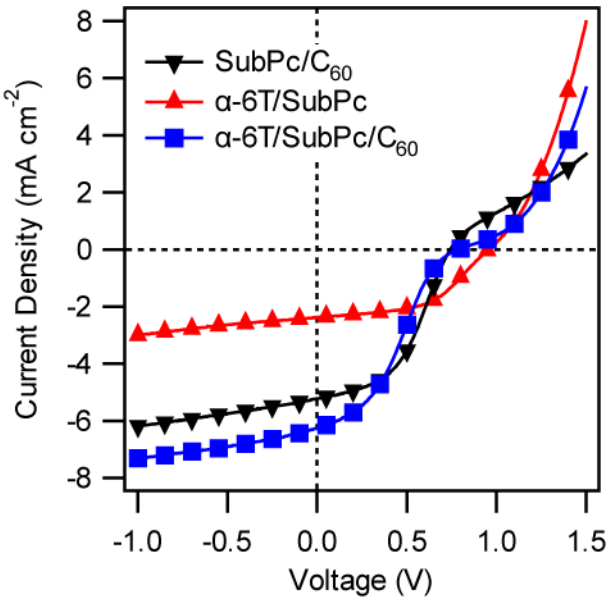

Figure 5.4: *J-V* plots of SubPc / C_{60}, α-6T / SubPc and α-6T/ SubPc / C_{60} OPV devices under AM1.5 100 mW cm^{-2} simulated light.

Device Structure (nm)	J_{SC} (mA cm^{-2})	V_{OC} (V)	*FF*	*PCE* (%)
SubPc (14) / C_{60} (32.5)	5.23	0.74	0.47	1.81
α-6T (5) / SubPc (14)	2.41	0.96	0.52	1.19
α-6T (5) / SubPc (14) / C_{60} (32.5)	6.23	0.78	0.34	1.66

Table 5.1: Device parameters of SubPc / C_{60}, α-6T / SubPc and α-6T/ SubPc / C_{60} OPV devices

To investigate the origin of the increased photocurrent in the cascade device, the *EQE* was measured. The *EQE* for the cascade device along with the two substituent heterojunction devices are shown in Figure 5.5. The SubPc / C_{60} device shows a photocurrent contribution from both the C_{60} (400-450 nm) and the SubPc (500-600 nm). A large peak in *EQE* in the SubPc region is observed of 42 % at 590 nm. The α-6T / SubPc device only shows contribution from the SubPc layer as the thin α-6T layer absorbs only a small fraction of the light compared to the SubPc. The cascade device shows similar *EQE* in the C_{60} region at 400 nm, indicating that the SubPc / C_{60} interface has not been modified by the addition of the α-6T layer ruling out this as the cause for the increase in J_{SC}. The increase in *EQE* occurs from 500 – 600 nm in the SubPc region, with a peak *EQE* of 64 % at 590 nm an improvement of ~50 % from the SubPc / C_{60} device. This increase in photocurrent indicates that excitons generated in the SubPc layer are able to dissociate at both the α-6T and the C_{60} interface with the SubPc acting simultaneously as an acceptor for α-6T and a donor for C_{60}.

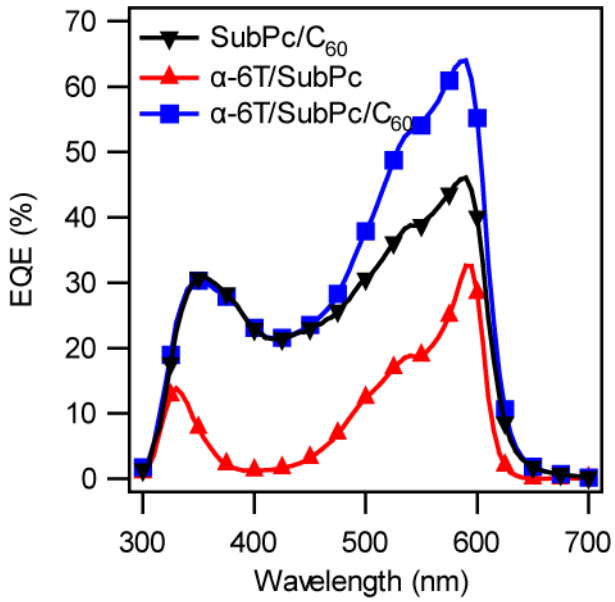

Figure 5.5: *EQE* spectra of SubPc / C_{60}, α-6T / SubPc and α-6T/ SubPc / C_{60} OPV devices.

With only a thin 5 nm layer of α-6T used in the cascade device, little or no contribution was shown from the α-6T at the α-6T / SubPc interface. To investigate the contribution of α-6T and to display a device with three contributing layers, the thickness of α-6T was altered in the cascade device up to 30 nm and the J-V characteristics are shown in Figure 5.6 with the performance parameters summarised in Table 5.2. For these devices the thickness of SubPc was changed to 15 nm. The J_{SC} of the reference SubPc / C_{60} devices displays a J_{SC} of 5.42 mA cm^{-2} and a V_{OC} of 0.81 V giving a slightly higher efficiency of 2.11 % than the device shown in Figure 5.4. The cascade devices all show an increase in J_{SC} of over 17 % compared to the SubPc / C_{60} reference device, similar to the cascade devices presented previously (Figure 5.4). There is little difference shown between the 5nm and the 20 nm α-6T thicknesses, with both devices achieving a *PCE* of ~ 1.7 %. An increase in J_{SC} is seen on the addition of a 30 nm α-6T layer in the cascade device to 6.53 mA cm^{-2} from the 6.38 mA cm^{-2} produced in the 5nm α-6T cascade device suggesting a possible contribution from the α-6T. The V_{OC} shows a slight decrease with thickness of α-6T and the *FF* slightly improves. A higher *PCE* is therefore achieved for the 30 nm 6T cascade device of 1.75 %. The series resistance of the cascade device decreases with α-6T thickness as displayed in Figure 5.6 where there is a reduction in the S-shaped kink in the *J-V* plot and higher current is passed at forward bias. This suggests that the α-6T layer is moving towards full coverage of the ITO (Figure 5.2) and increasing the charge extraction from the SubPc layer.

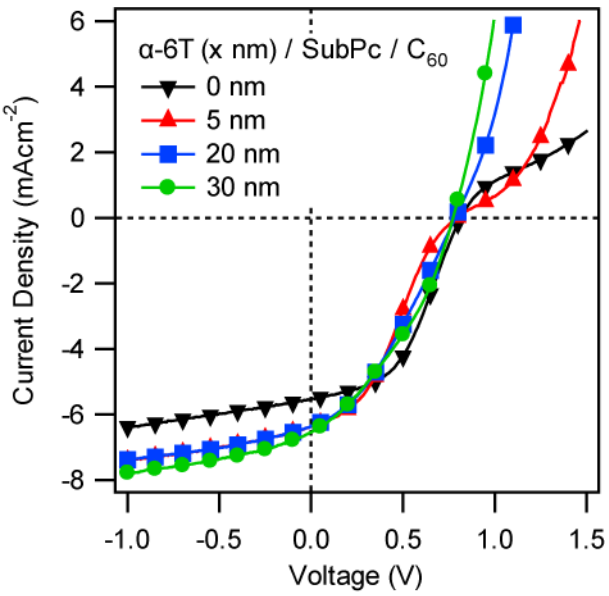

Figure 5.6: *J-V* plots for the α-6T / SubPc / C_{60} cascade OPV devices with multiple thicknesses of α-6T; 0, 5, 20 and 30 nm under simulated AM1.5 illumination.

α-6T Thickness (x nm)	J_{SC} (mA cm^{-2})	V_{OC} (V)	*FF*	*PCE* (%)
0 nm	5.42	0.81	0.48	2.11
5 nm	6.38	0.79	0.34	1.70
20 nm	6.35	0.78	0.34	1.69
30 nm	6.53	0.77	0.35	1.75

Table 5.2: Device parameters for the α-6T / SubPc / C_{60} cascade OPV devices with multiple thicknesses of α-6T; 0, 5, 20 and 30 nm under simulated AM1.5 illumination

To evaluate whether the increase in J_{SC} observed for the devices in Figure 5.6 is due to the contribution from α-6T, *EQE* and *TAE* were measured. Figure 5.7a presents the *EQE* for the cascade devices with the three thicknesses of α-6T and the SubPc / C_{60} reference device. Similar to previous devices (Figure 5.5), a large increase in *EQE* is displayed from 500 – 600 nm on the addition of an α-6T layer to the SubPc / C_{60} heterojunction to create a cascade device, peaking above 60 % at 590 nm. With an increase in α-6T thickness, the peak at 590 nm shows little alteration signifying no improvement in exciton dissociation in the SubPc layer with the rougher α-6T layer (Figure 5.2). With the thicker α-6T layers of 20 nm and 30 nm, there is an

emergence of a peak at 400 nm which increases for the 30 nm layer. This is due to the α-6T absorption and is the cause for the increase in J_{SC} observed. This therefore displays a three layer cascade heterojunction device with all layers contributing to the photocurrent.

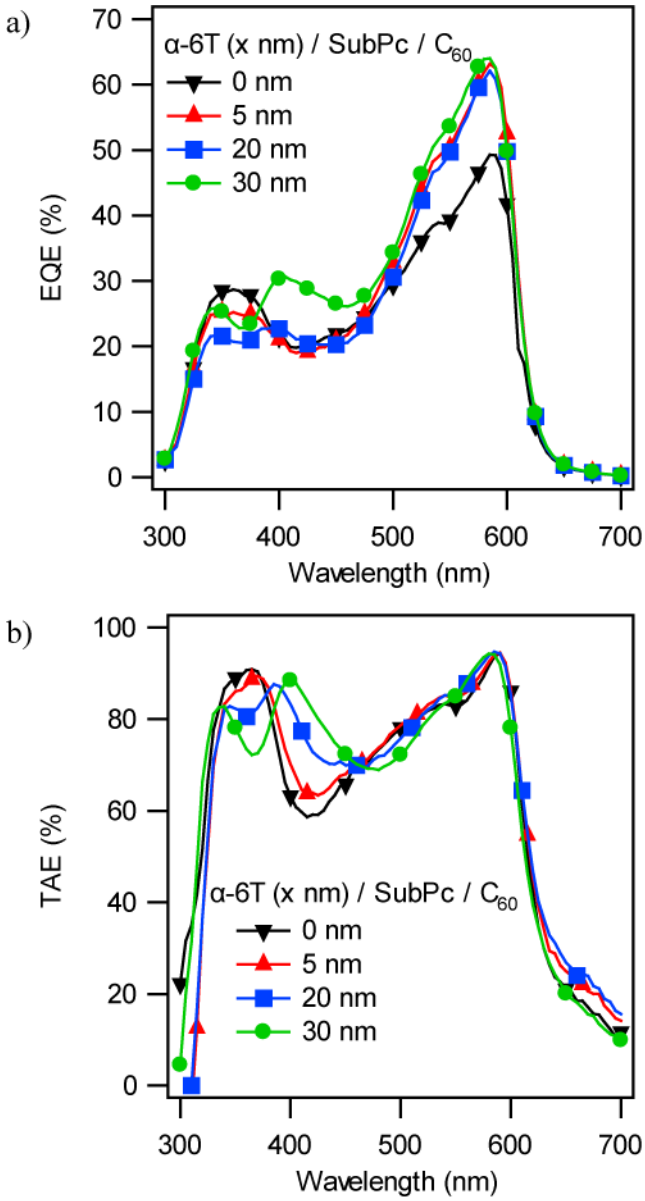

Figure 5.7: a) *EQE* spectra and **b)** TAE spectra of α-6T / SubPc / C_{60} cascade OPV devices with multiple thicknesses of α-6T; 0, 5, 20 and 30 nm.

To account for the increased α-6T contribution in the *EQE* the *TAE* for the cascade devices were measured and are displayed in Figure 5.7b. There was no change

observed in the SubPc absorption from 500 – 600 nm. The emergence of the same peak in the *EQE* at 400 nm was also present from the increased absorption of the thicker α-6T layers.

5.3 α-6T / ClAlPc / C_{60} Cascade Device

The overall *PCE* of the α-6T / SubPc / C_{60} cascade device is lower than the substituent heterojunctions due to the reduction in *FF* in the device. Another cascade device structure based upon ClAlPc was investigated to see the cascade structure could provide an improvement in *PCE* over a PHJ device. Figure 5.8 presents the energy level diagram for the two layer heterojunction and the three layer cascade heterojunction system. The HOMO level of 5.4 eV for the ClAlPc fits well into the α-6T / ClAlPc / C_{60} cascade structure, ensuring that there is 0.3 eV ΔHOMO energy gap between each layer for efficient exciton dissociation. Figure 5.8c displays the cascade device structure used in this investigation. It was composed of ITO / α-6T (5 nm) / ClAlPc (20 nm) / C_{60} (40 nm) / BCP (8 nm) / Al. The ClAlPc / C_{60} heterojunction thickness was chosen as it has been presented as an optimum thickness in reported devices.[92]

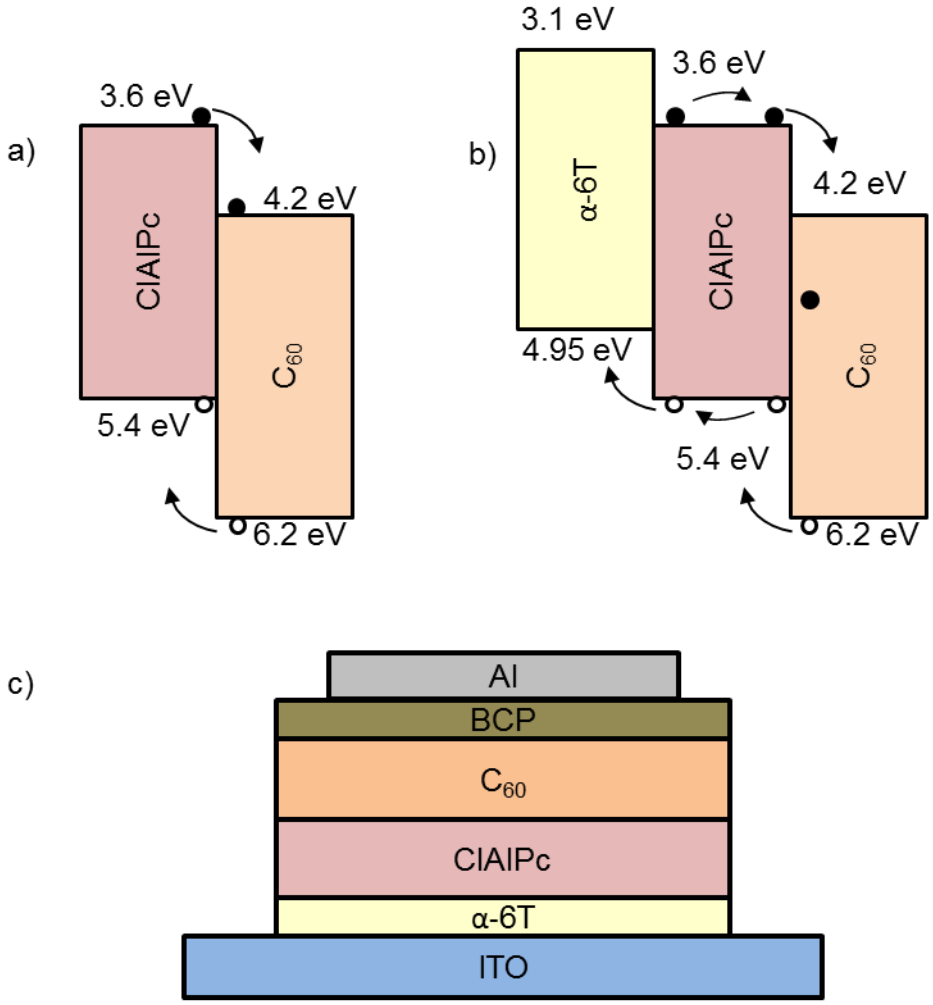

Figure 5.8: a) Energy level diagram of a ClAlPc / C_{60} heterojunction displaying exciton dissociation. **b)** Energy level diagram of α-6T / ClAlPc / C_{60} cascade heterojunction displaying two exciton dissociation interfaces for the ClAlPc layer. **c)** Device structure for the α-6T / ClAlPc / C_{60} cascade OPV device.

The *J-V* characteristics for the cascade device and the two substituent heterojunctions are shown in Figure 5.9 with the performance parameters summarised in Table 5.3. The ClAlPc / C_{60} device has a J_{SC} of 3.16 mA cm^{-2}, a V_{OC} of 0.69 V, *FF* of 0.52 and a *PCE* of 1.13 %. The performance of this device is slightly increased over the similar system in Figure 3.17 because of the increased thickness of C_{60} improving the J_{SC}. There is a reduction in V_{OC} seen due to absence

of MoO_x.[60] The second heterojunction of α-6T / ClAlPc also shows adequate performance with a J_{SC} of 1.53 mA cm^{-2}, V_{OC} of 0.50 V and a *FF* of 0.56 giving an overall *PCE* of 0.42 %. This proves that ClAlPc can act as an acceptor for α-6T, as seen with SubPc, with a higher *FF* than the C_{60} system. The low J_{SC} for this device could be due to the poor alignment of ClAlPc to the optical interference peak as it is positioned close to the Al cathode (Section 4.4). In the α-6T / ClAlPc / C_{60} cascade device, a large improvement in J_{SC} of over 50 % is seen increasing from 3.16 mA cm^{-2} to 5.08 mA cm^{-2} which is indicative of exciton dissociation in the ClAlPc layer occurring at two interfaces. This improvement is much larger than that seen in the α-6T / SubPc / C_{60} device (Figure 5.4). The V_{OC} of the cascade device decreases from that of the ClAlPc / C_{60} device from 0.69 V to 0.56 V though it is still larger than the α-6T/C_{60} V_{OC} of 0.4 V.[112] The cascade device maintains a *FF* of 0.51 which results in an overall *PCE* of 1.46 %, a 29 % increase over the ClAlPc / C_{60} device.

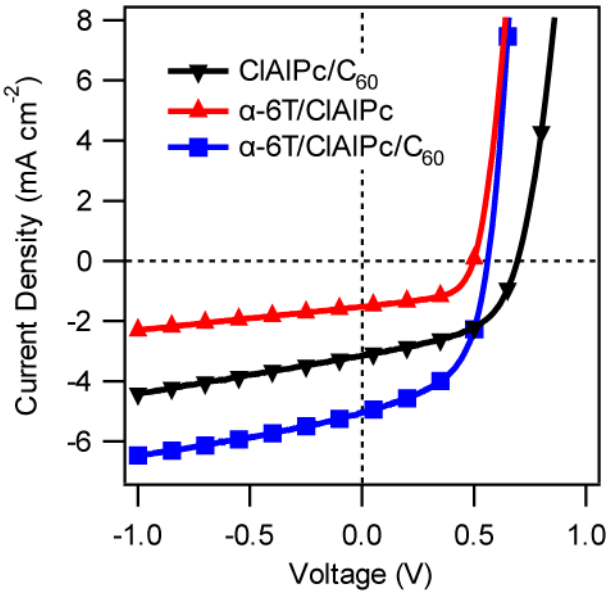

Figure 5.9: *J-V* plots of ClAlPc / C_{60}, α-6T / ClAlPc and α-6T/ ClAlPc / C_{60} OPV devices under AM1.5 100 $mWcm^{-2}$ simulated light.

Device Structure (nm)	J_{SC} (mA cm^{-2})	V_{OC} (V)	*FF*	*PCE* (%)
ClAlPc (20) / C_{60} (40)	3.16	0.69	0.52	1.13
α-6T (5) / ClAlPc (20)	1.53	0.50	0.56	0.42
α-6T (5) / ClAlPc (20) / C_{60} (40)	5.08	0.56	0.51	1.46

Table 5.3: Device parameters of ClAlPc / C_{60}, α-6T / ClAlPc and α-6T/ ClAlPc / C_{60} OPV devices under AM1.5 100 mWcm^{-2} simulated light.

The *EQE* was measured to investigate the origin of the photocurrent increase in the cascade device. Figure 5.10 shows the EQE for the cascade device along with the two substituent heterojunction devices. The ClAlPc / C_{60} device shows a contribution from both the absorption regions of C_{60} from 400–500 nm and the ClAlPc at 600–800 nm. The ClAlPc peaks with an *EQE* of 11.4 % at 740 nm. In the α-6T / ClAlPc device, the *EQE* follows the absorption spectra of the ClAlPc with no contribution from the α-6T. As with the SubPc based cascade device (Figure 5.3) there is no improvement in the C_{60} region 400 -500 nm in the α-6T / ClAlPc / C_{60} cascade device indicating no improvement in the ClAlPc / C_{60} heterojunction. The large gain in *EQE* occurs in the ClAlPc region where *EQE* is improved from 600–800 nm peaking at 24 % at 740 nm, over a 50 % increase from the ClAlPc / C_{60} device. This suggests that the same cascade mechanism is happening in the α-6T / ClAlPc / C_{60} device, where two heterojunction interfaces are provided with ClAlPc acting as an acceptor for α-6T and a donor for C_{60}, increasing exciton dissociation.

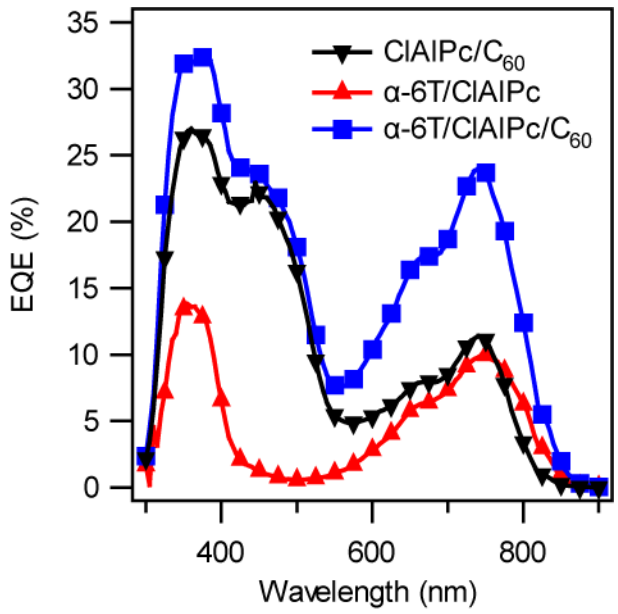

Figure 5.10: *EQE* spectra of ClAlPc/ C_{60}, α-6T / ClAlPc and α-6T/ ClAlPc / C_{60} OPV devices.

The thickness dependence of the α-6T layer in the α-6T / ClAlPc / C_{60} cascade device was also investigated and the *J-V* characteristics are presented in Figure 5.10 with the performance characteristics summarised in Table 5.4. A reduction in J_{SC} is seen with increased thickness of α-6T from 5.17 mA cm^{-2} for the 10 nm α-6T layer to 3.65 mA cm^{-2} for 30 nm. This is contrary to what was seen for the SubPc device and a reduction in *FF* is seen from 0.50 to 0.41 in the 30 nm layer. These factors reduce the *PCE* to 0.83 % for the cascade device with 30 nm of α-6T compared to the 10 nm α-6T device of 1.41 %.

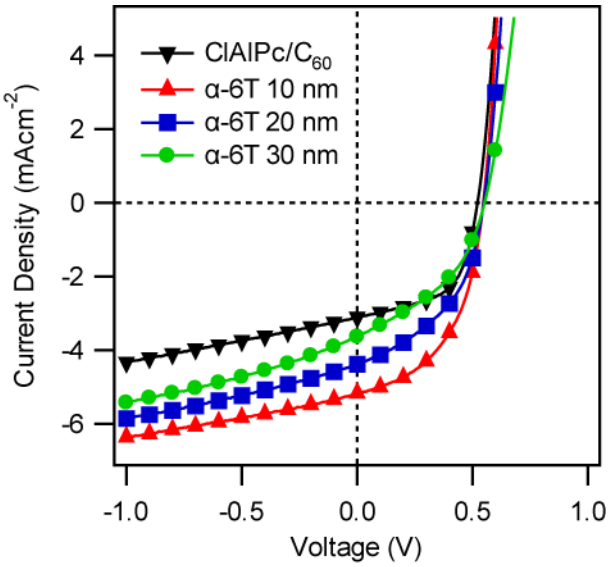

Figure 5.11: *J-V* plots for the α-6T / ClAlPc / C_{60} cascade OPV devices with multiple thicknesses of α-6T; 0, 10, 20 and 30 nm under simulated AM1.5 illumination.

α-6T Thickness (nm)	J_{SC} (mA cm^{-2})	V_{OC} (V)	*FF*	*PCE* (%)
0 nm	3.11	0.53	0.56	0.92
10 nm	5.17	0.55	0.50	1.41
20 nm	4.41	0.55	0.46	1.10
30 nm	3.65	0.55	0.41	0.83

Table 5.4: Device parameters for the α-6T / ClAlPc / C_{60} cascade OPV devices with multiple thicknesses of α-6T; 0, 10, 20 and 30 nm

Figure 5.12 displays the *EQE* of the cascade devices with varied thickness of α-6T. As with the previous *EQE* (Figure 5.10) a large increase in ClAlPc is shown on the insertion of a 10 nm α-6T layer from 9.6 % to 23.4 % at 740 nm. Increasing the thickness of this layer causes a reduction in *EQE* in both the C_{60} (400 -500 nm) and ClAlPc (600 – 800 nm) absorption regions. There is also a blue shift in the main ClAlPc peak with increased α-6T thickness from 745 nm for 0nm to 730 nm for 30 nm. In section 3.4, structural templating ClAlPc with PTCDA showed a red shift in the Q-band absorption peak as the film becomes more ordered. This blue shift with α-6T thickness may result from decreased ordering of the ClAlPc molecules which

could lower the mobility of the film, reducing the photocurrent and *FF* in the device. The *EQE* of the dual heterojunction cascade device at 30 nm α-6T is still larger than the bilayer device due to the two exciton dissociation interfaces.

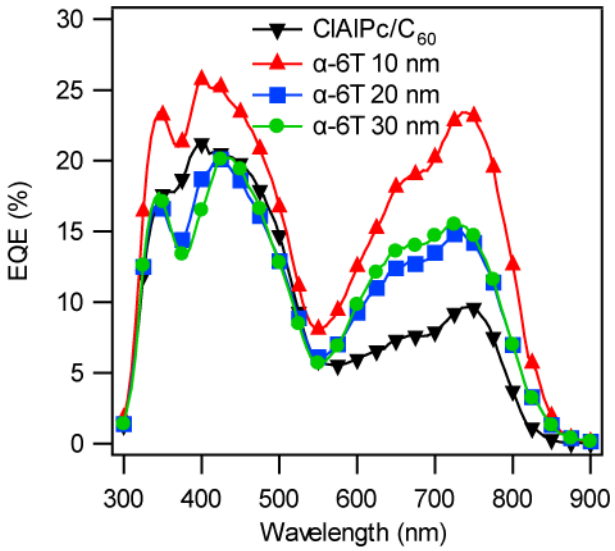

Figure 5.12: *EQE* spectra for the α-6T / ClAlPc / C_{60} cascade OPV devices with multiple thicknesses of α-6T; 0, 10, 20 and 30 nm.

5.4 Summary

This chapter introduced a cascade device architecture using an α-6T layer in conjunction with phthalocyanine / C_{60} devices. Exciton dissociation was shown between SubPc and α-6T from PL quenching measurements. The highest quenching was seen for the cascade device indicating dual dissociation in the SubPc layer. The cascade device data showed an improvement in J_{SC} from 5.23 mA cm^{-2} to 6.23 mA cm^{-2} compared to the SubPc / C_{60} device although the overall *PCE* was reduced from 1.81 % to 1.66%. The EQE showed this improvement in photocurrent to originate from the SubPc layer, indicating dissociation at each interface. Contribution from the α-6T layer was also shown with increasing thickness although little efficiency improvement was seen.

The cascade device structure was also investigated for a ClAlPc / C_{60} device which showed a 50 % improvement in J_{SC} from 3.16 mA cm^{-2} to 5.08 mA cm^{-2} on the addition of the α-6T layer. EQE measurements showed that the improvement in photocurrent was due to the ClAlPc dissociating at both interfaces in the same cascade mechanism as the SubPc device. Due to the maintenance of the high *FF* in the cascade device, unlike the SubPc cascade device, the *PCE* was increased from 1.13 % to 1.46%. The thickness dependence of the α-6T in the cascade device was also studied with a decrease in performance found for thicker α-6T layers.

Chapter 6: Conclusions

This thesis has investigated the design of multi-heterojunction architectures for small molecule OPV devices as a way of improving their performance. The work has been separated into three main areas:

- The optimisation of the Ag recombination layer and the modification of the photoactive layers in a tandem OPV device.
- The use of α-NPD co-deposited with MoOx as a hole transporting optical spacer layer in single and tandem OPV devices.
- Using a dual heterojunction cascade structure to improve photocurrent in PHJ OPV devices.

6.1 Modification of the photoactive layers

Investigation of the Ag recombination layer in a tandem OPV device showed a thickness dependence on the performance. Ultra-thin layers of Ag form nanoclusters around 30 nm in diameter and were shown to embed in the underlying BCP layer. Transmittance spectra of a range of thicknesses from 0.3 – 1.6 nm show ~20 % decrease in transmittance at 550 nm when increasing thickness. Implementation of the Ag recombination layer in a ClAlPc / C_{60} // SubPc / C_{60} tandem device showed an increase in V_{OC} compared to the device without from 1.18 V to 1.75 V as the Ag nanoclusters act as recombination sites for the electrons and holes for each sub-cell. The photocurrent of the device decreased with increasing Ag thickness from 3.84 mA cm^{-2} to 2.57 mA cm^{-2}, as the parasitic absorption of the Ag layer increases. An optimum Ag thickness of 0.3 nm was found and resulted in a *PCE* of 3.43 % which is over double the efficiency of the tandem device without the Ag layer. A slow

deposition rate of 0.5 $Å s^{-1}$ for the Ag layer was chosen to maintain accuracy of the layer thickness.

Modification of the photoactive layers by co-deposition of the donor and acceptor has been used to increase exciton dissociation. The effect of the BHJ ratio in a ClAlPc:C_{60} device shows an increase in photocurrent with a higher proportion of C_{60} in the co-deposited layer. It was seen in the EQE spectra of the devices that a large variation in the C_{60} contribution at 450 nm occurred relative to the BHJ ratio, while the change ClAlPc contribution was lower. The calculated absorptance of the photoactive layers indicated that the larger variation in the C_{60} compared to the ClAlPc was due to the layer being positioned in a peak in the optical field that is suited to the 450 nm absorption of C_{60}. Creating a tandem OPV device consisting of two BHJ sub-cells allows for increased photocurrent generation compared to a PHJ device. Using BHJ sub-cells in a ClAlPc:C_{60}//SubPc:C_{60} tandem device a photocurrent increase from 3.84 mA cm^{-2} to 4.54 mA cm^{-2} was observed due to the enhanced exciton dissociation. Overall the *PCE* improved from 3.43 % in the PHJ device to 3.81 % in the BHJ device.

Finally, the use of a PTCDA structural template to preferentially align the ClAlPc molecules for charge transport in a PHJ OPV device has been investigated. The absorption of the templated ClAlPc showed a red shift in the Q band suggesting increased ordering of the film. AFM of the surface topography of ClAlPc saw only a small change in surface roughness on addition of the PTCDA layer. In a single PHJ ClAlPc / C_{60} OPV device, the J_{SC} and the *FF* were improved on the addition of the PTCDA templating layer. In the tandem OPV device, the improvement in *FF* from 0.51 to 0.55 on addition of the PTCDA layer contributed to the improved efficiency of 3.59 %.

6.2 α-NPD as an Optical Spacer Layer

An investigation of α-NPD as a hole transporting optical spacer layer for OPV devices was shown. The conductivity of the α-NPD layer was improved by co-deposition with 5 % MoO_x leading to only a small loss in transmission due to the radical cation peak at 500 nm from electron transfer from the α-NPD to the MoO_x.. Kelvin probe was used to show the Fermi level shift of α-NPD on the addition of MoO_x which was pinned to 0.5 eV above the HOMO. AFM showed little variation in surface topography with different MoOx concentration with a RMS roughness < 1 nm.

α-NPD was used as a HTL in single heterojunction SubPc / C_{60} devices. The intrinsic α-NPD layer showed reduced performance compared to the MoO_x HTL due to the high series resistance of the layer. The co-deposited α-NPD:MoO_x layer was shown to be an effective HTL for SubPc / C_{60} devices with the inclusion of a MoO_x interlayer for hole extraction from the SubPc. A slight reduction in J_{SC} was observed due to the parasitic absorption of the α-NPD:MoO_x layer. This HTL showed an adequate performance up to 130 nm.

Subsequently, the optical spacing effect of an α-NPD:MoO_x layer in a ClAlPc:C_{60} BHJ device was investigated. Optical simulations showed the optical field effect on the J_{SC}. Similar results were found for the devices with a large variation in J_{SC} at different optical spacer thicknesses ranging from 1.87 mA cm^{-2} to 5.25 mA cm^{-2}. The V_{OC} and the *FF* remained constant with spacer layer thickness indicating no resistance loss in the layer. EQE measurements showed how the different absorbing wavelengths are affected by the optical field.

The α-NPD:MoO_x optical spacer layer was also implemented into a tandem OPV device based on ClAlPc / C_{60} and SubPc / C_{60} sub-cells. No improvement in performance was found due to the device being previously optimised.

Finally, the α-NPD:MoO_x optical spacer layer was used to investigate current matching in a SubPc:C_{60} BHJ tandem OPV device. Optical simulations showed that the tandem OPV device has unbalanced sub-cell photocurrents due to low absorptance in the front sub-cell, as it is positioned in a poor optical position for SubPc absorption. Using an α-NPD:MoO_x optical spacer layer of 60 nm produces balance photocurrents with a J_{SC} improvement from 3.22 mA cm^{-2} to 4.72 mA cm^{-2}. EQE and TAE measurements showed an increase in contribution from the SubPc at 590 nm which corroborates with gain in SubPc absorptance in the optical simulation. Increasing the pixel size to 1 cm^2 showed a small decrease in performance from 4.32 % to 4.10 % and it displayed a stability for ~100 days under constant illumination.

6.3 Cascade multi-heterojunction device

The construction of a dual heterojunction cascade PHJ OPV device was investigated for two phthalocyanine / C_{60} based systems. α-6T was selected to create a cascade energy structure with ClAlPc/C_{60} and SubPc/C_{60} as the HOMO energy level of 4.95 eV provides an energy gap that can overcome the exciton binding energy. Films of α-6T deposited onto ITO show a large grain structure with a surface roughness that increases with film thickness. PL quenching spectra was used to evaluate the exciton dissociation at the α-6T / SubPc heterojunction interface with quenching observed indicating exciton dissociation. The cascade structure produced the lowest PL signal for SubPc excitation suggesting dissociation at each interface. Device data for the α-

6T / SubPc / C_{60} cascade system and its constituent heterojunctions was measured with α-6T / SubPc producing an effective heterojunction device showing the ambipolar ability of SubPc as a donor and an acceptor. The dual heterojunction cascade device showed a 20 % improvement in J_{SC} from the SubPc / C_{60} device indicating increased exciton dissociation. EQE measurements revealed that the enhancement in photocurrent was from the increase in the SubPc contribution between 500 – 600 nm with no observed change in the C_{60} suggesting exciton dissociation in the SubPc layer at each interface. Thicker α-6T layers in the cascade device were investigated and the performance increased with α-6T thickness. Photocurrent contribution was seen from the thicker α-6T layer with a reduction in series resistance from improved charge extraction.

In the α-6T / ClAlPc / C_{60} cascade device system the ambipolar ability of the ClAlPc was demonstrated in an α-6T / ClAlPc PHJ device although photocurrent was low due to poor alignment with the optical field. The cascade device showed a 50 % improvement in J_{SC} from 3.16 mA cm^{-2} to 5.08 mA cm^{-2} with a drop in the V_{OC} and the *FF*. Overall the cascade device showed an increase in efficiency from 1.13 % to 1.46 %. EQE measurements indicated that the improvement in photocurrent was due to the ClAlPc dissociating at two interfaces in the same cascade mechanism as the SubPc device. The thickness dependence of the α-6T layer in the cascade device was also studied with a decrease in J_{SC} and *FF* seen for thicker α-6T layers, possibly due to the roughness of the underlying layer.

6.4 Future Work

This work has shown how different multi-heterojunction device architectures can be used to improve the performance of an OPV device. This gives a wide scope for further development of device architecture. Optical spacing was used as a tool to optimise the current matching of sub-cells and this can be developed further by adding an optical spacer on both sides of the photoactive layer to ensure the entire absorbing layer is in an optimum optical field position. In terms of photoactive materials, a new near infrared absorber in conjunction with SubPc would help extend spectral range of the tandem device to improve its efficiency which could be optimised with the optical spacer layer. Extending the concept further, a third sub-cell can be added to create a high voltage tandem OPV device as there is a large amount of photons that can be captured in the infrared.

The cascade OPV device was introduced as a method to increase the photocurrent of an absorbing layer. This work is still in its infancy, and factors determining what govern the V_{OC} of the device are not well known. A systematic study of phthalocyanine derivatives with different energy levels as the donor layers could determine what factors affect the V_{OC}. Further development of the architecture of a cascade device would require an interfacial layer with a high ambipolar mobility and combining it with broadly absorbing donor and acceptors. As a future concept, the combination of a cascade OPV device in a multijunction architecture could provide a high J_{SC} coupled with a high V_{OC}, leading to an efficient OPV device.

Chapter 7 References

(1) BP statistical review of world energy 2012

(2) Hansen, J.; Sato, M.; Ruedy, R.; Lo, K.; Lea, D. W.; Medina-Elizade, M. *Proceedings of the National Academy of Sciences. U. S. A.* **2006**, *103*, 14288.

(3) Ohl, R., US Patent 2042662: Light Sensitive Device. 1946.

(4) Green, M. A.; Emery, K.; Hishikawa, Y.; Warta, W.; Dunlop, E. D. *Progress in Photovoltaics: Research and Applications* **2012**, *20*, 606.

(5) Geisz, J. F.; Friedman, D. J.; Ward, J. S.; Duda, A.; Olavarria, W. J.; Moriarty, T. E.; Kiehl, J. T.; Romero, M. J.; Norman, A. G.; Jones, K. M. *Applied Physics Letters* **2008**, *93*.

(6) http://www.nrel.gov/ncpv/images/efficiency_chart.jpg 1/02/13

(7) Oregan, B.; Gratzel, M. *Nature* **1991**, *353*, 737.

(8) Yella, A.; Lee, H. W.; Tsao, H. N.; Yi, C. Y.; Chandiran, A. K.; Nazeeruddin, M. K.; Diau, E. W. G.; Yeh, C. Y.; Zakeeruddin, S. M.; Gratzel, M. *Science* **2011**, *334*, 629.

(9) Chamberlain, G. A.; Cooney, P. J. *Chemical Physics Letters* **1979**, *66*, 88.

(10) Tang, C. W. *Applied Physics Letters* **1986**, *48*, 183.

(11) Peumans, P.; Forrest, S. R. *Applied Physics Letters* **2001**, *79*, 126.

(12) Sullivan, P.; Heutz, S.; Schultes, S. M.; Jones, T. S. *Applied Physics Letters* **2004**, *84*, 1210.

(13) Rand, B. P.; Xue, J. G.; Uchida, S.; Forrest, S. R. *Journal of Applied Physics* **2005**, *98*.

(14) Pfuetzner, S.; Meiss, J.; Petrich, A.; Riede, M.; Leo, K. *Applied Physics Letters* **2009**, *94*.

(15) Fitzner, R.; Mena-Osteritz, E.; Mishra, A.; Schulz, G.; Reinold, E.; Weil, M.; Korner, C.; Ziehlke, H.; Elschner, C.; Leo, K.; Riede, M.; Pfeiffer, M.; Uhrich, C.; Bauerle, P. *Journal of the American Chemical Society* **2012**, *134*, 11064.

(16) Mishra, A.; Bauerle, P. *Angew. Chem.-Int. Edit.* **2012**, *51*, 2020.

(17) Chen, Y. H.; Lin, L. Y.; Lu, C. W.; Lin, F.; Huang, Z. Y.; Lin, H. W.; Wang, P. H.; Liu, Y. H.; Wong, K. T.; Wen, J. G.; Miller, D. J.; Darling, S. B. *Journal of the American Chemical Society* **2012**, *134*, 13616.

(18) Hiramoto, M.; Suezaki, M.; Yokoyama, M. *Chemistry Letters* **1990**.

(19) Yakimov, A.; Forrest, S. R. *Applied Physics Letters* **2002**, *80*, 1667.

(20) Maennig, B.; Drechsel, J.; Gebeyehu, D.; Simon, P.; Kozlowski, F.; Werner, A.; Li, F.; Grundmann, S.; Sonntag, S.; Koch, M.; Leo, K.; Pfeiffer, M.; Hoppe, H.; Meissner, D.; Sariciftci, N. S.; Riedel, I.; Dyakonov, V.; Parisi, J. *Applied Physics A* **2004**, *79*, 1.

(21) Drechsel, J.; Mannig, B.; Kozlowski, F.; Pfeiffer, M.; Leo, K.; Hoppe, H. *Applied Physics Letters* **2005**, *86*.

(22) Xue, J. G.; Uchida, S.; Rand, B. P.; Forrest, S. R. *Applied Physics Letters* **2004**, *85*, 5757.

(23) Cheyns, D.; Rand, B. P.; Heremans, P. *Applied Physics Letters* **2010**, *97*, 033301.

(24) Howells, T.; New, E.; Sullivan, P.; Jones, T. S. *Advanced Energy Materials* **2011**, *1*, 1085.

(25) Macko, J. A.; Lunt, R. R.; Osedach, T. P.; Brown, P. R.; Barr, M. C.; Gleason, K. K.; Bulovic, V. *Physical Chemistry Chemical Physics* **2012**, *14*, 14548.
(26) Lassiter, B. E.; Zimmerman, J. D.; Panda, A.; Xiao, X.; Forrest, S. R. *Applied Physics Letters* **2012**, *101*.
(27) Heliatek Press release 16/01/2013 www.heliatek.com
(28) Zou, Y.; Deng, Z. B.; Potscavage, W. J.; Hirade, M.; Zheng, Y. Q.; Adachi, C. *Applied Physics Letters* **2012**, *100*.
(29) Sullivan, P.; Schumann, S.; Da Campo, R.; Howells, T.; Duraud, A.; Shipman, M.; Hatton, R. A.; Jones, T. S. *Advanced Energy Materials* **2013**, *3*, 239.
(30) Ameri, T.; Dennler, G.; Lungenschmied, C.; Brabec, C. J. *Energy & Environmental Science* **2009**, *2*, 347.
(31) Kawano, K.; Ito, N.; Nishimori, T.; Sakai, J. *Applied Physics Letters* **2006**, *88*.
(32) Dennler, G.; Prall, H. J.; Koeppe, R.; Egginger, M.; Autengruber, R.; Sariciftci, N. S. *Applied Physics Letters* **2006**, *89*.
(33) Hadipour, A.; de Boer, B.; Wildeman, J.; Kooistra, F.; Hummelen, J. C.; Turbiez, M. G. R.; Wienk, M. M.; Janssen, R. A. J.; Blom, P. W. M. *Organic Optoelectronics and Photonics II* **2006**, *6192*, D1920.
(34) Kim, J. Y.; Lee, K.; Coates, N. E.; Moses, D.; Nguyen, T. Q.; Dante, M.; Heeger, A. J. *Science* **2007**, *317*, 222.
(35) Gilot, J.; Wienk, M. M.; Janssen, R. A. J. *Applied Physics Letters* **2007**, *90*, 143512.
(36) Sista, S.; Park, M. H.; Hong, Z. R.; Wu, Y.; Hou, J. H.; Kwan, W. L.; Li, G.; Yang, Y. *Advanced Materials* **2010**, *22*, 380.
(37) He, Y. J.; Chen, H. Y.; Hou, J. H.; Li, Y. F. *Journal of the American Chemical Society* **2010**, *132*, 1377.
(38) You, J.; Dou, L.; Yoshimura, K.; Kato, T.; Ohya, K.; Moriarty, T.; Emery, K.; Chen, C.-C.; Gao, J.; Li, G.; Yang, Y. *Nature Communications* **2013**, *4*, 1446.
(39) Vaubel, G.; Baessler, H. *Physics Letters A* **1968**, *27*, 328.
(40) Yoo, S.; Domercq, B.; Kippelen, B. *Applied Physics Letters* **2004**, *85*, 5427.
(41) Brutting, W. *Physics of Organic Semiconductors*; Wiley-VCH, 2012.
(42) Gledhill, S. E.; Scott, B.; Gregg, B. A. *Journal of Materials Research* **2005**, *20*, 3167.
(43) Gregg, B. A.; Hanna, M. C. J*ournal of Applied Physics* **2003**, *93*, 3605.
(44) Hill, I. G.; Kahn, A.; Soos, Z. G.; Pascal, R. A. *Chemical Physics Letters* **2000**, *327*, 181.
(45) Peumans, P.; Yakimov, A.; Forrest, S. R. J*ournal of Applied Physics* **2003**, *93*, 3693.
(46) Gommans, H.; Schols, S.; Kadashchuk, A.; Heremans, P.; Meskers, S. C. J. *Journal of Physical Chemistry C* **2009**, *113*, 2974.
(47) Luhman, W. A.; Holmes, R. J. *Advanced Functional Materials* **2011**, *21*, 764.
(48) Rand, B. P.; Burk, D. P.; Forrest, S. R. *Physical Review B* **2007**, *75*.
(49) Offermans, T.; Meskers, S. C. J.; Janssen, R. A. J. *Chemical Physics* **2005**, *308*, 125.
(50) Arkhipov, V. I.; Heremans, P.; Bassler, H. *Applied Physics Letters* **2003**, *82*, 4605.

(51) Potscavage, W. J.; Yoo, S.; Kippelen, B. *Applied Physics Letters* **2008**, *93*, 3.
(52) Potscavage, W. J.; Sharma, A.; Kippelen, B. *Accounts of Chemical Research* **2009**, *42*, 1758.
(53) Cnops, K.; Rand, B.; Cheyns, D.; Heremans, P. *Applied Physics Letters* **2012**, *101*.
(54) Hains, A. W.; Liang, Z. Q.; Woodhouse, M. A.; Gregg, B. A. *Chemical Reviews* **2010**, *110*, 6689.
(55) Bredas, J. L.; Norton, J. E.; Cornil, J.; Coropceanu, V. *Accounts of Chemical Research* **2009**, *42*, 1691.
(56) Headrick, R. L.; Wo, S.; Sansoz, F.; Anthony, J. E. *Applied Physics Letters* **2008**, *92*, 063302.
(57) Beaumont, N.; Hancox, I.; Sullivan, P.; Hatton, R. A.; Jones, T. S. *Energy & Environmental Science* **2011**, *4*, 1708.
(58) Khodabakhsh, S.; Sanderson, B. M.; Nelson, J.; Jones, T. S. *Advanced Functional Materials* **2006**, *16*, 95.
(59) Chen, L. M.; Xu, Z.; Hong, Z. R.; Yang, Y. *Journal of Materials Chemistry* **2010**, *20*, 2575.
(60) Hancox, I.; Sullivan, P.; Chauhan, K. V.; Beaumont, N.; Rochford, L. A.; Hatton, R. A.; Jones, T. S. *Organic Electronics* **2010**, *11*, 2019.
(61) Schumann, S.; Da Campo, R.; Illy, B.; Cruickshank, A. C.; McLachlan, M. A.; Ryan, M. P.; Riley, D. J.; McComb, D. W.; Jones, T. S. *Journal of Materials Chemistry* **2011**, *21*, 2381.
(62) Timmreck, R.; Olthof, S.; Leo, K.; Riede, M. K. J*ournal of Applied Physics* **2010**, *108*, 033108.
(63) Rand, B. P.; Peumans, P.; Forrest, S. R. J*ournal of Applied Physics* **2004**, *96*, 7519.
(64) Zhao, D. W.; Sun, X. W.; Jiang, C. Y.; Kyaw, A. K. K.; Lo, G. Q.; Kwong, D. L. *Applied Physics Letters* **2008**, *93*.
(65) Hiramoto, M.; Suezaki, M.; Yokoyama, M. *Chemistry Letters* **1990**, 327.
(66) Zhou, Y. H.; Fuentes-Hernandez, C.; Shim, J. W.; Khan, T. M.; Kippelen, B. *Energy & Environmental Science* **2012**, *5*, 9827.
(67) Hadipour, A.; de Boer, B.; Blom, P. W. M. *Organic Electronics* **2008**, *9*, 617.
(68) Hadipour, A.; de Boer, B.; Blom, P. W. M. J*ournal of Applied Physics* **2007**, *102*, 074506.
(69) Gilot, J.; Wienk, M. M.; Janssen, R. A. J. *Advanced Functional Materials* **2010**, *20*, 3904.
(70) Gilot, J.; Wienk, M. M.; Janssen, R. A. J. *Organic Electronics* **2011**, *12*, 660.
(71) Gilot, J.; Wienk, M. M.; Janssen, R. A. J. *Advanced Materials* **2010**, *22*, E67.
(72) Gilot, J.; Barbu, I.; Wienk, M. M.; Janssen, R. A. J. *Applied Physics Letters* **2007**, *91*, 113520.
(73) Ameri, T.; Dennler, G.; Waldauf, C.; Denk, P.; Forberich, K.; Scharber, M. C.; Brabec, C. J.; Hingerl, K. J*ournal of Applied Physics* **2008**, *103*.
(74) Mityashin, A.; Cheyns, D.; Rand, B. P.; Heremans, P. *Applied Physics Letters* **2012**, *100*.
(75) Chan, M. Y.; Lai, S. L.; Lau, K. M.; Lee, C. S.; Lee, S. T. *Applied Physics Letters* **2006**, *89*.
(76) Heidel, T. D.; Hochbaum, D.; Sussman, J. M.; Singh, V.; Bahlke, M. E.; Hiromi, I.; Lee, J.; Baldo, M. A. J*ournal of Applied Physics* **2011**, *109*, 104502.

(77) Huang, J. A.; Yu, J. S.; Wang, W.; Jiang, Y. D. *Applied Physics Letters* **2011**, *98*, 023301.
(78) Sista, S.; Yao, Y.; Yang, Y.; Tang, M. L.; Bao, Z. *Applied Physics Letters* **2007**, *91*.
(79) Schlenker, C. W.; Barlier, V. S.; Chin, S. W.; Whited, M. T.; McAnally, R. E.; Forrest, S. R.; Thompson, M. E. *Chemistry of Materials* **2011**, *23*, 4132.
(80) Ichikawa, M.; Suto, E.; Jeon, H.; Taniguchi, Y. *Organic Electronics* **2010**, *11*, 700.
(81) Hong, Z.; Lessmann, R.; Maennig, B.; Huang, Q.; Harada, K.; Riede, M.; Leo, K. *Journal of Applied Physics* **2009**, *106*.
(82) McKeown, N. B., Phthalocyanine Materials: Synthesis, Structure and Function; Cambridge University Press: Cambridge, U.K., 1998
(83) Liu, S. H.; Wang, W. C. M.; Briseno, A. L.; Mannsfeld, S. C. E.; Bao, Z. N. A*dvanced Materials* 2**009,** 2*1*, 1217.
(84) Peisert, H.; Knupfer, M.; Schwieger, T.; Fuentes, G. G.; Olligs, D.; Fink, J.; Schmidt, T. J*ournal of Applied Physics* 2**003,** 9*3*, 9683.
(85) Hatton, R. A.; Blanchard, N. P.; Miller, A. J.; Silva, S. R. P. P*hysica E* 2**007,** 3*7*, 124.
(86) AzimAraghi, M. E.; Krier, A. P*ure and Applied Optics* 1**997,** 6, 443.
(87) Li, L. Q.; Hu, W. P.; Fuchs, H.; Chi, L. F. A*dvanced Energy Materials* 2**011,** 1, 188.
(88) Verreet, B.; Muller, R.; Rand, B.; Vasseur, K.; Heremans, P. O*rganic Electronics* 2**011,** 1*2*, 2131.
(89) Kato, K.; Saito, Y.; Ohdaira, Y.; Shinbo, K.; Kaneko, F. T*hin Solid Films* 2**006,** 4*99*, 174.
(90) Chauhan, K.; Sullivan, P.; Yang, J.; Jones, T. J*ournal of Physical Chemistry C* 2**010,** 1*14*, 3304.
(91) Mao, H. Y.; Wang, R.; Wang, Y.; Niu, T. C.; Zhong, J. Q.; Huang, M. Y.; Qi, D. C.; Loh, K. P.; Wee, A. T. S.; Chen, W. A*pplied Physics Letters* 2**011,** 9*9*, 3.
(92) Bailey-Salzman, R.; Rand, B.; Forrest, S. A*pplied Physics Letters* 2**007,** 9*1*.
(93) Cheyns, D.; Rand, B. P.; Heremans, P. A*pplied Physics Letters* 2**010,** 9*7*.
(94) Meller, A.; Ossko, A. M*onatshefte Fur Chemie* 1**972,** 1*03*, 150.
(95) Claessens, C. G.; Gonzalez-Rodriguez, D.; Torres, T. C*hemical Reviews* 2**002,** 1*02*, 835.
(96) Gommans, H.; Cheyns, D.; Aernouts, T.; Girotto, C.; Poortmans, J.; Heremans, P. A*dvanced Functional Materials* 2**007,** 1*7*, 2653.
(97) Mutolo, K.; Mayo, E.; Rand, B.; Forrest, S.; Thompson, M. J*ournal of the American Chemical Society* 2**006,** 1*28*, 8108.
(98) Sullivan, P.; Duraud, A.; Hancox, I.; Beaumont, N.; Mirri, G.; Tucker, J.; Hatton, R.; Shipman, M.; Jones, T. A*dvanced Energy Materials* 2**011,** 1, 352.
(99) Heremans, P.; Cheyns, D.; Rand, B. P. A*ccounts of Chemical Research* 2**009,** 4*2*, 1740.
(100) Kroto, H. W.; Heath, J. R.; Obrien, S. C.; Curl, R. F.; Smalley, R. E. N*ature* 1**985,** 3*18*, 162.
(101) Hamed, A.; Sun, Y. Y.; Tao, Y. K.; Meng, R. L.; Hor, P. H. P*hysical Review B* 1**993,** 4*7*, 10873.
(102) Haddon, R. C.; Brus, L. E.; Raghavachari, K. C*hemical Physics Letters* 1**986,** 1*25*, 459.

(103) Kratschmer, W.; Lamb, L. D.; Fostiropoulos, K.; Huffman, D. R. N*ature* 1**990,** 3*47,* 354.
(104) Pfuetzner, S.; Meiss, J.; Petrich, A.; Riede, M.; Leo, K. A*pplied Physics Letters* 2**009,** 9*4,* 3.
(105) Faiman, D.; Goren, S.; Katz, E. A.; Koltun, M.; Melnik, N.; Shames, A.; Shtutina, S. T*hin Solid Films* 1**997,** 2*95,* 283.
(106) Sease, J. W.; Zechmeister, L. J*ournal of the American Chemical Society* 1**947,** 6*9,* 270.
(107) Fichou, D. J*ournal of Materials Chemistry* 2**000,** 1*0,* 571.
(108) Horowitz, G.; Fichou, D.; Garnier, F. S*olid State Communications* 1**989,** 7*0,* 385.
(109) Horowitz, G.; Fichou, D.; Peng, X. Z.; Xu, Z. G.; Garnier, F. S*olid State Communications* 1**989,** 7*2,* 381.
(110) Garnier, F.; Horowitz, G.; Peng, X. H.; Fichou, D. A*dvanced Materials* 1**990,** 2, 592.
(111) Matsushima, T.; Murata, H. J*ournal of Applied Physics* 2**012,** 1*12.*
(112) Sakai, J.; Taima, T.; Saito, K. O*rganic Electronics* 2**008,** 9, 582.
(113) VanSlyke, S. A.; Chen, C. H.; Tang, C. W. A*pplied Physics Letters* 1**996,** 6*9,* 2160.
(114) Deng, Z. B.; Lee, S. T.; Webb, D. P.; Chan, Y. C.; Gambling, W. A. S*ynthetic Metals* 1**999,** 1*07,* 107.
(115) Kroger, M.; Hamwi, S.; Meyer, J.; Riedl, T.; Kowalsky, W.; Kahn, A. O*rganic Electronics* 2**009,** 1*0,* 932.
(116) Zhang, M. L.; Wang, H.; Tang, C. W. A*pplied Physics Letters* 2**011,** 9*9,* 3.
(117) Avendano, F. M.; Forsythe, E. W.; Gao, Y. L.; Tang, C. W. S*ynthetic Metals* 1**999,** 1*02,* 910.
(118) Rand, B. P.; Li, J.; Xue, J. G.; Holmes, R. J.; Thompson, M. E.; Forrest, S. R. A*dvanced Materials* 2**005,** 1*7,* 2714.
(119) Drechsel, J.; Petrich, A.; Koch, M.; Pfützner, S.; Meerheim, R.; Scholz, S.; Walzer, K.; Pfeiffer, M.; Leo, K. S*ID Symposium Digest of Technical Papers* 2**006,** 3*7,* 1692.
(120) Donley, C.; Dunphy, D.; Paine, D.; Carter, C.; Nebesny, K.; Lee, P.; Alloway, D.; Armstrong, N. R. L*angmuir* 2**002,** 1*8,* 450.
(121) Binnig, G.; Quate, C. F.; Gerber, C. P*hysical Review Letters* 1**986,** 5*6,* 930.
(122) C.Manos, B. Tompkins, MFP-3D Atomic Force Microscope, Asylum Research Inc., 2008
(123) Pettersson, L. A. A.; Roman, L. S.; Inganas, O. J*ournal of Applied Physics* 1**999,** 8*6,* 487.
(124) J. Nelson, The Physics of Solar Cells, Imperial College Press, London, 2003
(125) Xue, J. G.; Uchida, S.; Rand, B. P.; Forrest, S. R. A*pplied Physics Letters* 2**004,** 8*5.*
(126) Xu, G.; Chen, Y.; Tazawa, M.; Jin, P. A*pplied Physics Letters* 2**006,** 8*8,* 3.
(127) Lunt, R.; Giebink, N.; Belak, A.; Benziger, J.; Forrest, S. J*ournal of Applied Physics* 2**009,** 1*05.*
(128) Peumans, P.; Uchida, S.; Forrest, S. R. N*ature* 2**003,** 4*25,* 158.
(129) Fitzner, R.; Reinold, E.; Mishra, A.; Mena-Osteritz, E.; Ziehlke, H.; Korner, C.; Leo, K.; Riede, M.; Weil, M.; Tsaryova, O.; Weiss, A.; Uhrich, C.; Pfeiffer, M.; Bauerle, P. A*dvanced Functional Materials* 2**011,** 2*1,* 897.
(130) Pandey, R.; Holmes, R. A*dvanced Materials* 2**010,** 2*2,* 5301.
(131) Zhang, M.; Wang, H.; Tang, C. W. O*rganic Electronics* 2**012,** 1*3.*

(132) Pandey, R.; Gunawan, A. A.; Mkhoyan, K. A.; Holmes, R. J. A*dvanced Functional Materials* 2**012,** 2*2,* 617.
(133) Sullivan, P.; Jones, T. S.; Ferguson, A. J.; Heutz, S. *Applied Physics Letters* 2**007,** 9*1,* 233114.
(134) Sielcken, O. E.; Van Tilborg, M. M.; Roks, M. F. M.; Hendriks, R.; Drenth, W.; Nolte, R. J. M. J*ournal of the American Chemical Society* 1**987,** 1*09,* 4261.
(135) Rand, B.; Cheyns, D.; Vasseur, K.; Giebink, N.; Mothy, S.; Yi, Y.; Coropceanu, V.; Beljonne, D.; Cornil, J.; Bredas, J.; Genoe, J. A*dvanced Functional Materials* 2**012,** 2*2,* 2987.
(136) Blom, P. W. M.; deJong, M. J. M.; Vleggaar, J. J. M. *Applied Physics Letters* 1**996,** 6*8,* 3308.
(137) Blochwitz, J.; Pfeiffer, M.; Fritz, T.; Leo, K. A*pplied Physics Letters* 1**998,** 7*3,* 729.
(138) Walzer, K.; Maennig, B.; Pfeiffer, M.; Leo, K. C*hem Rev* 2**007,** 1*07,* 1233.
(139) http://www.sigmaaldrich.com/catalog/product/aldrich/376779
(140) Matsushima, T.; Murata, H. *Applied Physics Letters* 2**009,** 9*5,* 203306.
(141) Lee, J.; Kim, H.; Kim, K.; Kim, J. O*rganic Electronics* 2**011,** 1*2,* 950.
(142) Tress, W.; Leo, K.; Riede, M. A*dvanced Functional Materials* 2**011,** 2*1,* 2140.
(143) Schueppel, R.; Timmreck, R.; Allinger, N.; Mueller, T.; Furno, M.; Uhrich, C.; Leo, K.; Riede, M. J*ournal of Applied Physics* 2**010,** 1*07.*
(144) Jin, H.; Tao, C.; Velusamy, M.; Aljada, M.; Zhang, Y.; Hambsch, M.; Burn, P. L.; Meredith, P. A*dvanced Materials* 2**012,** 2*4,* 2572.
(145) Shrotriya, V.; Li, G.; Yao, Y.; Moriarty, T.; Emery, K.; Yang, Y. A*dvanced Functional Materials* 2**006,** 1*6,* 2016.
(146) Riede, M.; Uhrich, C.; Widmer, J.; Timmreck, R.; Wynands, D.; Schwartz, G.; Gnehr, W. M.; Hildebrandt, D.; Weiss, A.; Hwang, J.; Sundarraj, S.; Erk, P.; Pfeiffer, M.; Leo, K. A*dvanced Functional Materials* 2**011,** 2*1,* 3019.
(147) http://www.ossila.com
(148) Peters, C. H.; Sachs-Quintana, I. T.; Mateker, W. R.; Heumueller, T.; Rivnay, J.; Noriega, R.; Beiley, Z. M.; Hoke, E. T.; Salleo, A.; McGehee, M. D. A*dvanced Materials* 2**012,** 2*4,* 663.
(149) F.C.Krebs, Stability and Degridation of Organic and Polymer Solar Cells, Wiley 2012
(150) Uhrich, C. L.; Schwartz, G.; Maennig, B.; Gnehr, W. M.; Sonntag, S.; Erfurth, O.; Wollrab, E.; Walzer, K.; Foerster, J.; Weiss, A.; Tsaryova, O.; Leo, K.; Riede, M. K.; Pfeiffer, M. O*rganic Photonics Iv* 2**010,** 7*722.*
(151) Sista, S.; Yao, Y.; Yang, Y.; Tang, M. L.; Bao, Z. A. *Applied Physics Letters* 2**007,** 9*1.*
(152) Dodabalapur, A.; Torsi, L.; Katz, H. E. S*cience* 1**995,** 2*68,* 270.
(153) Morse, G. E.; Bender, T. P. A*CS Applied Materials & Interfaces* 2**012,** 4, 5055.
(154) Beaumont, N.; Cho, S. W.; Sullivan, P.; Newby, D.; Smith, K. E.; Jones, T. S. A*dvanced Functional Materials* 2**012,** 2*2,* 561.